

**The Effects of Large-Scale Convection on Solar
Eigenfrequencies**

by

Michael Marchand Swisdak, III

B.S., Astronomy, University of Maryland, 1994

B.S., Mathematics, University of Maryland, 1994

B.S., Physics, University of Maryland, 1994

M.S., Astrophysics, University of Colorado, 1996

A thesis submitted to the
Faculty of the Graduate School of the
University of Colorado in partial fulfillment
of the requirements for the degree of
Doctor of Philosophy
Department of Astrophysical and Planetary Sciences

1999

This thesis entitled:
The Effects of Large-Scale Convection on Solar Eigenfrequencies
written by Michael Marchand Swisdak, III
has been approved for the Department of Astrophysical and Planetary Sciences

Ellen G. Zweibel

Juri Toomre

Date _____

The final copy of this thesis has been examined by the signatories, and we find that both the content and the form meet acceptable presentation standards of scholarly work in the above mentioned discipline.

Swisdak, III, Michael Marchand (Ph.D., Astrophysics)

The Effects of Large-Scale Convection on Solar Eigenfrequencies

Thesis directed by Professor Ellen G. Zweibel

We describe and implement an approach for determining the eigenfrequencies of solar acoustic oscillations (p modes) in a convective envelope. By using the ray approximation, we transform the problem into one in which we seek the eigenfrequencies of a Hamiltonian system. To find these eigenfrequencies we have written a computer program which implements the method of adiabatic switching. In this technique, we begin with a system with no convective perturbations for which the eigenmodes and eigenfrequencies are known. The code adiabatically increases the strength of the convective structures, allowing the mode eigenfrequency to adjust from its initial value to the eigenfrequency of the perturbed state. The ray approximation restricts our investigations to perturbations which are large compared to the mode wavelength.

For a simple class of structures we test our results against the predictions of semi-classical EBK quantization and find the two methods agree. We then examine more complicated perturbations, concentrating on the dependence of the frequency shifts on the radial and angular mode numbers as well as the perturbation strength. Among our results, we conclude that the fractional frequency shift is given by the weighted average of the perturbation over the resonant cavity. As a result, convective perturbations with horizontally anti-symmetric structures generate downward frequency shifts which are second-order in the perturbation strength. We also examine more complex convective structures which we find tend to produce downshifts whose magnitude scales with the strength of the perturbation. These results may have implications for resolving the differences between eigenfrequencies derived from solar models and those deduced from helioseismic observations.

Dedication

To Misha

Acknowledgements

This work was supported by NASA GSRP 153-0972, NSF Grant AST-95-21779, the NASA Space Physics Theory Program, and the SOHO/MDI Investigation. Mark Rast and Nic Brummell kindly provided me with the plume model and convective simulation used in §4.3 and §4.4, respectively. Deborah Haber, Jim Meiss, and Rex Skodje provided helpful discussions at critical points along the way.

In addition to the professional acknowledgments, I would like to use this space to thank a few of the people whose influences have been instrumental in seeing this dissertation to fruition. Naturally this is a daunting task; fortunately the associated memories make it an enjoyable one.

Ellen Zweibel, my advisor, well deserves first mention on this list for giving a nervous first-year graduate student a job and then nurturing me through the intervening years. Hopefully I have managed to fulfill at least some small part of her expectations as a student, for she has met and exceeded all of mine as an advisor.

My time at Colorado resonates with great memories, a happy circumstance in part attributable to the students with whom I have had the pleasure of working. Even if specific memories — conversations, scientific and otherwise, social events, and so many Ultimate games — begin to fade, I will always associate a warm glow with my time here. In that spirit, and with a nod to my fear of inadvertently neglecting anyone, I extend a comprehensive acknowledgment to my fellow students.

A few merit special notice. No thesis is written without journeys along roads which, while initially promising, lead to treacherous dead-ends. I am lucky enough to have found several

people who were tolerant enough to listen to my off-track meanderings and, more often than not, gently nudge me onto the correct path. Marc DeRosa has gracefully consented to my, at times seemingly never-ending, barrages of questions, theories, and explanations. Kelsey Johnson, the closest thing to a sister I have ever had, provided uncountable words of encouragement. Rémy Indebetouw showed me the power of forthrightness. And, my officemates Eli Michael and Rekha Jain, who coped with frantic mumblings and assorted eccentricities, deserve special praise for their patience in the midst of it all.

I have been further blessed with a wonderful family. My parents, Michael and Carole, have been the single biggest influence on my life; despite not appearing on the title page, they are as much the authors of this document as I. Stephen, my brother, must be commended for his grace during the onerous task of growing up with me as a sibling. In light of this burden, his accomplishments are even more impressive. And finally I am grateful to Misha, my wife, whose love sustained me, not only through the low points, but along every step of the way.

Thank you all.

Contents

Chapter

1	Introduction	1
1.1	Problem Outline	3
1.2	Solution Method	6
1.3	Literature Review	9
2	Theoretical Justification	12
2.1	Stellar Oscillations	12
2.1.1	Fluid Equations	12
2.1.2	Perturbations	14
2.1.3	Separation of Angular Variables	15
2.1.4	Derivation of a Wave Equation	16
2.2	Asymptotic Approximations	20
2.3	Hamiltonian Systems	24
2.4	Quantization Conditions	26
2.4.1	EBK Quantization	27
2.4.2	A Simple Physical Model	28
2.4.3	P Mode Quantization Conditions	30
2.4.4	Surfaces of Section	32
2.5	Adiabatic Switching	34

3	Implementation and Tests	39
3.1	The Reference State	39
3.1.1	Reference State Results	42
3.1.2	Quantization Conditions	44
3.2	Adiabatic Switching	45
3.3	A Test of an Integrable System	48
3.4	Doppler Shifts	53
4	Convective Structures	57
4.1	Cell-like Velocity Perturbation	57
4.2	Rayleigh-Bénard Boussinesq Convection	64
4.3	Compressible Plume	71
4.4	Turbulent Compressible Convection	81
5	Conclusions	88
5.1	Results	88
5.2	Future Work	91
	Bibliography	94
	Appendix	
A	Table of Important Symbols	97
B	Fluid Descriptions and Perturbations	100
B.1	Descriptions	100
B.2	Mathematical Operations	101
B.3	Perturbations	102
B.4	Commutation Relations	106

B.4.1	Eulerian Perturbation, Commuting Operators	107
B.4.2	Eulerian Perturbation, Non-Commuting Operators	107
B.4.3	Lagrangian Perturbation, Commuting Operators	108
B.4.4	Lagrangian Perturbation, Non-Commuting Operators	108
C	Alternate Forms of the Wave Equation	110
D	The Computer Code	114

Figures

Figure

1.1	The difference between observationally and theoretically determined values of the relative squared sound speed versus solar radius.	4
2.1	Acoustic raypaths in a two-dimensional Sun.	29
3.1	A sample raypath in an adiabatically stratified, two-dimensional, polytropic envelope with $\mu = 3$	41
3.2	A raypath and the evolution of the eigenfrequency for the perturbation of §3.3. .	52
3.3	A raypath and the evolution of the eigenfrequency for the perturbation of §3.4. .	56
4.1	Streamlines for the velocity perturbation of §4.1.	59
4.2	A raypath and the evolution of the eigenfrequency for the perturbation of §4.1. .	65
4.3	Streamlines and isotherms for the convective perturbation of §4.2.	67
4.4	A raypath and the evolution of the eigenfrequency for the perturbation of §4.2. .	73
4.5	Sound speed perturbations for the plume of §4.3.	75
4.6	A raypath and the evolution of the eigenfrequency for the perturbation of §4.3. .	78
4.7	Fractional frequency shift versus strength of the plume of §4.3.	79
4.8	Horizontal slices of the plume of §4.3.	80
4.9	Sound speed and velocity perturbations of the convective model of §4.4.	82
4.10	A raypath and the evolution of the eigenfrequency for the perturbation of §4.4. .	84
4.11	Horizontal slices of the convective model of §4.4.	85

4.12 Fractional frequency shift versus strength of the convective model of §4.4. 87

B.1 A pictorial demonstration of the Eulerian and Lagrangian perturbations. 104

Tables

Table

3.1	Frequency shifts for the perturbation of §3.3.	50
3.2	Frequency shifts for the perturbation of §3.4.	54
4.1	Frequency shifts for the convective perturbation of §4.1.	60
4.2	Frequency shifts for the convection cells of §4.2 with dominant horizontal velocity perturbations.	70
4.3	Frequency shifts for the convection cells of §4.2 with equal strength horizontal velocity and sound speed perturbations.	72
A.1	Important symbols.	97
D.1	Modules used in our adiabatic switching code.	115

Chapter 1

Introduction

Plasma in a thin exterior layer, the photosphere, produces all of the observable light from the Sun; photons generated interior to that layer are unable to escape the Sun without being absorbed and re-emitted. This limitation restricted early observations, but astrophysicists could, and did, construct models of the solar interior based on the available data (primarily the Sun's mass, radius, luminosity, photospheric composition, and age). Unfortunately, their predictions of the interior structure could not be directly confirmed. Only in the last 25 years has it been possible to peer beneath the surface of the Sun and examine its interior structure. The new source of information is the discipline of helioseismology.

Leighton et al. (1962) used observations of the Doppler shifts of photospheric spectral lines to detect the first evidence of solar oscillations. (Modern observations use either a modification of their technique or another method which searches for variations in the total intensity of emitted radiation.) Although other mechanisms were considered, it was eventually proposed (Ulrich 1970; Leibacher & Stein 1971) that acoustic waves forming resonant oscillations, or modes, within the Sun were the source of the signal. Since pressure provides the restoring force for these oscillations, they are now known as p modes. The Sun, like an organ pipe, is a resonant structure capable of sounding only particular notes. In general, an object's structure dictates which notes, or eigenfrequencies as they are called on the Sun, are generated. For an organ pipe the key structural element is its length: A pipe with a C fundamental can also sound the C an octave higher, but will never produce the intervening E^b . Similarly, the composition

and structure (particularly the speed of sound) of the Sun determine its eigenfrequencies. Once correctly identified, it was quickly realized that p modes provide an excellent mechanism for directly exploring the solar interior since p -mode frequencies depend on the solar structure much as organ notes depend on the length of the pipe. Thus, measurements of photospheric quantities permit the probing of the solar interior. Since terrestrial earthquakes produce acoustic waves which are subjected to a similar analysis, the new discipline was termed helioseismology.

Although recent helioseismic investigations conclusively demonstrate that modern solar models closely describe the Sun, there are still statistically significant discrepancies between the predictions and the observations. In this work, we investigate a probable cause of some of the discrepancy: large-scale convection as it affects p -mode frequencies. This first chapter is devoted to the presentation of introductory material. A more detailed outline of the problem is given in §1.1, while §1.2 describes our attempt to resolve it. In the context of helioseismology, we believe our methodology is a novel approach to the problem. However, several antecedent works have attacked the issue from other directions; a review of the relevant literature may be found in §1.3.

Subsequent chapters develop the solution method and its applications. Chapter 2, in which we discuss the mathematical underpinnings of our work, is a visually imposing but crucial component, as it delineates the assumptions on which the following chapters are based. In Chapter 3 we use two unrealistic, but simple, models to illustrate both the implementation of the method and some general results. The more detailed convective models of Chapter 4 are simultaneously more interesting and more difficult to interpret. In particular we consider a cell composed solely of velocity perturbations, a Rayleigh-Bénard model of convective cells, a cold plume descending in a compressible atmosphere, and a slice of a model of turbulent compressible convection. Chapter 5 contains a summary of the results as well as our thoughts concerning future applications of the method.

1.1 Problem Outline

In broad terms, astrophysicists understand the structure of the Sun. The inner 20%, by radius, is known as the core and produces essentially the entirety of the Sun’s energy through thermonuclear fusion. Photons carrying this energy slowly diffuse through the radiative interior to approximately $0.7R_{\odot}$,¹ where a sharp transition occurs. At this radius the Sun becomes convective, meaning that energy transport occurs primarily through bulk fluid motions rather than photon diffusion. The convection zone extends to the solar surface, the photosphere, whereupon photons free-stream outward carrying the Sun’s energy through the solar atmosphere — the chromosphere and corona — and into space.

Although this basic description of solar structure is almost universally accepted, certain details remain contentious. After creating a solar model astrophysicists can compare its structure with the solar structure as inferred from p -mode eigenfrequencies. As can be seen in Figure 1.1, the differences between the two are small but significant. The largest discrepancies occur in three distinct regions: near the solar core, at the tachocline (the boundary between the radiative interior and the convective envelope), and near the solar surface. This work focuses on the discrepancy near the surface which is thought to be partially a consequence of the incomplete treatment of convective motions, both in computing the solar models and in analyzing the helioseismic data. On one hand, solar models based on mixing-length theories of convection slightly miscalculate the interior solar structure and thus disagree with the true Sun. On the other hand, inversions of p -mode eigenfrequencies to determine the solar structure ignore the effects of convective perturbations. Although both effects contribute to the discrepancies seen in Figure 1.1, we will primarily concern ourselves with the latter in this work.

Solar convection is notoriously difficult to model. Important physical processes occur on lengthscales varying by at least 6 orders of magnitude and current simulations (Brummell et al. 1995) fall a factor of more than a billion short of resolving these different scales. Solar modelers, long recognizing the inadequacy of numerical simulations, developed and embraced a

¹ The symbol R stands for radius and the subscript \odot symbolizes the Sun.

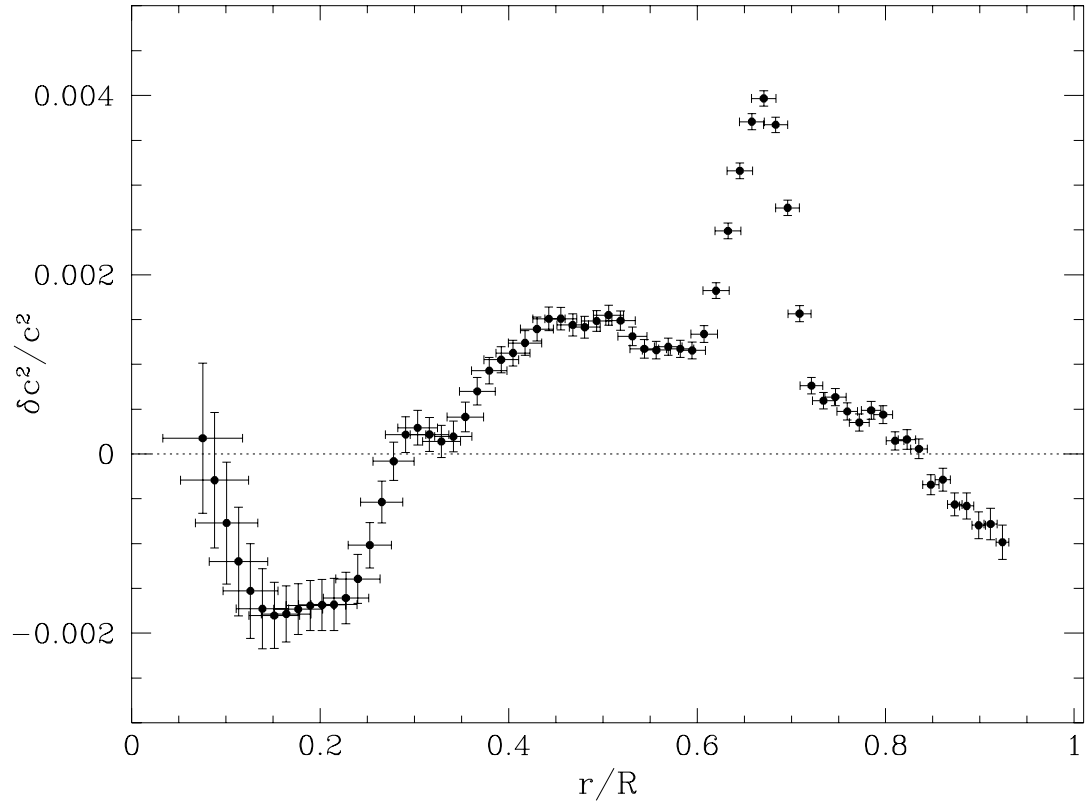


Figure 1.1: The difference between observationally and theoretically determined values of the relative squared sound speed versus solar radius. The observational values come from inversions of p -mode eigenfrequencies while the theoretical values come from a solar model. Courtesy of SOHO/MDI consortium. SOHO is a project of international cooperation between ESA and NASA.

parameterization of the convection zone known as mixing-length theory (see Spiegel 1971, for a review of the field’s development), in which all of the complex convective motions are collapsed into one parameter, the mixing length. Mixing-length theory enjoys the dual benefits of being conceptually simple as well as generally correct — solar models which employ it do a remarkably good job of matching observations. In reality however, the outer portion of the convection zone harbors turbulent convection on scales at least as small as granules (1 Mm) and as big as supergranules (30–50 Mm). In addition, giant cells spanning the entire convection zone (200 Mm) may exist (Beck et al. 1998). The existence of different scales of motion implies mixing-length theory is, at some level, inadequate. Since it is reasonable to assume that the solar convection zone is not precisely described by mixing-length theory, one naturally anticipates disagreements between observational data and theoretical models of the solar sound speed structure.

The inversion methods which deduce the true solar structure of Figure 1.1 from p -mode eigenfrequencies contribute a separate set of errors. Although in principle it is possible to use only the information contained in the eigenfrequencies to reconstruct the solar interior,² the process is computationally difficult. In practice, inversions begin with a reference model such as one of the mixing-length models described above. Eigenfrequencies are computed for the reference model and compared to the solar data; discrepancies are resolved by perturbing the structure of the model so that its eigenfrequencies agree more closely with the observations. Iteration produces the final result, the inverted solar structure (which is hopefully independent of the initial reference model). Any errors in the model stratification will be corrected in the iteration and will not affect the inverted structure. However, current inversion techniques ignore the effects of convective perturbations. Since, as we show in this work, convective structures do affect p -mode eigenfrequencies, not treating their effects will produce errors in the inversion for the true solar structure.

Thus, two possible errors can produce the discrepancies of Figure 1.1. Models of the solar convection zone created with mixing-length theories do not completely describe the average

² Sound speed and density are the most common variables sought in inversions, but other choices, such as the helium abundance, are possible.

interior structure. However, even if models employing mixing-length theory were completely accurate, the true solar structure to which they should be compared is unknown since helioseismic inversions do not account for the effects of convective structures on p -mode eigenfrequencies. In this work we concentrate on the second of these effects and demonstrate that convective motions change p -mode eigenfrequencies by a helioseismically significant amount.

1.2 Solution Method

P modes are three-dimensional analogues of the standing waves (or modes) formed in an organ pipe sounding at one of its natural frequencies. To produce a note in an organ, a sound wave propagates the length of the pipe, reflects from the opposite end and returns down the tube. If the frequency of the sound wave corresponds to a mode of the pipe, the superposition of the counter-propagating waves will resonate, producing a standing wave with the proper frequency. Waves with other frequencies suffer destructive interference and will not produce a tone. A similar mechanism occurs in the Sun, although complicated by spherical geometry, when acoustic waves of the proper frequency and structure resonate to form standing waves — the aforementioned p modes. Unfortunately, this description of p modes, although mathematically correct, causes difficulties with both visualizations and calculations. Ray theory is an alternative approach which simplifies each of these concerns at the expense of being only an approximation to the true, modal, description.

Standing waves are the superposition of traveling waves which can mathematically, to a good approximation, be represented as plane waves — waves with the same amplitude and propagation direction in all of space. Since plane waves travel in only one direction, they are conveniently described by a ray which points parallel to the direction of motion. Interaction of waves with the sides of any enclosure, such as the organ pipe considered above, will cause this approximation to break down. However, if the wavelength of the sound wave is small compared to the dimensions of the enclosure, the effects of the boundary can usually be ignored. Returning to the solar case, if we consider a Sun where any inhomogeneities are large compared to the

wavelength of the p -mode (just as the dimensions of the organ pipe are large compared to the wavelength of the sound wave), then, by analogy, p modes are well approximated by rays.

In the spirit of this approximation, consider a beam of light incident upon a screen with a hole. When the hole is large compared to the wavelength of light, the ray approximation is a valid one and the light travels through the hole in a straight line. However, if the aperture is small compared to the light's wavelength, the light will diffract as it travels through the hole — a phenomenon which can only be explained by considering light as a wave. Within the domain of classical (non-quantum) mechanics, the wave picture will provide the correct description for both situations. Nevertheless, it can be both conceptually and mathematically simpler to use the ray approximation when it is valid. One of the reasons we employ ray theory is precisely this simplicity. Recall that we seek the eigenfrequencies of p modes in a solar model containing turbulent convection. The governing equations for the complete problem are quite difficult — as is, by analogy, solving the problem of light traveling through a large hole using wave theory — particularly for the complex convective motions of the solar interior. By considering p modes whose wavelengths are smaller than the dimensions of the convective motions, we can utilize the simplifying ray approximation.

Until this point, we have been deliberately vague about the nature of the computational advantages provided by using the ray approximation. Mathematical analysis demonstrates that the equations describing the ray-like propagation of a p mode are cast in a special form called Hamilton's equations. Hamilton's equations, which are equivalent to Newton's laws of motion, describe the time evolution of an object's position and momentum and can be used, for instance, to calculate particle trajectories. The correspondence between ray theory and particle propagation may not be surprising after considering the analogy presented above. When light passes through a large aperture, its path can be treated with the ray approximation and is found to be straight lines, just as a beam of particles would behave in a similar situation. Extensive work has focused on systems obeying Hamilton's equations, in particular on determining the eigenfrequencies and modes of oscillation of such systems. By connecting the problem under

consideration (p -mode oscillations in a convective Sun) with Hamiltonian dynamics, we can directly apply these results to the system at hand.

Certain Hamiltonian systems possess quantities known as adiabatic invariants. In some systems — including those with which we are concerned — the adiabatic invariants are found to have special values when the system occupies a mode of oscillation. This property is known as EBK quantization (Einstein 1917; Brillouin 1926; Keller 1958) and suggests that a profitable method for finding eigenmodes of complex systems may be a direct search for those rays whose adiabatic invariants satisfy the quantization conditions. As we will show, this method, although conceptually useful, is unreliable for calculating the eigenfrequencies of sufficiently complex convective models.

However, adiabatic invariants possess another special property; as their name suggests, they are unchanged when the system undergoes slow alterations. We use a technique known as adiabatic switching (reviewed in Skodje & Cary 1988), which relies on both the invariance and the quantization of the adiabatic invariants, to determine the eigenfrequencies of p modes in convective systems. Beginning with a simple model for which theorists can calculate the p mode eigenfrequencies, we choose a ray corresponding to an eigenmode. Doing so ensures the ray possesses correctly quantized adiabatic invariants. Next, we impose a slow alteration onto the envelope in which the ray travels by, for example, gradually increasing the amplitudes of a complicated set of convective motions. Since the adiabatic invariants remain constant during slow changes, they continue to satisfy the correct quantization conditions during the alteration and the ray continues to correspond to an eigenmode. Although the invariants are constant, the eigenfrequency of the ray is not and it slowly changes from its initial value (known from the initial calculation) to a final value, which is not known beforehand. Thus, by comparing the two frequencies, we calculate frequency shifts caused by the convective motions. We will show that this method successfully generates eigenfrequency shifts for complicated convective models. We also demonstrate that these shifts offer a possible solution to the discrepancy between theoretically and observationally based solar models of the structure near the solar

surface.

1.3 Literature Review

The deleterious effects of neglecting fluid motions has been understood for some time and several attempts have been made to untangle the intertwined effects of convection and stellar pulsation (see Baker & Gough 1979, and references therein). Among the first to consider the helioseismic implications was Brown (1984). While considering only vertical velocity perturbations with a zero horizontal average, his work demonstrated that such perturbations always produce eigenfrequency downshifts and suggested that these shifts could be of sufficient magnitude to produce an observable effect. These results are confined to a special subset of photospheric models (those without perturbations in the horizontal direction or to thermodynamic quantities). We confirm them in this work and extend our results to more complicated flows.

Others (Balmforth 1992; Rosenthal 1997; Rosenthal et al. 1998) have examined whether the eigenfrequency discrepancies could be due to other effects, notably turbulent pressure arising from convective motions. Their analysis shows the discrepancy between theory and observation can be reduced, although not enough to bring the two data sets into complete agreement. Furthermore, since the f mode (a surface gravity wave which propagates on the density interface between the photosphere and the chromosphere) is a surface oscillation, it is not affected by the mechanism they consider even though its observed frequencies do not agree with theoretical calculations. From this evidence, they acknowledge that the convective effects which we consider may also be important. They do conclude, however, that the resolution will come from consideration of modal physics, arising from the interaction between p modes and the solar structure, rather than model effects which arise from inaccuracies in the mean solar structure.

A series of papers (Murawski & Roberts 1993a,b; Murawski & Goossens 1993) addresses the effects of photospheric flows and a chromospheric magnetic field on the f mode. Although the oscillation physics of f and p modes are quite different, it is intriguing to note that they find that random photospheric flow fields lower the f -mode frequencies. Although they work in the

incompressible fluid limit, they are able to fit the observational data (which show that the actual f -mode eigenfrequencies are lower than theoretical predictions) with reasonable values for the flow speeds, and magnetic fields. Both Ghosh et al. (1995) and Duvall et al. (1998) extend this work, each showing that several features of the f -mode spectrum can be accounted for by the effects of shearing velocity fields.

More applicable to this work are two papers (Lavelly & Ritzwoller 1992, 1993) which use quasi-degenerate perturbation theory to investigate the effects of steady-state, large-scale convection on helioseismic linewidths and frequencies. In particular, they find that convection on the scale of giant cells (at least in one model) has a systematic effect on the linewidths of p modes and hence that such a signal can be used as a diagnostic tool. Although they also find a small effect on p -mode frequencies, they consider only small to medium harmonic degrees ($\ell \lesssim 100$, where ℓ is defined in §2.1.3) and hence their results do not apply to the same parameter range as ours.

Gruzinov (1998) also uses an analysis based on perturbation theory, but with an emphasis on finding analytic expressions for the eigenfrequency shifts. He derives a general result, in terms of integrals over the flow fields, which he uses to examine turbulent shifts in the f mode. The results include an unobservably small positive frequency shift for low-degree modes, a negative frequency shift at high degrees, and a credible fit with observational data. It is not clear, however, if this method is computationally practical for complicated convective motions.

Also of note is a series of papers investigating acoustic waves in a structured medium (Zhugzhda & Stix 1994; Zhugzhda 1998; Stix & Zhugzhda 1998). They consider corrections arising from a single sinusoidal perturbation to the sound speed and the vertical velocity, ignoring any horizontal flows. Again, they find that the result is a downshift in the eigenfrequencies which increases with both frequency and mode degree ℓ . Furthermore, for solar-like conditions they find that velocity, and not sound speed, perturbations have a stronger effect. As will be shown, our results agree with these although we can extend our analysis to somewhat more complicated flows.

Our first attempts at this problem were motivated by Gough (1993), who discusses EBK quantization (see §2.4) as a means for determining eigenfrequency shifts. He assumes the convective effects are weak, allowing him to use a perturbative expansion and express the frequency shifts in terms of certain integral constraints. As will be shown below, we ultimately abandon this technique in favor of adiabatic switching due to the flexibility of the latter in handling complicated convective motions. Our early work on this subject, portions of Chapters 2–4, has been published elsewhere (Swisdak & Zweibel 1999).

Chapter 2

Theoretical Justification

This chapter provides the theoretical justification for our approach to the problem. In §2.1 we discuss the theory of stellar oscillations and derive the governing differential equation. In §2.2, we describe the WKB solution to this equation and show how it can be cast in terms of the ray approximation. Section 2.3 outlines the general properties of Hamiltonian systems. The use of EBK quantization to find Hamiltonian eigenvalues is discussed in §2.4. Finally, in §2.5, we give a synopsis of the method of adiabatic switching, treating both its theoretical underpinnings and its application to the specific problem at hand.

2.1 Stellar Oscillations

The theory of stellar oscillations is a well explored field with results ranging far wider than is necessary for this work. The basic mathematics is well known and we present only a brief summary of the germane topics; for more details, consult one of the many available references (Cox 1980; Gough 1993; Christensen-Dalsgaard 1997).

2.1.1 Fluid Equations

To derive the equations governing p -mode oscillations, we begin with the equations of fluid dynamics; for a derivation of these equations starting from Newtonian mechanics see Fetter & Walecka (1980). The mass conservation, or continuity, equation is

$$\frac{\partial \rho}{\partial t} + \nabla \cdot (\rho \mathbf{v}) = 0, \quad (2.1)$$

where ρ and \mathbf{v} are the fluid density and velocity, respectively.¹ Solar Reynolds numbers are $\gtrsim 10^{12}$ (Brummell et al. 1995), implying that the viscous terms in the Navier-Stokes (conservation of momentum) equation are unimportant. We note that, even though they are numerically small, the dissipative effects of viscosity can have significant effects on p modes, particularly in the outer convection zone. We ignore them here, however, and take

$$\frac{\partial \mathbf{v}}{\partial t} + (\mathbf{v} \cdot \nabla) \mathbf{v} = -\frac{1}{\rho} \nabla p + \mathbf{f}, \quad (2.2)$$

where p represents pressure and \mathbf{f} is the sum of all body forces per unit mass. In this work, the only body force we consider is gravity, so $\mathbf{f} = \mathbf{g}$ where \mathbf{g} is the acceleration due to gravity.² The gravitational acceleration also satisfies Poisson's equation,

$$\nabla \cdot \mathbf{g} = \nabla^2 \Phi = -4\pi G \rho, \quad (2.3)$$

for the gravitational potential Φ , where G is the Newtonian gravitational constant. A final relation is necessary to complete the set of equations. Beginning with the first law of thermodynamics and assuming that the fluid motions are adiabatic, it may be shown that the pressure and density are related by:

$$\frac{dp}{dt} = \frac{\Gamma_1 p}{\rho} \frac{d\rho}{dt} = c^2 \frac{d\rho}{dt}, \quad (2.4)$$

where the adiabatic exponent is

$$\Gamma_1 = \left(\frac{\partial \ln p}{\partial \ln \rho} \right)_s, \quad (2.5)$$

with the subscript s indicating that the derivative is taken at constant specific entropy. Equation (2.4) also defines the adiabatic sound speed c .

Justification for the assumption of adiabatic fluid motions in the context of p -mode oscillations comes from an examination of the relevant timescales. The motion of a fluid element may be approximated as adiabatic if the element undergoes several oscillations before heat is

¹ Appendix A contains a table of important symbols used in this work.

² Although Lorentz forces arising from magnetic fields could also be included, their effects in the solar convection zone are usually significant only in active regions. We disregard them here.

transferred between it and the surroundings. In other words, the oscillation timescale must be shorter than the timescales for radiation and convection, the relevant heat transfer mechanisms in the Sun. The canonical period of a solar p -mode is 5 minutes. In the solar convection zone the radiation timescale is $\approx 10^2$ years, which is significantly longer than an oscillation period.³ Convective timescales, however, are much shorter. Observations show that granules have lifetimes of ≈ 10 minutes. Larger convective motions such as mesogranules (≈ 1 hour lifetimes) and supergranules (≈ 1 day lifetimes) have been detected and giant cells persisting for a solar rotation period of 30 days may also exist. Granules, with lifetimes of $\approx 1 - 2$ oscillation periods, clearly violate the assumption of adiabatic fluid motions. But, as will be shown below, p modes rarely occupy the same regions as granules, hence justifying our dismissal of their non-adiabatic effects.

2.1.2 Perturbations

The amplitudes of solar oscillations are small in comparison to other fluid motions in the Sun. The first discovery of p modes (Leighton et al. 1962) showed the solar surface to be tiled with oscillating fluid elements having a characteristic velocity amplitude of 1 km s^{-1} . Later observations found that these oscillations are the superposition of $\approx 10^7$ p modes with individual amplitudes of $\approx 1 \text{ m s}^{-1}$. For comparison, the adiabatic sound speed near the photospheric surface is $c \approx 10 \text{ km s}^{-1}$; in the interior the sound speed rapidly rises while the oscillation amplitude falls. The resulting Mach numbers, $\approx 10^{-4}$ at the surface maximum, imply p modes are linear oscillations, an assumption we carry throughout this work.

We seek oscillations about a reference state satisfying equations (2.1)–(2.4) and certain (unspecified) boundary conditions. As p -mode oscillations are small, we use linear perturbation theory. Assuming the existence of a static,⁴ spherically symmetric reference model satisfying equations (2.1)–(2.4), we expand each variable around its equilibrium state. Any variable Q

³ The radiation timescale drastically decreases at the photosphere. However, processes in this region cause difficulties for several reasons, as will be seen below, and are ignored in this work.

⁴ Direct observation supports this assumption as the mean solar structure does not vary on the timescales in question.

becomes

$$Q(\mathbf{x}, t) = Q_0(\mathbf{x}) + Q'(\mathbf{x}, t), \quad (2.6)$$

where \mathbf{x} is the position vector, Q_0 is the variable evaluated in the reference model and Q' is an Eulerian perturbation. (For a full description of Eulerian and Lagrangian perturbations, see Appendix B.)

To continue, we replace the variables in equations (2.1)–(2.4) with their linearized counterparts, dropping the 0 subscripts from reference quantities. The continuity equation becomes

$$\rho' + \nabla \cdot (\rho \delta \mathbf{x}) = \delta \rho + \rho \nabla \cdot (\delta \mathbf{x}) = 0, \quad (2.7)$$

where δ represents a Lagrangian perturbation, while the momentum equation is

$$\rho \frac{\partial^2 \delta \mathbf{x}}{\partial t^2} = -\nabla p' + \rho \mathbf{g}' + \rho' \mathbf{g}. \quad (2.8)$$

From the adiabatic approximation of equation (2.4), the density and pressure perturbations are connected through

$$\delta p = c^2 \delta \rho. \quad (2.9)$$

Finally, Poisson's equation becomes

$$\nabla^2 \Phi' = \nabla \cdot \mathbf{g}' = -4\pi G \rho'. \quad (2.10)$$

2.1.3 Separation of Angular Variables

Since the reference state is spherically symmetric, it proves helpful to consider the angular behavior of the independent variables in spherical coordinates (r, θ, ϕ) . After rewriting the perturbed form of Poisson's equation (2.10) as

$$\frac{1}{r^2} \frac{\partial}{\partial r} \left(r^2 \frac{\partial \Phi'}{\partial r} \right) + \nabla_h^2 \Phi' = -4\pi G \rho', \quad (2.11)$$

we see that derivatives with respect to the angular variables θ and ϕ appear solely as part of the horizontal Laplacian

$$\nabla_h^2 = \frac{1}{r^2 \sin \theta} \frac{\partial}{\partial \theta} \left(\sin \theta \frac{\partial}{\partial \theta} \right) + \frac{1}{r^2 \sin^2 \theta} \frac{\partial^2}{\partial \phi^2}. \quad (2.12)$$

Assuming that ρ' and Φ' have the same angular dependence, separation of the angular coordinates, leads to the well known result that the angular eigenfunctions are the spherical harmonics, $Y_\ell^m(\theta, \phi)$. To be precise, we have

$$\rho'(\mathbf{x}, t) = \rho'(r, t)Y_\ell^m(\theta, \phi) \quad (2.13)$$

$$\Phi'(\mathbf{x}, t) = \Phi'(r, t)Y_\ell^m(\theta, \phi), \quad (2.14)$$

where ℓ , a non-negative integer, is the degree of the harmonic, while m is restricted to the range $-\ell \leq m \leq \ell$ and is called the azimuthal order. Given equations (2.13)–(2.14), we can show that the spherical harmonics are also the angular eigenfunctions of the other scalar perturbations.

Although the spherical harmonics are familiar from other problems of mathematical physics, it is useful to discuss a few of their properties as they relate to p -mode structure. A full solution of the eigenvalue problem produces radial eigenfunctions $\rho'(r, t)$ demarcated by an integer n ; the full eigenfunctions $\rho'(\mathbf{x}, t)$ are then denoted by three integers: n , ℓ and m . The radial eigenvalue roughly measures the number of oscillations in the radial direction, ℓ and m characterize the oscillations on a spherical surface. Hence as n and ℓ increase, the radial and azimuthal wavelengths decrease.

The solar acoustic structure traps p modes in a radial cavity. Within the cavity the mode resonates and produces a standing wave, while outside of the cavity the mode is evanescent. The radial location of the cavity depends on the mode numbers, roughly increasing linearly with ℓ and decreasing linearly with n . For $n = 1$, $\ell > 15$ the cavity of a p mode is confined within the solar convection zone ($r \gtrsim 0.7R_\odot$) and oscillations with $n = 1$, $\ell > 80$ have a minimum radius of $0.95R_\odot$.

2.1.4 Derivation of a Wave Equation

Equations (2.7)–(2.10) may be recast in a suggestive form through a derivation of Gough (1993) based on the earlier work of Lamb (1932). Define the variable

$$\chi \equiv \nabla \cdot \delta \mathbf{x} = -\frac{\delta \rho}{\rho} = -\frac{\delta p}{c^2 \rho}, \quad (2.15)$$

where the last two equalities follow from equations (2.7) and (2.9). Substituting equation (2.15) into the perturbed momentum equation (2.8) yields

$$\rho \frac{\partial^2 \delta \mathbf{x}}{\partial t^2} = -\nabla(\rho \delta \mathbf{x} \cdot \mathbf{g} - \rho c^2 \chi) + \rho \mathbf{g}' - \rho \chi \mathbf{g} - (\delta \mathbf{x} \cdot \nabla \rho) \mathbf{g}, \quad (2.16)$$

where we have made use of the equation of hydrostatic equilibrium, $\nabla p = \rho \mathbf{g}$, and equation (B.10). Dividing through by ρ and rearranging, we find that

$$\frac{\partial^2 \delta \mathbf{x}}{\partial t^2} = \nabla(c^2 \chi + \delta \mathbf{x} \cdot \mathbf{g}) + c^2 \chi \frac{\nabla \rho}{\rho} + \delta \mathbf{x} \cdot \mathbf{g} \frac{\nabla \rho}{\rho} + \mathbf{g}' - \chi \mathbf{g} - \frac{1}{\rho} (\delta \mathbf{x} \cdot \nabla \rho) \mathbf{g}. \quad (2.17)$$

The curl of the equation of hydrostatic equilibrium shows that \mathbf{g} and $\nabla \rho$ are parallel and allows us to cancel the third and sixth terms on the right-hand side. After a small rearrangement, we have

$$\frac{\partial^2 \delta \mathbf{x}}{\partial t^2} = \nabla(c^2 \chi + \delta \mathbf{x} \cdot \mathbf{g}) + (c^2 \frac{\nabla \rho}{\rho} - \mathbf{g}) \chi + \mathbf{g}'. \quad (2.18)$$

Finally, recall that the reference state was assumed to be spherically symmetric. Denoting the radial unit vector as $\hat{\mathbf{r}}$ gives $\mathbf{g} = -g(r)\hat{\mathbf{r}}$ and defining the radial component of the Lagrangian displacement as

$$\xi \equiv \hat{\mathbf{r}} \cdot \delta \mathbf{x} \quad (2.19)$$

produces

$$\frac{\partial^2 \delta \mathbf{x}}{\partial t^2} = \nabla(c^2 \chi - g\xi) + (c^2 \frac{\nabla \rho}{\rho} + g\hat{\mathbf{r}}) \chi + \mathbf{g}'. \quad (2.20)$$

We can proceed further, using equations (2.10), (2.15), and (B.10) to substitute for \mathbf{g}' and obtain an equation for $\delta \mathbf{x}$ only in terms of the parameters of the reference model. A more fruitful approach comes from making several well motivated and simplifying assumptions which we discuss below.

2.1.4.1 Cowling's Approximation

In making Cowling's approximation we assume that Φ' , the perturbation to the gravitational potential due to the oscillations, is negligible compared to the density variation ρ' and

thus that we can neglect \mathbf{g}' in equation (2.20). First demonstrated by Cowling (1941), it arises from a consideration of the solution to the perturbed Poisson's equation (2.10) in integral form:

$$\Phi'(r) = \frac{4\pi G}{2\ell + 1} \left[r^\ell \int_r^\infty \rho'(x) x^{1-\ell} dx + r^{-1-\ell} \int_0^r \rho'(x) x^{\ell+2} dx \right]. \quad (2.21)$$

The perturbed potential Φ' may be safely neglected when the spherical harmonic degree is large, as both integrals contain terms which rapidly decay with increasing ℓ . In addition, Φ' can safely be neglected in modes where ρ' rapidly changes sign, which happens when n is large. Since factors we discuss in §2.2 restrict our investigation to modes with $\ell \gtrsim 100$, we hereby set $\mathbf{g}' = 0$ in what follows.

2.1.4.2 Further Approximations

Since we desire oscillatory solutions, we expect the governing equation to be similar in form to the standard wave (Helmholtz) equation for a scalar variable. After making Cowling's approximation, equation (2.20) becomes

$$\frac{\partial^2 \delta \mathbf{x}}{\partial t^2} = \nabla(c^2 \chi - g\xi) + \beta \chi \hat{\mathbf{r}}. \quad (2.22)$$

where

$$\beta \equiv \frac{c^2}{\rho} \frac{d\rho}{dr} + g = -\frac{c^2 N^2}{g} \quad (2.23)$$

and N is the Brunt-Väisälä frequency. Modes of high spherical degree occupy a cavity with a small radial extent near the top of the convection zone. As a simple, but useful, approximation we take gravity to be constant throughout this region and simplify the governing equations. To be precise, we assume the variation of gravity on the vertical scale of the oscillations is small and hence that all derivatives of g with respect to r vanish.⁵

After applying the divergence operator $\nabla \cdot$ to equation (2.22), we have

$$\frac{\partial^2 \chi}{\partial t^2} = \nabla^2(c^2 \chi - g\xi) + \hat{\mathbf{r}} \cdot \nabla(\beta \chi) + \frac{2\beta \chi}{r}. \quad (2.24)$$

⁵ To be consistent we should work in the plane-parallel limit $r \rightarrow \infty$. However for now we keep terms depending inversely on r noting that they, by chance, disappear from the final result of equation (2.30). For a consistent treatment see Appendix C.

To eliminate the variable $\nabla^2\xi$, apply the operator $\hat{\mathbf{r}} \cdot (\nabla \times \nabla \times$ to equation (2.22). Using various vector identities we obtain

$$\frac{\partial^2}{\partial t^2}(\hat{\mathbf{r}} \cdot \nabla \chi - \nabla^2 \xi) = -\nabla_h^2(\beta \chi) - \frac{2\beta \chi}{r^2}, \quad (2.25)$$

where ∇_h^2 is the horizontal Laplacian operator. Combining equations (2.24) and (2.25) gives

$$\frac{\partial^4 \chi}{\partial t^4} - \frac{\partial^2}{\partial t^2} \left(\nabla^2(c^2 \chi) + \hat{\mathbf{r}} \cdot \nabla [(\beta - g)\chi] + \frac{2\beta \chi}{r} \right) + \frac{2\beta g \chi}{r^2} + g \nabla_h^2(\beta \chi) = 0. \quad (2.26)$$

Since this equation contains odd spatial derivatives of χ , it is not quite in the desired Helmholtz-like form. The substitution $\Psi = c^2 \rho^{1/2} \chi = -\rho^{-1/2} \delta p$ eliminates the odd-order derivatives and gives

$$\frac{\partial^4 \Psi}{\partial t^4} - \left(c^2 \nabla^2 - \omega_c^2 - \frac{2\beta \chi}{r} \right) \frac{\partial^2 \Psi}{\partial t^2} - \left(c^2 N^2 \nabla_h^2 - \frac{2\beta g c^2}{r^2} \right) \Psi = 0. \quad (2.27)$$

The acoustic cutoff frequency ω_c is defined by

$$\omega_c^2 \equiv \frac{c^2}{4H_\rho^2} \left(1 - 2\hat{\mathbf{r}} \cdot \nabla H_\rho - \frac{4H_\rho}{r} \right) \quad (2.28)$$

where

$$H_\rho \equiv - \left(\frac{d \ln \rho}{dr} \right)^{-1} \quad (2.29)$$

is the density scale height.

Solar convection is so efficient that the underlying reference state is nearly adiabatically stratified. Non-adiabatic stratification is a significant effect only in the outer portions of the convection zone where other aspects of our analysis (primarily the assumption of adiabatic fluid motions) also break down. Thus N^2 (and therefore β) are ≈ 0 in the bulk of the convection zone, the region of interest in this analysis. Neglecting the appropriate terms in equation (2.27), we arrive at a modified wave equation

$$\left(\frac{\partial^2}{\partial t^2} + \omega_c^2 \right) \Psi - c^2 \nabla^2 \Psi = 0. \quad (2.30)$$

The analysis leading to equation (2.30) required several assumptions. In roughly the order of occurrence, they are

- (a) Non-dissipative, adiabatic fluid motions
- (b) Linear perturbations
- (c) Spherically symmetric, non-magnetic, static reference state
- (d) Cowling's approximation
- (e) Constant gravity
- (f) Adiabatic stratification.

Appendix C discusses the ramifications of relaxing restrictions (e) and (f). Note that the derivation of equation (2.30) did not assume a plane-parallel geometry, only that variations in the gravitational acceleration are small over the region of interest. Below we will adopt a plane-parallel geometry, the only effect of which is to eliminate the final term in equation (2.28).

2.2 Asymptotic Approximations

The ultimate goal is to determine the eigenfrequencies of a solar model which includes convective motions. In principle this means solving equation (2.30) in a domain where c and ω_c are complicated functions of position — a difficult computational problem which has the potential to obfuscate the underlying physics within a morass of numerical work. Instead, we seek the eigenvalues for a particular limit of the general problem, the short-wavelength limit where the lengthscales of the oscillations are much shorter than those of the other varying quantities. Since, for example, a p mode with an $\ell = 200$ has a typical horizontal length scale of $R_\odot/\ell = 3.5$ Mm, our analysis will only be valid for convective motions of mesogranular scales and larger. Of course, as granules already violate the assumption of adiabatic fluid motions used in the derivation of equation (2.30), our mathematical formalism has already implicitly excluded these motions. On the other hand, granulation near the solar surface is the leading candidate for the source of p modes and hence would be expected to leave an imprint on the oscillation frequencies. Our analysis is insensitive to any such signal. The short-wavelength approximation,

also known as geometrical acoustics or optics, is equivalent to the WKB method used in the asymptotic analysis of differential equations.

Our assumption of small-wavelength modes allows us to use the well known analogy between geometrical optics and particle motion to cast the problem in a Hamiltonian formalism. A method analogous to EBK semi-classical quantization then provides a relatively simple route to the desired eigenvalues. However, we will demonstrate that this method is difficult, if not impossible, to implement for the complicated domains under consideration. However, due to the Hamiltonian nature of the system, a related technique known as adiabatic switching produces eigenvalues even for complex systems.

Consider, for the moment, an unrealistic solar model where $\omega_c = 0$ and c is a constant. Equation (2.30) reduces to the Helmholtz equation, which has plane-wave solutions

$$\Psi = \Psi_0 e^{\pm i(\mathbf{k}\cdot\mathbf{x} - \omega t)}, \quad (2.31)$$

where Ψ_0 is the constant amplitude of the wave and the wavenumber \mathbf{k} and frequency ω are related by the dispersion relation $\omega^2 = c^2 k^2$. These plane waves have the distinctive property that their propagation directions and amplitudes are the same for all space. In this case, we can actually ignore the wave nature of equation (2.31) and treat the solution as a one-dimensional ray, propagating perpendicular to the wavefronts.

Now, consider instead a system where the lengthscale over which equilibrium quantities (such as c , p and ρ) vary is much longer than the wavelength of a mode. Letting the ratio of these lengthscales be denoted by Λ ($\sim H_\rho |\mathbf{k}|$) — a constant, large parameter used for bookkeeping purposes — we write the solution to equation (2.30) as a plane wave with varying amplitude, A , and phase, φ (assumed to be real):

$$\Psi = A(\mathbf{x}, t) e^{i\Lambda\varphi(\mathbf{x}, t)}. \quad (2.32)$$

Although we have not made any approximations in assuming this form for the solution, the presence of Λ suggests that Ψ rapidly oscillates in comparison to the background state. Thus, it is reasonable to think of equation (2.32) as describing waves which are locally planar and hence

amenable to a ray description, albeit one where the rays undergo changes in both direction and amplitude during propagation. If, as is the case for p modes, an eigenmode is trapped within a cavity the wavenumber of the solution disappears at the boundaries. There, $\Lambda \rightarrow 0$ and it is impossible to satisfy the locally planar condition. This difficulty is merely the well known breakdown of the WKB approximation near the classical turning points of a trajectory.

Using the ansatz of equation (2.32) and following the work of Gough (1993), we expand equation (2.30) and equate powers of Λ . This process, equivalent to the WKB approximation, gives the leading equation

$$\left(\frac{\partial\varphi}{\partial t}\right)^2 - \left(\frac{\omega_c}{\Lambda}\right)^2 - c^2 |\nabla\varphi|^2 = 0. \quad (2.33)$$

In a slightly different form, this is the eikonal equation of geometric optics. Next, making the analogy between equations (2.31) and (2.32), we define the local frequency $\tilde{\omega}$ and wavenumber \mathbf{k} as

$$\tilde{\omega}(\mathbf{x}, t) \equiv -\Lambda \frac{\partial\varphi}{\partial t} \quad \text{and} \quad \mathbf{k}(\mathbf{x}, t) \equiv \Lambda \nabla\varphi. \quad (2.34)$$

These identifications allow us to write equation (2.33) in the form of a dispersion relation:

$$\omega(\mathbf{x}, \mathbf{k}, t) = (c^2 k^2 + \omega_c^2)^{\frac{1}{2}}, \quad (2.35)$$

where ω differs from $\tilde{\omega}$ only in the inclusion of \mathbf{k} as an independent variable. Furthermore, equation (2.34) also implies that

$$\frac{\partial\mathbf{k}}{\partial t} + \nabla\tilde{\omega} = 0, \quad (2.36)$$

from which we find that

$$\left(\frac{d\mathbf{k}}{dt} + \nabla\omega\right) + \left(\frac{\partial\omega}{\partial\mathbf{k}} - \frac{d\mathbf{x}}{dt}\right) \cdot \nabla\mathbf{k} = 0, \quad (2.37)$$

where $\frac{d}{dt}$ is the total derivative with respect to time along a ray path. As the grouping of the terms suggests, this equation is satisfied when each expression is identically zero. The result is a set of first-order differential equations which describe the trajectory of a ray:

$$\frac{d\mathbf{k}}{dt} = -\frac{\partial\omega}{\partial\mathbf{x}} \quad \text{and} \quad \frac{d\mathbf{x}}{dt} = \frac{\partial\omega}{\partial\mathbf{k}}. \quad (2.38)$$

Equations (2.38) are Hamilton's equations for a Hamiltonian ω in terms of the canonical positions $q_i = x_i$ and momenta $p_i = k_i$. The dispersion relation of the ray, $\omega(\mathbf{x}, \mathbf{k}, t)$, is identified as the functional form of the Hamiltonian. Using the WKB approximation we have recast the original problem; instead of solving the eigenvalue problem presented by the partial differential equation (2.30), we seek the eigenfrequencies of the Hamiltonian given by equation (2.35). This reworking comes at a price since once we pass to a ray description we lose information concerning the structure of the eigenmode. However, we are primarily concerned with the eigenfrequencies which, as we will show, can be determined in a straightforward manner for the Hamiltonian systems under consideration.

While the appearance of Hamilton's equations may appear serendipitous, it has been known since the time of Hamilton himself that the eikonal equation is equivalent to the Hamilton-Jacobi equation of classical mechanics. As an aside, it is well known in quantum mechanics (Goldstein 1965) that high-frequency solutions to the wave equation (in other words, solutions which oscillate rapidly compared to any background variation) follow ray-like trajectories similar to classical particles. In that case, the semi-classical limit, the inverse of Planck's constant, \hbar^{-1} , plays an analogous role to our parameter Λ .

Finally, the dispersion relation of equation (2.35) is not a fully satisfactory description of ray motion in a convective domain. While it does describe the trajectory of a ray in a Sun where c and ω_c are arbitrary functions of position, any method which wishes to treat realistic convective structures must also consider the possibility of advective motions. This oversight is a result of our initial description of the problem: equations (2.7)–(2.10) do not allow for fluid motions in the reference state and hence they do not appear in the final dispersion relation. To account for this discrepancy, we will add a term to equation (2.35) in §3.2 which takes the form of a Doppler shift and accounts for the effects of advective motions.

2.3 Hamiltonian Systems

The identification with Hamiltonian mechanics allows us to take advantage of the extensive results available for Hamiltonian systems. Before discussing how to find the eigenfrequencies for such systems, we review several results from Hamiltonian theory which will be of use in later sections. More details on these subjects can be found in a number of texts on classical mechanics and Hamiltonian systems (for example Goldstein 1965; Arnold 1978; Lichtenberg & Lieberman 1983; Tabor 1989).

A general Hamiltonian $H(\mathbf{q}, \mathbf{p}, t)$, satisfies Hamilton's equations

$$\frac{d\mathbf{q}}{dt} = \frac{\partial H}{\partial \mathbf{p}} \quad \text{and} \quad \frac{d\mathbf{p}}{dt} = -\frac{\partial H}{\partial \mathbf{q}} \quad (2.39)$$

for the canonical position vector \mathbf{q} and canonical momentum vector \mathbf{p} . If the Hamiltonian is cyclic in one of the canonical positions q_i (i.e., the Hamiltonian does not explicitly depend on that coordinate), then the corresponding canonical momentum p_i is also a constant of the motion:

$$\frac{\partial H}{\partial q_i} = 0 \quad \text{implies} \quad \frac{dp_i}{dt} = 0. \quad (2.40)$$

Furthermore, the time derivative of H is given by

$$\frac{dH}{dt} = \frac{\partial H}{\partial t} + \frac{\partial H}{\partial \mathbf{q}} \frac{d\mathbf{q}}{dt} + \frac{\partial H}{\partial \mathbf{p}} \frac{d\mathbf{p}}{dt} = \frac{\partial H}{\partial t}, \quad (2.41)$$

where the final equality follows from equation (2.39). Hence, for systems where the Hamiltonian is not explicitly time-dependent, the Hamiltonian itself is a constant of the motion. Finally, we note that if a Hamiltonian of degree n does contain an explicit time-dependence, it is possible to rewrite it as a time-independent Hamiltonian of degree $n + 1$ in which the time and the old Hamiltonian become elements of the canonical position and momentum vectors, respectively.

Certain special Hamiltonians, named integrable systems, have equal numbers of independent constants of the motion and degrees of freedom. Such systems permit a canonical transformation (one which preserves the Hamiltonian nature of the system) in which all of the

new canonical positions, usually termed angle variables and denoted Θ_k , are cyclic. The new canonical momenta are the action variables I_k , and the transformed Hamiltonian $H(I_k)$ satisfies a certain set of Hamilton's equations:

$$\frac{dI_k}{dt} = -\frac{\partial H}{\partial \Theta_k} = 0 \quad \text{and} \quad \frac{d\Theta_k}{dt} = \frac{\partial H}{\partial I_k} = \nu_k(\mathbf{I}), \quad (2.42)$$

where ν_k is the characteristic frequency for motion in the k th coordinate.⁶ Since the angles are cyclic, each action variable is one of the n independent constants of the motion.

Thus, a Hamiltonian system with n degrees of freedom defines a $2n$ -dimensional phase space, but integrability ensures that the phase-space trajectories are confined to $(2n - n) = n$ -dimensional surfaces. It can be shown both that this surface is topologically equivalent to an n -dimensional torus and that the action variables may be written as

$$I_k = \frac{1}{2\pi} \oint_{C_k} \mathbf{p} \cdot d\mathbf{q}, \quad (2.43)$$

for $k = 1, \dots, n$. The curves C_k are topologically independent closed paths on the n -dimensional torus. An integrable system is confined to a torus by its initial conditions (which set the values of the invariant action variables) and does not stray from this torus as long as the system remains integrable.

A concrete example is provided by a two degree of freedom Hamiltonian; in particular, we shall consider equation (2.35). In the appropriate notation, the Hamiltonian (ω) is written as

$$H(q_1, q_2, p_1, p_2) = \sqrt{c^2(p_1^2 + p_2^2) + \omega_c^2} \quad (2.44)$$

where the sound speed c and the acoustic cut-off frequency ω_c are functions of the canonical positions q_1 and q_2 . The system has two degrees of freedom and thus a four-dimensional phase space. As the Hamiltonian is independent of time, H itself is a constant of the motion. Furthermore, if we specialize to a system where c and ω_c are both independent of one of the position coordinates, say q_1 , then the corresponding wavenumber p_1 is also a constant of the motion. The

⁶ These are usually represented as ω_k . To avoid confusion with the acoustic cutoff frequency ω_c and the Hamiltonian ω , we adopt this non-standard notation.

existence of two constants ensures the integrability of the system and restricts phase-space motions to a two-dimensional surface, topologically equivalent to a familiar two-dimensional torus. In fact, a family of invariant tori exist, each individual torus corresponding to a particular pair (H, q_1) . As the tori do not intersect, initial conditions constrain the system to a particular torus for all time. To write the Hamiltonian of equation (2.44) in action-angle coordinates requires the specification of the functional form of c and ω_c and would lead us astray at this time. We return to the subject in Chapter 3.

General Hamiltonian systems, however, are usually non-integrable and thus their trajectories are not confined to n -dimensional phase-space tori. However, special attention has been given to systems which are nearly-integrable in the sense that they may be written as

$$H = H_0(\mathbf{I}) + \epsilon H_1(\mathbf{I}, \Theta), \quad (2.45)$$

where \mathbf{I} and Θ are vectors of the action and angle coordinates, respectively, and ϵ is a small parameter. The fate of invariant tori in non-integrable systems is addressed by the KAM (Kolmogorov-Arnold-Moser) theorem. We will return to the implications of this theorem in later sections, but roughly it states that for sufficiently small values of ϵ , most invariant tori are preserved. In other words, for small perturbations from integrability, most sets of initial conditions remain on invariant tori. However, the destroyed and invariant tori are intermingled in phase space and as the strength of the perturbation increases, so does the density of the destroyed tori. For a strong enough perturbation, no invariant tori remain.

2.4 Quantization Conditions

We now return to the question of determining the eigenfrequencies of a convective solar model. Before deriving the p -mode quantization conditions, we briefly digress with a discussion of semi-classical EBK quantization as it is formulated in quantum mechanics. Then, we examine a simple solar model to derive insight into the behavior of the ray solutions. Finally, we determine the p -mode quantization conditions and discuss their implications.

2.4.1 EBK Quantization

Prior to the development of wave and matrix mechanics, quantum theory postulated that the correct description of the quantum world arose from quantizing the classical action variables. Perhaps the most familiar example is Bohr's derivation of the hydrogen spectra from the quantization of orbital angular momentum. The general result is displayed in the Bohr-Sommerfeld-Wilson quantization condition:

$$I_j = \oint_{C_j} p_j dq_j = n_j h, \quad (2.46)$$

where h is Planck's constant, n_j is an integer, and C_j is the closed contour associated with the motion in the j th degree of freedom. Disregarding the factor of 2π , this action is slightly different than that of equation (2.43) since it assumes that motions in different coordinates are separable. But, it was quickly realized that the separation procedure is not unique: evaluation in different coordinate systems produces different quantization conditions. As an additional defect, the zero-point energy ($n_j \rightarrow n_j + 1/2$) found in, for example, the quantum harmonic oscillator, could not be accounted for with equation (2.46) and was added as an empirical correction.

Einstein (1917) proposed a solution to the first of these problems by noting that since the quantity $\mathbf{p} \cdot d\mathbf{q}$, unlike the individual terms $p_j dq_j$, is invariant under coordinate transformations, the action variable to be quantized should be that given in equation (2.43). Soon thereafter, modern quantum theory arose and it was discovered that Schrödinger's wave equation reduced to the Hamilton-Jacobi equation (and hence classical mechanics) in the semi-classical limit of $h \rightarrow 0$. Brillouin (1926), working in this limit, confirmed Einstein's supposition concerning the form of the quantized action variables by requiring that the wavefunction solutions be single-valued. Finally, Keller (1958) added a term to the quantization condition which accounts for phase loss at caustic surfaces.⁷ The result is EBK semi-classical quantization which states that

⁷ Caustics occur when rays converge onto a lower-dimensional surface. A telescope focus, where a three-dimensional bundle of rays coalesces to a point, is one example.

for quantum phenomena the classical action variable I_k of equation (2.43) is quantized:

$$I_k = \frac{1}{2\pi} \oint_{C_k} \mathbf{p} \cdot d\mathbf{q} = \hbar \left(n_k + \frac{s_k}{4} \right), \quad (2.47)$$

where n_k is an integer and s_k , Keller's contribution, is the number of encountered caustics. It is interesting to note that the final term can naturally account for the zero-point energy absent from the Bohr-Sommerfeld-Wilson quantization condition.

2.4.2 A Simple Physical Model

Before deriving the appropriate quantization conditions for p modes, we first examine a simple system for some physical insight into the procedure. In §2.2 we demonstrated that, in the small-wavelength limit, the solutions to equation (2.30) are rays. For now we work in plane polar coordinates (r, ϕ) , use the simplified dispersion relation $\omega^2 = c^2 k^2$, and assume that c is azimuthally symmetric, $c = c(r)$. The equations governing ray motion are found from equation (2.38):

$$\frac{dr}{dt} = \frac{c^2 k_r}{\omega} \quad \text{and} \quad r \frac{d\phi}{dt} = \frac{c^2 k_\phi}{\omega}, \quad (2.48)$$

and the raypaths are solutions to

$$\frac{dr}{d\phi} = \frac{rk_r}{k_\phi} = r \sqrt{\frac{\omega^2}{c^2 k_\phi^2} - 1}. \quad (2.49)$$

In order to proceed, we need to specify several quantities: the form of $c(r)$, a frequency ω (a constant of the motion as c is independent of time), an azimuthal wave number k_ϕ (another constant as c is independent of ϕ), and initial conditions. For a given c , certain combinations of ω and k_ϕ will yield eigenmodes (we discuss below how to find these combinations), however raypaths still exist even for non-modal values of those parameters. Choosing a reasonable form for the sound speed,⁸ as well as values for ω and k_ϕ , results in the raypath shown in Figure 2.1.

Some general features of the raypath, independent of the initial conditions or specific values of ω and k_ϕ , are noteworthy. A raypath propagates within a well defined radial cavity

⁸ Although the actual form is not important, we use a polytrope with $c^2 \propto r$. Polytopes are discussed further in §3.1

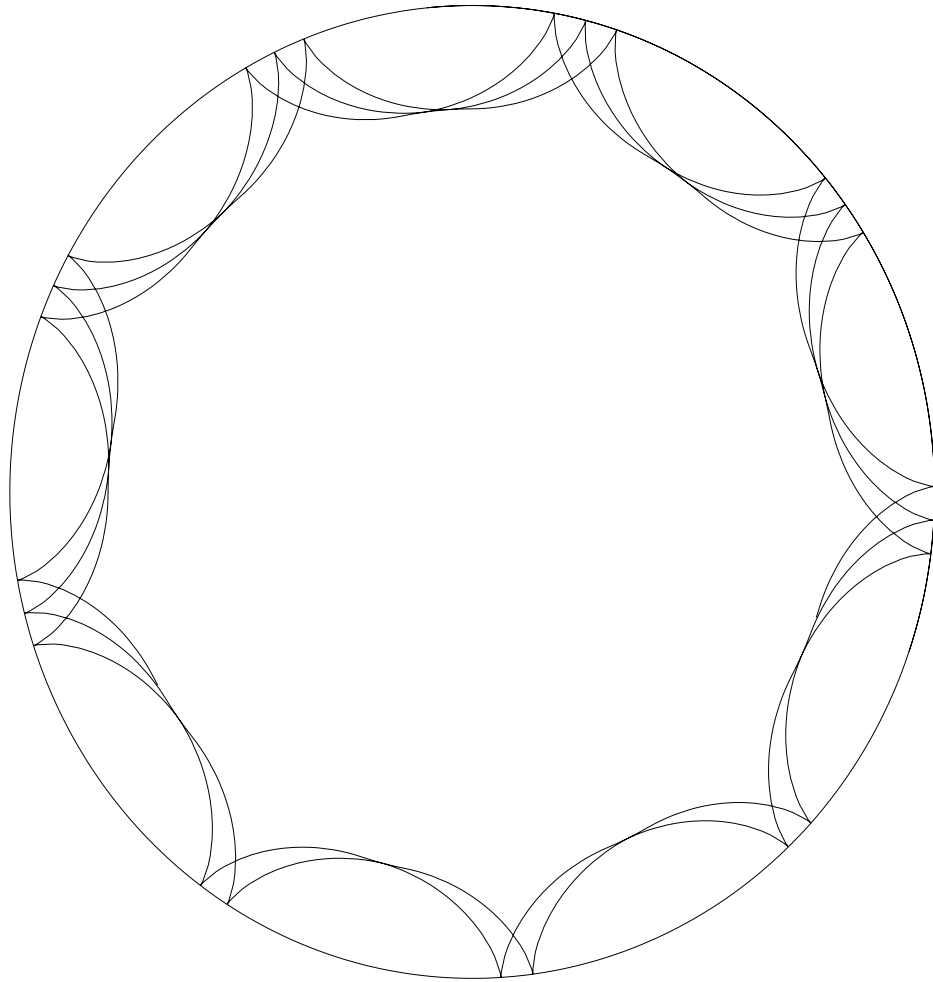


Figure 2.1: Acoustic raypaths in a two-dimensional Sun. The caustic at the lower turning point is clearly visible. Since the dispersion relation does not include an acoustic cutoff frequency, the upper caustic coincides with the surface. As will be seen later, inclusion of ω_c eliminates the cusps at the upper caustic, producing raypaths which are everywhere differentiable.

bordered by two caustic surfaces at which k_r changes sign. The quadratic dependence of the dispersion relation on the wavenumber implies that at any point within the cavity two rays, with k_r equal and opposite in magnitude, can exist. However, it will later prove useful to think of the rays as propagating in a slightly more complicated geometry in which two sheets are connected at the caustics, one in which k_r is restricted to positive values, the other in which k_r is negative. This domain is periodic in both the r and ϕ directions and is equivalent to the surface of a torus (unrelated, however, to the phase-space tori of §2.3). The construction of this new domain can be extended to higher-dimension systems, although visualization is more difficult.

We have not discussed how the values of ω and k_ϕ in Figure 2.1 were picked. In fact, they were chosen so that the ray corresponds to a p mode although, again, we have not yet indicated how this was done — indeed, the exact point of this work is to determine ω for arbitrary solar structures. Note, however, that even though it corresponds to an eigenmode, the ray does not close on itself. Instead it will eventually fill the entire cavity. Although the raypath itself gives no visual indication of whether it corresponds to an eigenmode, there is a technique similar to EBK quantization which allows one to make such determinations.

2.4.3 P Mode Quantization Conditions

We now consider how to determine the eigenvalues of equation (2.30) in the short-wavelength limit. The result will be almost identical to the EBK condition of equation (2.47), although the application to non-quantum systems was probably first discussed in Keller & Rubinow (1960). Our starting point is the wavefunction form of the solution as written in equation (2.32)

$$\Psi = A(\mathbf{x}, t)e^{i\Lambda\varphi(\mathbf{x}, t)}, \quad (2.50)$$

with φ real. As seen in the discussion of §2.4.2, the solution is a sum of multiple waves with opposing wavenumbers, however the forthcoming argument applies to each term individually and hence we work with a single term. Although this wavefunction is a classical solution, it is

analogous to a short-wavelength solution to the Schrödinger equation $\Psi = A \exp(ih^{-1}S)$ where S is the action and h^{-1} is equivalent to Λ . This is the basis for the strong similarity between the EBK result and the result of this section.

Since the domain is periodic, the wavefunction Ψ is constrained to be single-valued. No such restriction is placed on either the amplitude A or the phase φ . If we imagine traversing a closed circuit in the domain, the requirement that the solution be single-valued implies

$$\Lambda(\Delta\varphi) = 2\pi n + i(\Delta \ln A) \quad (2.51)$$

for any integer n , where Δ represents the difference accumulated along the circuit. However, we can quickly rewrite this condition by noting that

$$\Lambda(\Delta\varphi) = \Lambda \oint \nabla\varphi \cdot \mathbf{dx} \quad (2.52)$$

and thus, from equation (2.34),

$$\oint \mathbf{k} \cdot \mathbf{dx} = 2\pi n + i(\Delta \ln A). \quad (2.53)$$

Keller (1958), in the context of EBK quantization, first evaluated the final term of this equation, realizing that, as in optics, the phase of the amplitude is retarded by $\pi/2$ whenever a ray encounters a caustic. With this contribution, the condition becomes

$$\oint \mathbf{k} \cdot \mathbf{dx} = 2\pi(n + \frac{s}{4}), \quad (2.54)$$

where s is the number of caustics encountered along the path.

Although the quantization condition of equation (2.54) is valid around any closed curve in the domain, this does not lead to an infinite number of quantum conditions. Instead, there are as many independent curves, and hence quantization conditions, as there are degrees of freedom in the system.⁹ In the example considered in §2.4.2, evaluation of equation (2.54) along any two independent curves will yield two quantization conditions. Of course, some curves are more equal than others: wise choices in that case would be a curve at constant r and another

⁹ Topologically, two curves are independent when they cannot be continuously deformed into each other.

at constant ϕ . So, the complete quantization conditions are

$$\oint_{C_k} \mathbf{k} \cdot d\mathbf{x} = 2\pi\left(n_k + \frac{s_k}{4}\right) \quad (2.55)$$

where the C_k are independent curves and n_k and s_k are integers.

From our previous work relating \mathbf{k} and \mathbf{x} to the canonical momenta and positions, we can rewrite (2.55) in the suggestive form

$$I_k = \frac{1}{2\pi} \oint_{C_k} \mathbf{k} \cdot d\mathbf{x} = n_k + \frac{s_k}{4}, \quad (2.56)$$

which both connects the quantization condition to the realm of Hamiltonian mechanics discussed in §2.3 and shows that it is analogous to the EBK result of equation (2.47).

Unfortunately, while (2.56) appears to give a general method for determining eigenfrequencies, its use is limited to integrable systems. As Einstein (1917) recognized, in the context of EBK quantization, for non-integrable systems the curves C_k of equation (2.56) no longer exist and evaluation of the action variables becomes, in a strict mathematical sense, impossible. This restriction severely limits the convective structures which can be studied with this technique. Recall that Hamiltonian systems with two degrees of freedom, such as that of §2.4.2, require two constants of the motion to be integrable — in that case, ω and k_ϕ . Furthermore, each of these constants reflects a symmetry in the governing Hamiltonian, time-independence in the first case and azimuthal symmetry in the second. Although most convective flows can be assumed to be stationary on the timescale of p -mode oscillations, they do not have azimuthally-independent structures. Hence, k_ϕ is not a constant of the motion in such flows, the system is non-integrable, and equation (2.56) is an unsuitable method for determining the system's eigenfrequencies.

2.4.4 Surfaces of Section

As we will see, adiabatic switching addresses these difficulties. Before its introduction in §2.5, we briefly consider an aesthetically pleasing interpretation of the quantization conditions of the previous section. Although Noid & Marcus (1975) used this approach with some success to find the energy levels of an anharmonically coupled pair of oscillators, it does not extend to

non-integrable systems and is hence unsuitable for our needs. However, it gives the problem a geometric interpretation and, in addition, was the path we took on our first explorations of the subject. Although it can be applied to higher order systems, this method is most useful for a system with two degrees of freedom. We will avoid a formal treatment and instead concentrate on the system of §2.4.2; Tabor (1989) has a more general discussion.

Instead of treating equation (2.55) as an integral equation which must be solved to find the eigenfrequencies, we interpret it as a geometric statement. The Hamiltonian of §2.4.2 possesses two degrees of freedom and hence a ray propagates in a four-dimensional (r, ϕ, k_r, k_ϕ) phase space. However the constancy of ω and k_ϕ restrict the trajectory to a two-dimensional surface, topologically equivalent to a torus. Imagine the trajectory intersecting a plane at an arbitrary value of ϕ and making a record of the values of r and k_r at each intersection. After sufficient time, a surface of section will be traced: a closed curve which for our case can be found from solving the dispersion relation

$$k_r^2 = \frac{\omega^2}{c^2} - k_\phi^2. \quad (2.57)$$

A similar curve arises from considering the values of k_ϕ and ϕ at the intersection of the torus with a plane at constant r . Equation (2.55) is thus a statement concerning the area traced out by these curves: for eigenmodes the areas have certain quantized values. Rays not corresponding to modes trace out curves enclosing other areas not given by equation (2.55). Hence, one can determine the eigenmodes of a system by finding those rays which produce surfaces of section with the proper areas.

For integrable systems with two degrees of freedom, the trajectories are restricted to two-dimensional surfaces in phase space and hence the surfaces of section consist of smooth curves enclosing well defined areas. As a system is perturbed from integrability, the KAM theorem ensures that increasing numbers of invariant tori are destroyed. Rays whose initial conditions correspond to the destroyed tori are then free to wander in a three-dimensional region of phase space. A two-dimensional slice through a three-dimensional region of phase space does not

produce curves which enclose well-defined areas and hence makes the geometric interpretation of equation (2.55) unclear. The surfaces of section acquire a characteristic “fuzzy” appearance, an early example of which is seen in the work of Hénon & Heiles (1964). This is a consequence of the assertion made in §2.4 that the quantization conditions are undefined for non-integrable systems.

2.5 Adiabatic Switching

Ehrenfest (1917) was among the first to propose the concept of adiabatic switching, although his work has since been superseded by modern treatments. In essence, his hypothesis was that if a system is changed in a reversible, adiabatic way, then allowed motions will smoothly transform to allowed motions. Perhaps the most familiar example is provided by a small-amplitude pendulum. If the length of a pendulum is slowly increased, the energy, frequency, and oscillation amplitude will each decrease. However, the ratio of the energy to the frequency remains constant. In fact, this ratio remains constant for any perturbation, such as changing the gravitational acceleration or the mass of the bob, as long as it is performed on a timescale longer than the dynamical period of the system.

For a simple harmonic oscillator, of which the small-amplitude pendulum is an example, the ratio of the energy to the frequency is the classical action variable of §2.3. In a rough sense, an adiabatic change smoothly deforms the invariant tori between those of the initial and those of the final state. This property is of particular interest if a system has eigenmodes, for in this case the action variables — at least in the semi-classical limit — are quantized. If we start the system in an eigenmode for which the eigenfrequencies are known and allow it to evolve as the strength of a perturbation is increased, eventually we are left with a new system for which the eigenfrequencies were not known beforehand. But, due to the adiabatic nature of the transition, the action variables remain quantized and hence the original eigenmode has slowly relaxed into an eigenmode of the new system. Although we lend a degree of formalism to this qualitative description below, we do not present a complete derivation. A more thorough review of the

modern implementation of the method of adiabatic switching and its applications can be found in Skodje & Cary (1988).

Implementing adiabatic switching is fairly straightforward. The non-integrable Hamiltonian for which the eigenfrequencies are desired is written in action-angle variables as a sum of two terms

$$H(\mathbf{I}, \Theta) = H_0(\mathbf{I}) + H_1(\mathbf{I}, \Theta), \quad (2.58)$$

where H_0 is an integrable Hamiltonian for which the eigenfrequencies are known (for instance, from the quantization procedure of §2.4), and H_1 includes the non-integrable terms. We introduce into equation (2.58) a time-dependent switching function $\lambda(t)$:

$$H = H_0 + \lambda(t)H_1 \quad (2.59)$$

which satisfies

$$\lambda(t \leq 0) = 0 \quad \text{and} \quad \lambda(t \geq T) = 1 \quad (2.60)$$

for some time T which, in order to ensure that the transition from H_0 to H is adiabatic, is taken to be much longer than other timescales associated with the system (for instance, the characteristic propagation times of equation (2.42), $\nu_k^{-1} = [\partial H_0 / \partial I_k]^{-1}$). In addition the first few derivatives with respect to t of λ are, to ensure the smoothness of the transition, chosen to be continuous at $t = 0$ and $t = T$. In this work, λ is taken to be

$$\lambda(0 \leq t \leq T) = \frac{t}{T} - \frac{1}{2\pi} \sin\left(\frac{2\pi t}{T}\right). \quad (2.61)$$

Johnson (1985) discusses the effects of different switching functions.

At $t = 0$ we begin with an eigenmode. That is, our initial conditions are such that we satisfy the quantization conditions for the Hamiltonian H_0 . We then numerically integrate Hamilton's equations of motion (2.38) under the influence of the Hamiltonian H given in equation (2.59). As t increases so does $\lambda(t)$, adiabatically switching on the influence of the non-integrable term H_1 , and allowing the eigenfrequency of the system to slowly adjust from its original value. At $t = T$ we arrive at the eigenfrequency of the non-integrable Hamiltonian H .

Unfortunately, the mathematical justification of adiabatic switching is complete only for systems with one degree of freedom. For these systems, which include the pendulum discussed above, it can be proven (for example Arnold 1978, Section 52F) that the action variable is a strict adiabatic invariant if the characteristic frequency is never equal to 0. Qualitatively, this is a reasonable statement. Since the switching is slow, at any instant the system is governed by a one-dimensional, time-independent Hamiltonian. Such systems are always integrable since they possess one constant of the motion, the Hamiltonian itself, and hence the phase-space trajectories are restricted to a one-dimensional closed curve (that is, a one-dimensional invariant torus). Because of this confinement, a trajectory samples all of the available phase space during one period of motion and the system can, in a sense, average over the entire disturbance and keep the action variable constant. The restriction to $\nu_k \neq 0$ is reasonable when one realizes that if $\nu_k = 0$ at any point, the period of the system is infinite. It is then impossible for the switching to occur on a timescale which is long compared to the system's motion and a complete exploration of phase space cannot be made.

For systems with $n > 1$ degrees of freedom, the situation is less certain. A primary concern is the existence of the invariant tori, as time-independent Hamiltonians are always integrable only when $n = 1$. As we briefly discussed in §2.3, the KAM theorem concerns the existence of these tori. A more formal, although still not rigorous, statement of the theorem is:¹⁰ If an unperturbed, integrable system is non-degenerate, then for sufficiently small perturbations, most non-resonant invariant tori do not vanish. These invariant tori form a majority when the perturbation is small.

The degeneracy condition is a generalization of the requirement we encountered in the one degree of freedom case that $\nu_k \neq 0$. It accounts for the possibility that if the characteristic frequencies are commensurable, a trajectory will not fully explore an invariant torus and hence

¹⁰ A precise statement may be found in Arnold (1978), Appendix 8B.

will not sample the available phase space. As usually stated, it is written as

$$\det \left| \frac{\partial^2 \nu_i(\mathbf{I})}{\partial I_j} \right| = \det \left| \frac{\partial^2 H_0(\mathbf{I})}{\partial I_i \partial I_j} \right| \neq 0. \quad (2.62)$$

This condition is sufficient but not necessary, and the unperturbed system which we consider in Chapter 3 violates it. For a system with two degrees of freedom, another less stringent requirement (see Lichtenberg & Lieberman 1983, equation (3.2.12)) states that if the ratio of the characteristic frequencies is $\nu_2/\nu_1 = r/s$ with r and s integers, then

$$r^2 \frac{\partial^2 H_0}{\partial I_1^2} - 2rs \frac{\partial^2 H_0}{\partial I_1 \partial I_2} + s^2 \frac{\partial^2 H_0}{\partial I_2^2} \neq 0 \quad (2.63)$$

is sufficient to ensure the existence of invariant tori under small perturbations. Our unperturbed state does satisfy this condition.

Although the KAM theorem assures us of the existence of invariant tori (at least for small perturbations), during the switching we are essentially guaranteed to encounter regions where the degeneracy condition is violated and hence no tori exist. For a system with two degrees of freedom, the two-dimensional tori partition the three-dimensional energy shell into an inside and an outside, effectively blocking the trajectories on destroyed tori from wandering through all of phase space. However, if our original time-independent system has two degrees of freedom, the time-dependent switching Hamiltonian of (2.59) is equivalent to a time-independent system with three degrees of freedom. The complete phase space is six-dimensional with the time-independent Hamiltonian confining the system to a five-dimensional energy shell. The invariant tori are three-dimensional and do not partition the five-dimensional space. Therefore, when we switch through a region violating the degeneracy condition, the trajectory is free to wander in phase space away from our original family of invariant tori. This process is known as Arnold diffusion and is ubiquitous in non-integrable systems with more than two degrees of freedom. Arnold diffusion is of particular importance because it places an effective limit on the size of T in equation (2.61). As $T \rightarrow \infty$ a switched system remains near destroyed tori for longer periods of time, undergoes more Arnold diffusion, and eventually wanders randomly in phase space. We discuss our choice for T in §3.2.

There is the final possibility that the end state to which we switch does not contain any invariant tori. The KAM theorem merely asserts that most invariant tori exist for small perturbations; as the perturbation strength grows, more and more tori are destroyed until eventually none remain. This difficulty explains why we were forced to abandon the quantization procedure of §2.4 and adiabatic switching cannot be completely justified when this occurs.

Although the formal justification for adiabatic switching is incomplete for the systems under consideration, the empirical evidence for its success is strong. It has been used to investigate molecular spectra (Patterson 1985; Smith et al. 1987), the energy of nucleon systems (Brut & Arvieu 1993), and optical cavities (Nöckel & Stone 1997), and in each case performed well despite violating the strict constraints on its use. One justification is the possibility that switched systems spend a sufficiently small amount of their time in regions where the procedure is formally invalid that the final results are only slightly perturbed. Still, the strongest support comes from its long-standing success, and it is in that spirit that we use it to explore the effects of convective motions on solar eigenfrequencies.

Chapter 3

Implementation and Tests

Having established the underlying theory, we now turn to a more detailed description of its application to the determination of convective effects on p -mode eigenfrequencies. In §3.1 we examine our reference state in some detail. Section 3.2 documents the equations necessary to implement adiabatic switching as well as the computer program we have written to solve them. Two tests of the method and our code are discussed in §3.3 and §3.4.

3.1 The Reference State

We are interested in finding the eigenfrequencies of non-integrable systems which can be written in the form of equation (2.45). Our reference state, corresponding to H_0 in equation (2.45) and which we will show below to be integrable and non-degenerate, is a two-dimensional, adiabatically stratified, plane-parallel polytrope. The horizontal and vertical unit vectors are $\hat{\mathbf{x}}$ and $\hat{\mathbf{z}}$, respectively. We also define $z = 0$ as the level where $p = \rho = 0$ and take the vertical axis to increase inwards, opposite the radial axis in a spherical polar coordinate system. Polytropic systems are those where the pressure p and density ρ are assumed to be related by

$$\frac{p}{p_0} = \left(\frac{\rho}{\rho_0} \right)^{1 + \frac{1}{\mu}}, \quad (3.1)$$

where p_0 and ρ_0 are constants and μ is the polytropic index, which for an adiabatically stratified system may be written in terms of the adiabatic exponent defined in equation (2.5) as $\mu = 1 + 1/\Gamma_1$. For models in radiative equilibrium $\mu = 3$, although observations suggest $\mu = 3.5$

is a better fit for the solar photosphere. We adopt the former value in this work. Enforcing hydrostatic equilibrium leads to the relations

$$\frac{p}{p_0} = \left(\frac{z}{z_0}\right)^{\mu+1} \quad \text{and} \quad \frac{\rho}{\rho_0} = \left(\frac{z}{z_0}\right)^{\mu}, \quad (3.2)$$

where z_0 is a constant. Finally, the adiabatic sound speed and cutoff frequency can be computed from equations (2.4) and (2.28) respectively, and are given by

$$c^2 = \frac{gz}{\mu} \quad \text{and} \quad \omega_c^2 = \frac{\mu(\mu+2)}{4z^2}c^2, \quad (3.3)$$

where g is the gravitational acceleration. Assuming the ideal gas law holds, equations (3.2) and (3.3) imply that the square of the sound speed is proportional to the temperature.

For this system (compare with equation (2.35)), the Hamiltonian is

$$\omega(x, z, k_x, k_z) = \sqrt{\frac{gz}{\mu}(k_x^2 + k_z^2) + \frac{g(\mu+2)}{4z}}, \quad (3.4)$$

where k_x and k_z are the wavenumbers in the horizontal and vertical directions. As this two degree of freedom Hamiltonian is independent of time as well as the coordinate x , there are two constants of the motion: ω and k_x . These constraints are enough to ensure that this Hamiltonian is integrable. A raypath for this system is shown in Figure 3.1. Although this geometry is plane-parallel rather than spherically symmetric, the raypaths are obviously quite similar to those of Figure 2.1. In this figure the upper turning point at $z \approx 0.3$, an effect produced by the acoustic cutoff frequency, is clearly visible.

We turn next to the formulation of the reference system in action-angle coordinates. Combining the expressions for c^2 and ω_c^2 from equation (3.3) with the dispersion relation of equation (3.4), we may solve for k_z :

$$k_z^2 = \frac{\omega^2 - \omega_c^2}{c^2} - k_x^2 = \frac{\mu\omega^2}{gz} - \frac{\mu^2}{4z^2} \left(1 + \frac{2}{\mu}\right) - k_x^2. \quad (3.5)$$

In the extended periodic domain described in §2.4.2 we can integrate along a curve at constant x and write equation (2.43) as

$$I_z = \frac{1}{2\pi} \oint k_z dz = \frac{1}{\pi} \int_{z_1}^{z_2} k_z dz, \quad (3.6)$$

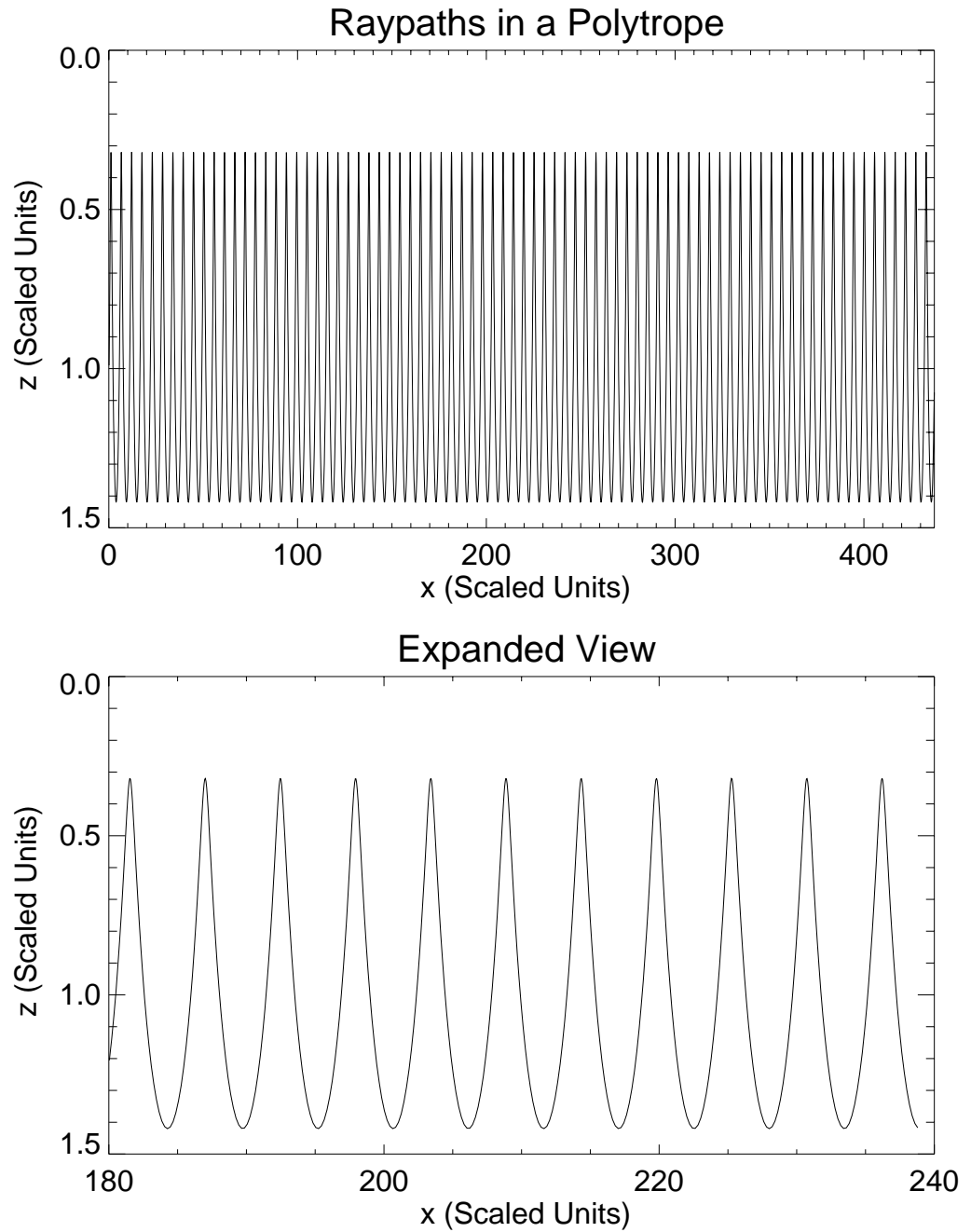


Figure 3.1: A sample raypath in an adiabatically stratified, two-dimensional, polytropic envelope with $\mu = 3$. This ray corresponds to a mode with $n = 1$, $\ell = 200$. The top panel shows the entire horizontally periodic cavity with length $2\pi R_{\odot}$. The large value of ℓ produces the many oscillations in the horizontal direction. The bottom panel shows an expanded version of the top panel. Note the two caustic surfaces at the vertical extremes of the cavity.

where z_1 and z_2 are the upper and lower turning points of the ray. With k_z given by equation (3.5), and since k_x is a constant of the motion, the integral in equation (3.6) can be analytically computed. The result is

$$I_z = \frac{1}{2} \left(\frac{\mu\omega^2}{gk_x} - \mu\sqrt{1 + \frac{2}{\mu}} \right). \quad (3.7)$$

A similar integral for the horizontal action variable gives

$$I_x = k_x R_\odot, \quad (3.8)$$

and thus the reference Hamiltonian in action-angle coordinates is

$$H = \omega = \sqrt{\frac{2g}{\mu R_\odot} I_x \left[I_z + \frac{\mu}{2} \left(1 + \frac{2}{\mu} \right)^{\frac{1}{2}} \right]}. \quad (3.9)$$

The characteristic frequencies, derived from equation (2.42), are

$$\nu_x = \frac{\partial\omega}{\partial I_x} = \frac{\omega}{2I_x} \quad \text{and} \quad \nu_z = \frac{\partial\omega}{\partial I_z} = \frac{\omega}{2 \left[I_z + \frac{\mu}{2} \left(1 + \frac{2}{\mu} \right)^{\frac{1}{2}} \right]}. \quad (3.10)$$

Although this Hamiltonian violates the stringent degeneracy criterion of equation (2.62), it satisfies the looser standard of equation (2.63). Hence the KAM theorem applies to this reference Hamiltonian.

3.1.1 Reference State Results

Several properties of this polytropic reference state will be of use in later sections. Perhaps most importantly Christensen-Dalsgaard (1980), beginning with the perturbed structure equations (2.7)–(2.10), solved for the eigenfrequencies of the system. Their exact values are

$$\omega^2 = \frac{2gk_x}{\mu} \left(n + \frac{\mu}{2} \right) \quad \text{for} \quad n = 1, 2, \dots \quad (3.11)$$

where $k_x = \ell/R_\odot$ and ℓ is an integer which we associate with the spherical harmonic degree.¹

The upper and lower turning points of a ray occur when $k_z = 0$. Using equation (3.4) and the condition given by equation (3.11), the cavity for an eigenmode is bounded in the vertical

¹ In the spherically symmetric case, $k_x = \sqrt{\ell(\ell+1)}/R_\odot$.

direction by

$$z_{1,2} = \left(n + \frac{\mu}{2}\right) \frac{R_\odot}{\ell} \left[1 \mp \sqrt{1 - \frac{\mu(\mu+2)}{(\mu+2n)^2}}\right]. \quad (3.12)$$

The midpoint of a modal cavity is merely

$$z_{\text{mid}} = \left(n + \frac{\mu}{2}\right) \frac{R_\odot}{\ell}, \quad (3.13)$$

which demonstrates, as noted earlier, that the depth of the cavity scales roughly as n/ℓ .

The evolution of a ray is given by Hamilton's equations, the general form of which are given in equation (2.38). Specializing to a polytrope, we have

$$\frac{dx}{dt} = \frac{c^2 k_x}{\omega} \quad (3.14)$$

$$\frac{dz}{dt} = \frac{c^2 k_z}{\omega} \quad (3.15)$$

$$\frac{dk_x}{dt} = 0 \quad (3.16)$$

$$\frac{dk_z}{dt} = -\frac{\omega}{2z}, \quad (3.17)$$

which explicitly contains the invariability of k_x .

We can also determine the characteristic periods of motion in each coordinate from equations (3.10) and (3.11). Doing so, we have

$$T_z = \frac{2\pi}{\nu_z} = \frac{4\pi}{\omega} \left(n + \frac{\mu}{2}\right) \quad (3.18)$$

and

$$T_x = \frac{2\pi}{\nu_x} = \frac{4\pi}{\omega} \ell. \quad (3.19)$$

Finally, we arrive at the ratio of the horizontal and vertical periods:

$$\frac{T_x}{T_z} = \frac{\ell}{n + \frac{\mu}{2}}. \quad (3.20)$$

For the high-degree modes under consideration the horizontal period is substantially longer than the vertical. In Figure 3.1, the ratio is 80 : 1.

3.1.2 Quantization Conditions

Since the reference state is integrable we can apply to it the quantization procedure of §2.4. As expected, in the appropriate limit it reproduces equation (3.11). Starting with equation (3.6), and noting that the integration path touches two caustics, equation (2.47) becomes

$$I_z = \frac{1}{2\pi} \oint k_z dz = \frac{1}{\pi} \int_{z_1}^{z_2} k_z dz = \left(n - \frac{1}{2} \right) \quad \text{for } n = 1, 2, \dots \quad (3.21)$$

with a final result of

$$\omega^2 = \frac{2gk_x}{\mu} \left[n - \frac{1}{2} + \frac{\mu}{2} \left(1 + \frac{2}{\mu} \right)^{\frac{1}{2}} \right] \quad \text{for } n = 1, 2, \dots \quad (3.22)$$

If we also evaluate equation (2.47) on a curve of constant z we encounter no caustics and find that

$$I_x = \frac{1}{2\pi} \oint k_x dx = \frac{1}{2\pi} \int_0^{2\pi R_\odot} k_x dx = \ell \quad \text{for } \ell = 0, 1, \dots \quad (3.23)$$

for which

$$k_x = \frac{\ell}{R_\odot} \quad \text{for } \ell = 0, 1, \dots \quad (3.24)$$

Although equation (3.24) is the correct horizontal quantization condition, the eigenfrequencies of equation (3.22) are not the same as those of equation (3.11). Recall, however, that the derivation of the quantization conditions relies on formulating the solutions as local plane waves, an approximation which is only valid when the wavelength of the variations in the reference state is larger than the wavelength of the solution. The limit in which we expect the two results to agree, then, is that where the eigenfunction rapidly oscillates in the vertical direction; in other words, when $n \gg 1$. In this limit the results agree. It should be noted that even with $n = 1$ and $\mu = 3$ the relative error in the eigenfrequencies is $\approx 3\%$, with agreement improving as either μ or n increases.

In this case we were able to evaluate the action variables due to the simple form of the sound speed and acoustic cutoff frequency given in equation (3.3). However, even when the action variables cannot be derived analytically, the quantization procedure will still work,

provided the system is integrable. For solar p modes the most realistic condition guaranteeing integrability is for the sound speed and cutoff frequency to be independent of x , implying that k_x is a constant of the motion. The quantized action variables can then be evaluated numerically to determine the eigenfrequency ω .

3.2 Adiabatic Switching

Our work in Chapter 2 demonstrated that the dispersion relation of equation (3.4) governs ray motion. However, this derivation was rather restrictive in that it ignored interesting effects such as advective motions, magnetic fields, and rotation, all of which contribute terms to the dispersion relation and can affect ray trajectories. Of the three, only advective motions are necessary for describing convective structures, and so in this initial examination we ignore magnetism and rotation. In a frame of reference moving with the ray, advective motions will contribute a Doppler shift to the ray frequency implying that the correct dispersion relation is:

$$(\omega - \mathbf{k} \cdot \mathbf{v})^2 = k^2 c^2 + \omega_c^2 \quad (3.25)$$

where \mathbf{v} is the velocity field. We adopt equation (3.25) as the dispersion relation for a ray propagating in a convective atmosphere in the remainder of this work. Note that for the polytropic reference state of §3.1 equation (3.25) reduces to equation (3.4) if $\mathbf{v} = 0$.

After some algebraic manipulation we can write this Hamiltonian in the form of equation (2.59):

$$\omega = c_0 \left(k^2 + \frac{\mu(\mu + 2)}{4z^2} \right)^{\frac{1}{2}} + \lambda(t) \left[(c - c_0) \left(k^2 + \frac{\mu(\mu + 2)}{4z^2} \right)^{\frac{1}{2}} + \mathbf{k} \cdot \mathbf{v} \right], \quad (3.26)$$

where $c_0 = \sqrt{gz/\mu}$ is the polytropic sound speed, c and \mathbf{v} are the sound speed and velocity field of the convective model, and the cutoff frequency of equation (3.3) replaces ω_c . The true definition of the cutoff frequency, given in equation (2.28), depends on the density scale height H_ρ which, in a self-consistent model, will almost certainly undergo perturbations somewhat different from those affecting the sound speed. However, this is a minor effect and we assume in

this work that the only perturbations to the cutoff frequency arise from variations in the sound speed in the manner shown.

For this more complicated dispersion relation, Hamilton's equations are

$$\frac{dx}{dt} = \frac{c_0^2 k_x}{\Omega} + \lambda(t) \left[\frac{c_0^2 k_x}{\Omega} \left(\frac{c}{c_0} - 1 \right) + v_x \right] \quad (3.27)$$

$$\frac{dz}{dt} = \frac{c_0^2 k_z}{\Omega} + \lambda(t) \left[\frac{c_0^2 k_z}{\Omega} \left(\frac{c}{c_0} - 1 \right) + v_z \right] \quad (3.28)$$

$$\frac{dk_x}{dt} = -\lambda(t) \left[\frac{\Omega}{c_0} \frac{\partial c}{\partial x} + k_x \frac{\partial v_x}{\partial x} + k_z \frac{\partial v_z}{\partial x} \right] \quad (3.29)$$

$$\frac{dk_z}{dt} = -\frac{\Omega}{2z} - \lambda(t) \left[\Omega \left(\frac{1}{c_0} \frac{\partial c}{\partial z} - \frac{1}{2z} \right) + k_x \frac{\partial v_x}{\partial z} + k_z \frac{\partial v_z}{\partial z} \right], \quad (3.30)$$

where $\Omega = \sqrt{c_0^2(k_x^2 + k_z^2) + \omega_c^2}$ is the instantaneous polytropic frequency. Note that in the polytropic limit where $c = c_0$ and $\mathbf{v} = 0$, we return to equations (3.14)–(3.17).

Although we include the function $\lambda(t)$ in our equations, we have not yet addressed our choice for the switching time T of equation (2.61). In order to ensure adiabaticity, we must choose T to be much longer than the longest dynamical timescale associated with the system. Heuristically, this ensures that the ray has a chance to explore the available phase space during the switching process. The relevant timescales in this case are the time for the ray to undergo an oscillation in the vertical and horizontal directions — taking our cue from equation (3.20), we choose $T \gg T_x$. As we discussed in §2.5, the presence of Arnold diffusion in non-integrable systems sets an upper constraint on the choice of T . Our numerical experiments show that choosing $T \approx 40T_x$ offers a satisfactory compromise between the two constraints. This choice agrees with that made in other implementations of adiabatic switching.

Beginning from different initial conditions should, in principle, lead to identical eigenfrequencies for the final state. For sufficiently complex systems our numerical experiments find a scatter in the results, presumably arising from the combined effects of a finite switching time and Arnold diffusion. This scatter is observed by other investigators and it has been found empirically that better results are obtained by implementing the procedure for several randomly distributed initial conditions and averaging the final eigenvalues (although see the mathematical justification presented in Skodje & Cary (1988)). This averaging is particularly necessary for the

systems of §4.3 and §4.4 where we typically find the eigenfrequencies for 20 initial conditions, a choice which we find suitably constrains the result.

With these considerations, we have written a computer program to implement adiabatic switching by numerically integrating equations (3.27)–(3.30). As our reference state we choose an adiabatically stratified, plane-parallel polytrope with an index μ corresponding to the average stratification of the photospheric model. We approximate the photospheric model itself as a grid of sound speeds c and velocity vectors $\mathbf{v} = (v_x, v_z)$. Although our current code requires equally spaced grids, they are not a necessity. Indeed, since the upper portion of the solar convection zone contains many scale heights of material an adaptive grid spacing would be computationally beneficial. The spacing of our grid elements represents, as usual, a trade-off between accuracy and computational speed. Currently we only work with two-dimensional, plane-parallel convective models with thermal and velocity structures, though there is no fundamental barrier to extending the method to explore other structures including, for example, those with magnetic fields or three dimensions.

To integrate equations (3.27)–(3.30), the code uses a slightly modified version of the DE package of Shampine & Gordon (1975): a variable-order, variable-timestep Adams-Bashforth-Moulton PECE (predict-evaluate-correct-evaluate) method. The modifications include an updating of the code to FORTRAN 90 and an adaptation for horizontally periodic boundary conditions. Fourth-order central differences are used to evaluate the partial derivatives of the sound speed and velocity fields everywhere within the cavity, except near the top and bottom boundaries where fourth-order forward and backward differences are used. The DE package allows the user to specify tolerances for both the relative and absolute errors. We found that the integration was sufficiently quick and accurate if both were set to 10^{-9} . Integration times for a trajectory greatly vary depending on the parameter range and the convective model. For a $n = 1$, $\ell = 200$ mode propagating in the perturbation of §3.3, integration of one trajectory takes ≈ 5 minutes to complete on a 194 MHz SGI Power Onyx. A further description of the code’s history and structure is presented in Appendix D.

Finally, we have scaled our variables in order to simplify the calculations. Unless otherwise noted, all lengths are quoted in units of 10^9 centimeters and all times in units of $10^{2.5}$ seconds. So, the solar surface gravity is $g = 2.7397$, the Sun's radius is $R_\odot = 69.599$ and a canonical 5-minute oscillation has a frequency of $\omega/(2\pi) = 1.0541$.

3.3 A Test of an Integrable System

To test the methodology and our code, we examine an integrable system whose eigenfrequencies can be computed both with adiabatic switching and through EBK quantization. Consider the simple, but not particularly realistic, case of a photosphere with no fluid motions and a sound speed closely related to the polytropic value of equation (3.3):

$$c = \left(\frac{gz}{\mu}\right)^{\frac{1}{2}} [1 + \epsilon \sin(Kz)], \quad (3.31)$$

where ϵ is the amplitude and K the wavenumber of the perturbation. Horizontal invariance implies that k_x is a constant of the motion and hence that the system is integrable at every point during the switching. For this perturbation, the acoustic cutoff frequency of equation (3.3) becomes

$$\omega_c = \left(\frac{g(\mu + 2)}{4z}\right)^{\frac{1}{2}} [1 + \epsilon \sin(Kz)]. \quad (3.32)$$

As mentioned above, the true expression for ω_c , equation (2.28), directly depends on the density scale height H_ρ as well as the sound speed. Equation (3.32) is not fully self-consistent, but we ignore the resulting discrepancies.

In order to derive the eigenfrequencies from EBK quantization, we must solve the integral equation

$$\int_{z_1}^{z_2} k_z dz = \int_{z_1}^{z_2} \left[\frac{\mu\omega^2}{gz[1 + \epsilon \sin(Kz)]^2} - \frac{\mu^2}{4z^2} \left(1 + \frac{2}{\mu}\right) - k_x^2 \right]^{\frac{1}{2}} dz, = \frac{\pi}{2} \quad (3.33)$$

for the eigenfrequency ω where z_1 and z_2 are the depths at which the integrand vanishes. This equation is only valid for the lowest ($n = 1$) mode; for higher modes the right-hand side increases by the necessary factors of π . Perhaps the most straightforward method of evaluating

this equation, and the one we use to derive the results presented below, is a bisection-like trial-and-error method.

We compute relative frequency shifts $\Delta\omega/\omega$ arising from the sound speed perturbation of equation (3.31) via adiabatic switching and EBK quantization and list the results in Table 3.1. The unperturbed frequencies, which we list for three of the modes in the first rows, are not identical for the two methods. For adiabatic switching we use the true eigenfrequencies of equation (3.11) while for EBK quantization we use the results of equation (3.22). The fractional frequency shifts do agree, however. The results suggest three separate trends in the frequency shifts:

- (a) The fractional frequency shift increases as n increases.
- (b) The fractional frequency shift decreases as ℓ increases.
- (c) The fractional frequency shift increases as ϵ increases.

In order to explain these results we turn to an analysis based on the work of Gough (1993), wherein we expand the EBK quantization condition of equation (3.6) around the polytropic reference state.

From equation (3.31),

$$c = c_0 + \Delta c = \left(\frac{gz}{\mu}\right)^{\frac{1}{2}} + \epsilon \left(\frac{gz}{\mu}\right)^{\frac{1}{2}} \sin(Kz) \quad (3.34)$$

where c_0 is the polytropic sound speed. Making similar expansions to ω and ω_c , the EBK quantization condition for the perturbed state is

$$\int_{z_1}^{z_2} k_z dz = \int_{z_1}^{z_2} \left[\frac{(\omega_0 + \Delta\omega)^2 - (\omega_{c,0} + \Delta\omega_c)^2}{(c_0 + \Delta c)^2} - k_x^2 \right]^{\frac{1}{2}} dz = \frac{\pi}{2}, \quad (3.35)$$

where quantities with a 0 subscript correspond to the polytropic reference state. Next, assuming that $\Delta\omega$, Δc , and $\Delta\omega_c$ are small parameters, we expand and discard higher-order terms. After rearranging, we have

$$\int_{z_1}^{z_2} k_{z,0} \left[1 + \frac{2}{c_0^2 k_{z,0}^2} \left(\omega_0 \Delta\omega - \omega_0^2 \frac{\Delta c}{c_0} + \omega_c^2 \frac{\Delta c}{c_0} - \omega_c \Delta\omega_c \right) \right]^{\frac{1}{2}} dz = \frac{\pi}{2}, \quad (3.36)$$

Table 3.1: Frequency shifts for a vertical sound speed perturbation. Some entries have been repeated in order to display trends.

n^a	ℓ^b	ϵ^c	K^c	$[\Delta\omega/\omega]_{AS}^d$	$[\Delta\omega/\omega]_{EBK}^e$
1 ^f	200			3.622	3.576
2	200			4.286	4.247
1	400			5.123	5.057
1	200	0.04	0.05	1.7×10^{-3}	1.7×10^{-3}
2	200	0.04	0.05	2.4×10^{-3}	2.4×10^{-3}
3	200	0.04	0.05	3.1×10^{-3}	3.0×10^{-3}
4	200	0.04	0.05	3.8×10^{-3}	3.7×10^{-3}
1	100	0.04	0.05	3.4×10^{-3}	3.4×10^{-3}
1	200	0.04	0.05	1.7×10^{-3}	1.7×10^{-3}
1	400	0.04	0.05	8.7×10^{-4}	8.7×10^{-4}
1	800	0.04	0.05	4.4×10^{-4}	4.4×10^{-4}
1	200	0.01	0.05	4.1×10^{-4}	4.2×10^{-4}
1	200	0.02	0.05	8.4×10^{-4}	8.5×10^{-4}
1	200	0.04	0.05	1.7×10^{-3}	1.7×10^{-3}
1	200	0.08	0.05	3.4×10^{-3}	3.4×10^{-3}
1	200	0.16	0.05	6.8×10^{-3}	6.8×10^{-3}

^a Vertical mode number.

^b Horizontal mode number.

^c Perturbation parameter from equation (3.31).

^d Relative frequency shifts from adiabatic switching.

^e Relative frequency shifts from EBK quantization.

^f The first three rows give unperturbed frequencies for comparison purposes.

where $k_{z,0}$ is the positive root of equation (3.5) and is thus a function of only unperturbed quantities. We expand again, ignore any perturbations to the cavity boundary (which we will see below are small), and cancel the zeroth-order term leaving, after some algebraic simplifications,

$$\frac{\Delta\omega}{\omega_0} = \left[\int_{z_1}^{z_2} \frac{\Delta c}{c_0} \frac{dz}{k_{z,0}c_0^2} \right] \left[\int_{z_1}^{z_2} \frac{dz}{k_{z,0}c_0^2} \right]^{-1}. \quad (3.37)$$

Note that we can derive the same result by expanding the horizontal quantization condition as well. In this case $\oint k_z dz$ is simpler to evaluate than $\oint k_x dx$ since the former includes the constant k_x^2 within the integrand while the latter would include terms proportional to Δk_z .

Thus, the fractional frequency shift is the weighted average of the fractional sound speed perturbation over the cavity. A mathematically satisfactory explanation for the trends noted above could come from integrating equation (3.37) analytically for the perturbation given in equation (3.34). However that approach is only possible for simple perturbations and so, in preparation for the results of Chapter 4, we cast our arguments in a more physically motivated form.

First, $\Delta c/c_0 = \epsilon \sin(Kz) \approx \epsilon Kz$ when, as is the case for the parameters we consider, Kz is small. Since the perturbation is positive and depends linearly on ϵ , it is not surprising that the fractional frequency shifts seen in Table 3.1 are always positive and scale linearly with the perturbation strength. The other two effects are somewhat more subtle as they arise from changes in the depth of the acoustic cavity. From equation (3.13), we see that the location of a cavity varies inversely with ℓ and linearly with $n + \mu/2$. As n and ℓ change, a ray encounters perturbations of different strengths which impart different frequency shifts. In this case the perturbation strength depends linearly on depth and we expect the fractional frequency shift to decrease inversely with ℓ and increase as $n + \mu/2$. These trends are reproduced by adiabatic switching.

We conclude that for vertically dependent sound speed perturbations, the fractional frequency shift depends linearly on the strength of the perturbation. The variation with the mode parameters depends on the functional form of the perturbation. For $\Delta c/c_0 \propto z^p$, we expect the

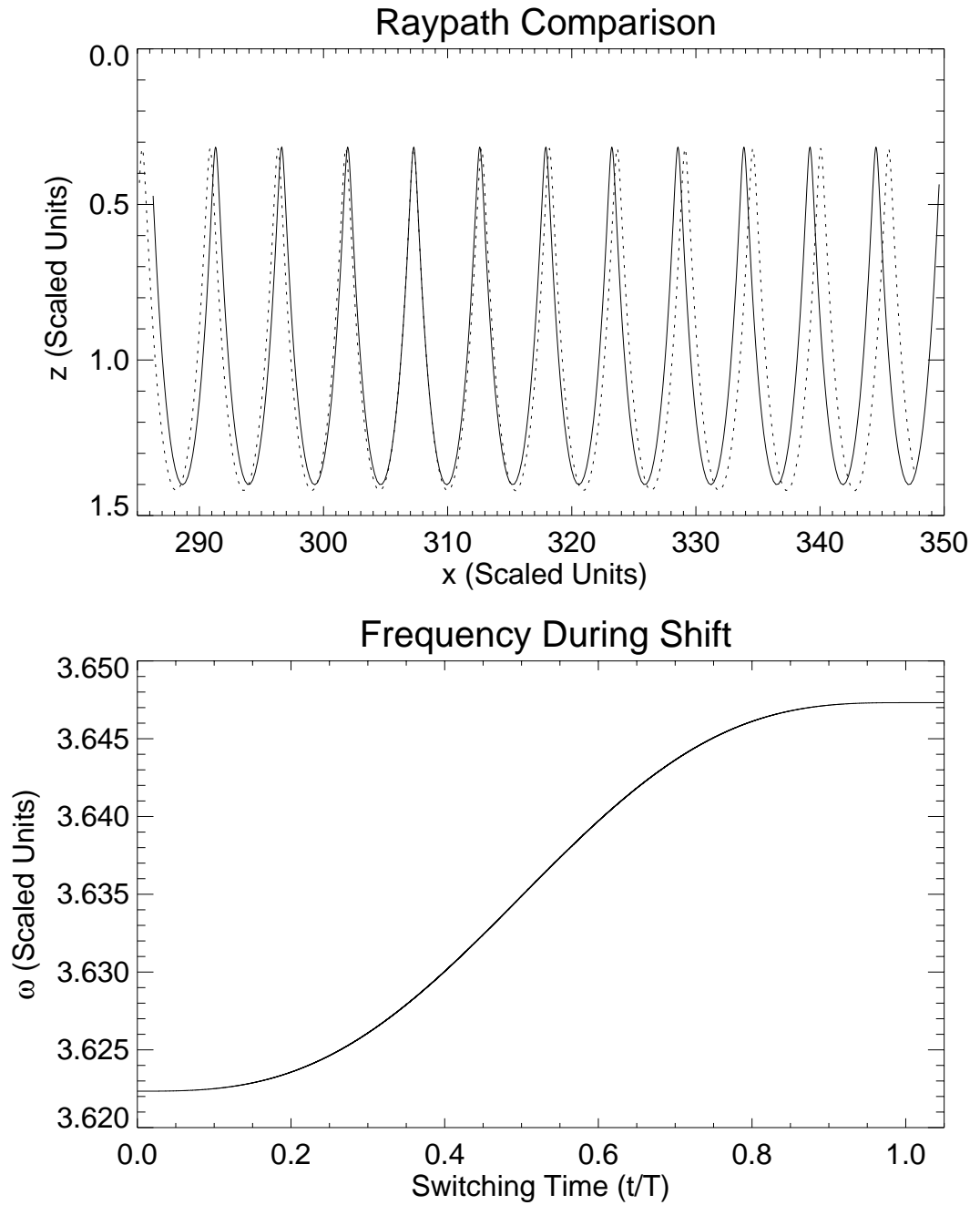


Figure 3.2: A raypath and the evolution of the eigenfrequency for the perturbation of §3.3. Results for a $n = 1$, $\ell = 200$ mode and the sound-speed perturbation of equation (3.31) with $\epsilon = 0.16$, $K = 0.05$ are plotted. See the text for further discussion.

fractional frequency shifts to vary as $(n + \mu/2)^p$ and ℓ^{-p} .

Finally, we present the perturbed raypaths and the modification of the frequency during adiabatic switching in Figure 3.2. The top panel shows two raypaths in a portion of the acoustic cavity. The dotted line is a raypath in the polytropic reference state while the solid line is a raypath in the perturbed model whose structure is given by equation (3.31). The cavity in the perturbed model is shifted slightly toward the surface due to the increased sound speed. The second panel shows the evolution of the ray frequency as a function of switching time. The smooth transition occurs when switching between integrable systems and, as we will see, does not occur for more complicated perturbations.

3.4 Doppler Shifts

As a final test before turning to non-integrable systems, we consider the effect of a constant horizontal flow on the eigenfrequencies. From equation (3.29) we see that a sufficient condition for k_x to be constant (thus maintaining integrability) is $\partial c/\partial x = \partial v_x/\partial x = \partial v_z/\partial x = 0$. In particular this occurs for the stringent criteria that v_x is a non-zero constant, $v_z = 0$, and $c = c_0$. Other selections also maintain integrability, but this choice of parameters leads to results which are easily interpreted.

Table 3.2 shows the frequency shifts from EBK quantization as well as those from adiabatic switching. We see that:

- (a) The fractional frequency shift decreases as n increases.
- (b) The fractional frequency shift increases as ℓ increases.
- (c) The fractional frequency shift increases as v_x increases.

Notice that the shifts for ℓ and n are of the opposite sense than for the sound speed perturbation of §3.3.

To explain these trends we can expand the EBK quantization condition as we did in the previous section. In this case, however, the simplicity of the perturbation (a constant v_x acting

Table 3.2: Frequency shifts for a horizontal velocity perturbation. Some entries have been repeated in order to display trends.

n^a	ℓ^b	v_x^c	$[\Delta\omega/\omega]_{AS}^d$	$[\Delta\omega/\omega]_{EBK}^e$
1 ^f	200		3.622	3.576
2	200		4.286	4.247
1	400		5.123	5.057
1	200	0.01	7.9×10^{-3}	7.9×10^{-3}
2	200	0.01	6.7×10^{-3}	6.7×10^{-3}
3	200	0.01	5.9×10^{-3}	5.9×10^{-3}
4	200	0.01	5.3×10^{-3}	5.3×10^{-3}
1	100	0.01	5.6×10^{-3}	5.6×10^{-3}
1	200	0.01	7.9×10^{-3}	7.9×10^{-3}
1	400	0.01	1.1×10^{-2}	1.1×10^{-2}
1	800	0.01	1.6×10^{-2}	1.6×10^{-2}
1	200	0.005	4.0×10^{-3}	4.0×10^{-3}
1	200	0.01	7.9×10^{-3}	7.9×10^{-3}
1	200	0.02	1.6×10^{-2}	1.6×10^{-2}
1	200	0.04	3.2×10^{-2}	3.2×10^{-2}
1	200	0.08	6.3×10^{-2}	6.3×10^{-2}

^a Vertical mode number.

^b Horizontal mode number.

^c Horizontal velocity.

^d Relative frequency shifts from adiabatic switching.

^e Relative frequency shifts from EBK quantization.

^f The first three rows give unperturbed frequencies for comparison purposes.

on a constant k_x) allows us to write down the correct result. The fractional frequency shift is give by a Doppler shift:

$$\frac{\Delta\omega}{\omega} = \frac{k_x v_x}{\omega} = k_x v_x \left[\frac{2gk_x}{\mu} \left(n + \frac{\mu}{2} \right) \right]^{-\frac{1}{2}}, \quad (3.38)$$

where we have used equation (3.11) to substitute for ω . Since $k_x \propto \ell$, the dependencies noted above are correctly explained by equation (3.38).

In Figure 3.3 the top panel shows two raypaths in a small portion of the acoustic cavity. The dotted line is a raypath in a polytropic atmosphere while the solid line is a raypath in the model including the horizontal flow. The effect of the flow in advancing the raypath motion is clearly visible. The second panel shows the evolution of the ray frequency as a function of switching time. Again, the shift between integrable systems is quite smooth.

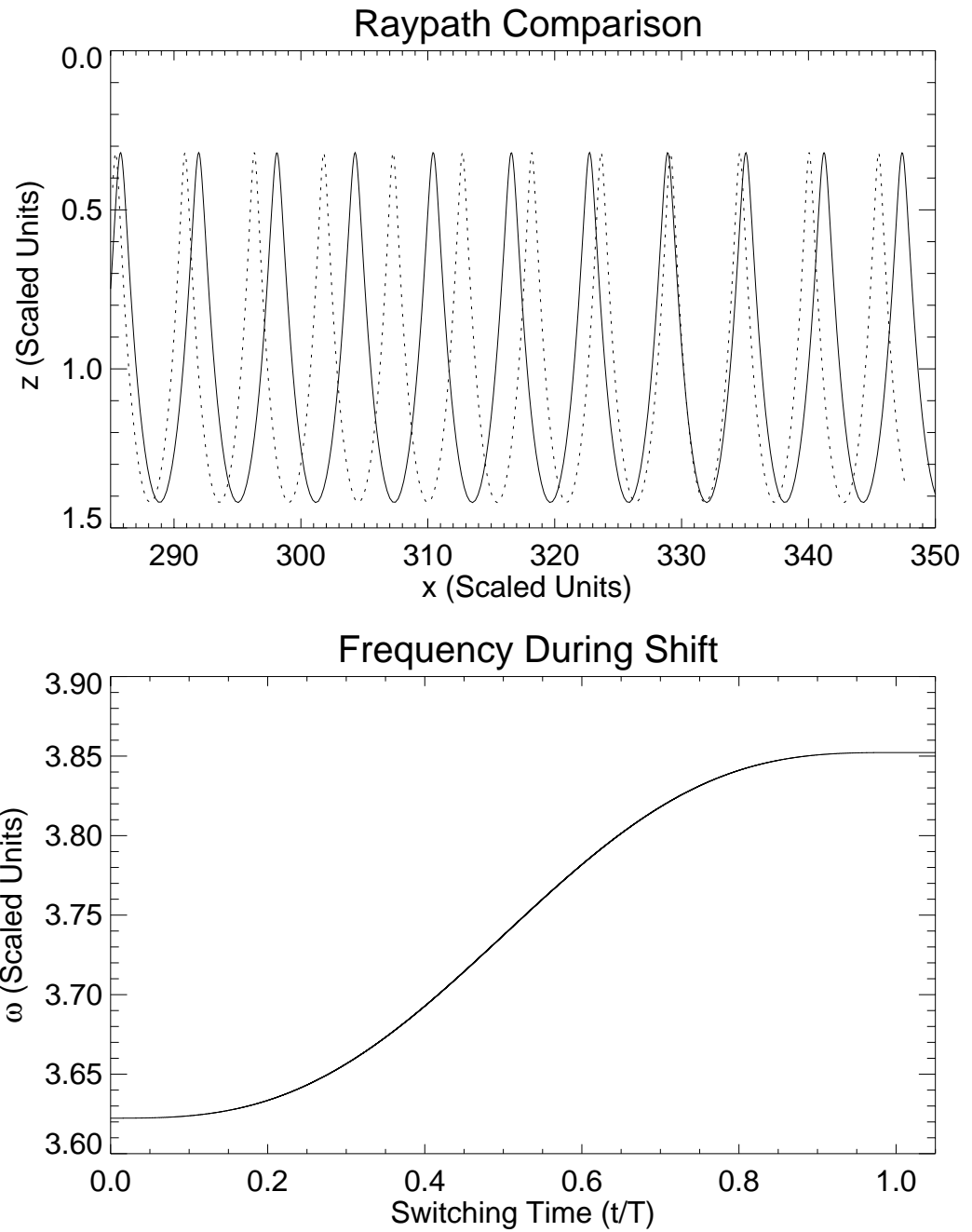


Figure 3.3: A raypath and the evolution of the eigenfrequency for the perturbation of §3.4. Results for a $n = 1$, $\ell = 200$ mode and a Doppler shift perturbation with $v_x = 0.08$. See the text for further discussion.

Chapter 4

Convective Structures

The sound speed and velocity fields of the solar convection zone do not form an integrable system. Within this chapter we introduce several models of convective structures containing non-integrable perturbations and examine their effects on p -mode eigenfrequencies. Although the model of §4.1 contains only velocity perturbations, its simple structure provides insight into the behavior of more complex convective structures. In §4.2 we examine a two-dimensional Rayleigh-Bénard convective model which contains both sound speed and velocity perturbations. More realistic convective simulations appear in §4.3 where we treat a model of a cool, compressible plume and §4.4 where we consider a two-dimensional slice of a three-dimensional simulation of compressible convection.

4.1 Cell-like Velocity Perturbation

As a first attempt we choose to model convective cells as velocity perturbations superimposed on a polytropic temperature stratification. Our velocity field is derived from a stream function

$$\psi = \epsilon \sin\left(\frac{2\pi x}{L}\right) \sin\left(\frac{2\pi z}{L}\right), \quad (4.1)$$

where $L = 2\pi R_{\odot}$ is the horizontal length of the cavity and ϵ is the perturbation strength. Although this parameterization unphysically assumes an incompressible fluid, we are more concerned with the physical insight we can derive from this model than its self-consistency. With

the normal stream function relations ($\mathbf{v} = \nabla \times \psi \hat{\mathbf{y}}$ where $\hat{\mathbf{y}}$ is a unit vector perpendicular to our other coordinates), equation (4.1) gives the velocity field

$$v_x = \frac{\epsilon}{R_\odot} \sin\left(\frac{x}{R_\odot}\right) \cos\left(\frac{z}{R_\odot}\right) \quad \text{and} \quad v_z = -\frac{\epsilon}{R_\odot} \cos\left(\frac{x}{R_\odot}\right) \sin\left(\frac{z}{R_\odot}\right). \quad (4.2)$$

We plot streamlines for this flow in Figure 4.1.

Given this perturbation, we use adiabatic switching to investigate the dependence of eigenfrequencies on the parameters ϵ , n , and ℓ . Our results are shown in Table 4.1 and suggest the following trends:

- (a) The fractional frequency shift decreases as n increases.
- (b) The fractional frequency shift increases as ℓ increases.
- (c) The fractional frequency shift increases as ϵ increases.

Although the sense of these trends are the same as for the Doppler shift of §3.4, the functional form of the shifts is different. Notably, the frequency shift does not linearly depend on ϵ ; instead, it is quadratic in ϵ .

To explain these relations, we turn, with an important caveat, to the mathematical framework developed in §3.3. We are no longer working with an integrable system and hence the quantization conditions of equation (2.47) are not well defined. For example, consider the vertical quantization condition for the lowest mode:

$$\oint k_z dz = \oint \left[\frac{(\omega - \mathbf{k} \cdot \mathbf{v})^2 - \omega_c^2}{c^2} - k_x^2 \right]^{\frac{1}{2}} dz = \pi. \quad (4.3)$$

In earlier applications the integrand depended solely on z and the integral was performed at an arbitrary value of x . Now k_x depends on both x and z and is no longer a constant of the motion; hence, the integral depends on the x at which it is evaluated. The condition is ill-defined, but the KAM theorem and the empirical success of adiabatic switching suggest that the quantization conditions are accurate for small perturbations. In this spirit, we average equation (4.3) over the horizontal dimension while acknowledging that we should use the results for guidance, and not absolute statements, concerning the eigenfrequency shifts.

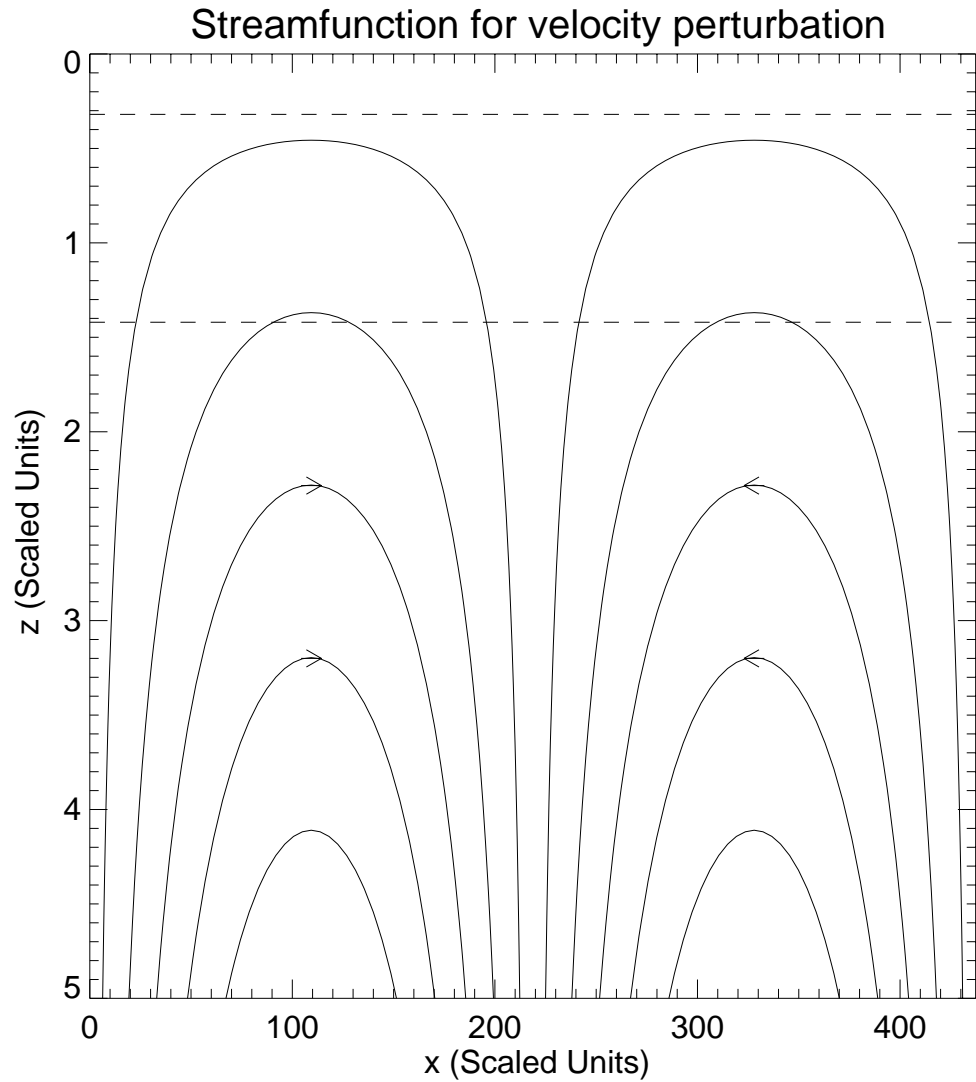


Figure 4.1: Streamlines for the velocity perturbation of §4.1. The two dashed lines near the top of the plot delineate the resonant cavity of the $n = 1$, $\ell = 200$ polytropic mode shown in Figure 3.1. The WKB criterion is clearly met in both directions. In order to resolve the cavity, the closure of the streamlines at lower depths is not shown.

Table 4.1: Frequency shifts for convective cells composed of velocity perturbations. Some entries have been repeated in order to display trends.

n^a	ℓ^b	ϵ^c	$[\Delta\omega/\omega]^d$
1	200	0.04	-1.3×10^{-3}
2	200	0.04	-9.0×10^{-4}
3	200	0.04	-7.0×10^{-4}
4	200	0.04	-5.7×10^{-4}
5	200	0.04	-4.8×10^{-4}
1	100	0.04	-6.3×10^{-4}
1	200	0.04	-1.3×10^{-3}
1	300	0.04	-1.9×10^{-3}
1	400	0.04	-2.5×10^{-3}
1	500	0.04	-3.2×10^{-3}
1	800	0.04	-5.1×10^{-3}
1	200	0.01	-7.9×10^{-5}
1	200	0.02	-3.2×10^{-4}
1	200	0.04	-1.3×10^{-3}
1	200	0.05	-2.0×10^{-3}
1	200	0.08	-5.1×10^{-3}

^a Vertical mode number.

^b Horizontal mode number.

^c Perturbation strength.

^d Relative frequency shifts from adiabatic switching.

Our system contains no perturbation to the sound speed, and thus none to the acoustic cutoff frequency, but now we must include both the Doppler term of equation (3.25) as well as a perturbation to k_x . So,

$$\oint k_z dz = \oint \left[\frac{(\omega_0 + \Delta\omega - \mathbf{k}_0 \cdot \mathbf{v})^2 - \omega_{c,0}^2}{c_0^2} - (k_{x,0} + \Delta k_x)^2 \right]^{\frac{1}{2}} dz = \pi, \quad (4.4)$$

where quantities with a 0 subscript correspond to the polytropic reference state and are thus independent of x . Averaging in the horizontal direction, treating $\mathbf{k}_0 \cdot \mathbf{v}$ as a small parameter, and performing the same expansion as in §3.3, yields

$$\frac{\Delta\omega}{\omega_0} = \frac{1}{L} \int dx \left[\oint \frac{\mathbf{k}_0 \cdot \mathbf{v}}{\omega_0} \frac{dz}{k_{z,0} c_0^2} + \oint \frac{k_{x,0}}{k_{z,0}} \Delta k_x dz \right] \left[\frac{1}{L} \int dx \oint \frac{dz}{k_{z,0} c_0^2} \right]^{-1}, \quad (4.5)$$

where L is the horizontal extent of the domain. From equations (3.14)–(3.17), Hamilton's equations for the unperturbed state, we can rewrite the final term in the first set of brackets as

$$\oint \frac{k_{x,0}}{k_{z,0}} \Delta k_x dz = \oint \Delta k_x dx. \quad (4.6)$$

From the quantization conditions this term is identically zero, leaving as a final result

$$\frac{\Delta\omega}{\omega_0} = \left[\int dx \oint \frac{\mathbf{k}_0 \cdot \mathbf{v}}{\omega_0} \frac{dz}{k_{z,0} c_0^2} \right] \left[\int dx \oint \frac{dz}{k_{z,0} c_0^2} \right]^{-1} \quad (4.7)$$

which should be compared to equations (3.37) and (3.38). Again, we find that the frequency shift depends on the weighted average of the perturbation over the cavity. As an aside, we note that a similar treatment beginning with the horizontal quantization condition yields

$$\frac{\Delta\omega}{\omega_0} = \left[\oint dz \int \frac{\mathbf{k}_0 \cdot \mathbf{v}}{\omega_0} \frac{dx}{k_{x,0} c_0^2} \right] \left[\oint dz \int \frac{dx}{k_{x,0} c_0^2} \right]^{-1}. \quad (4.8)$$

As we now show, these quantization conditions predict that the velocity perturbation of equation (4.2) produces no first-order frequency shift. The sole x -dependence in the integrands of equation (4.7) arises within \mathbf{v} . This dependence is sinusoidal for the perturbations we are considering and hence the horizontal integral of equation (4.7) is identically zero. Somewhat more generally, we see that this result holds for any convective model where, at every depth, the velocity components satisfy

$$\int_0^L v_x dx = \int_0^L v_z dx = 0. \quad (4.9)$$

In such a flow, a ray whose frequency is boosted at a given point suffers a frequency retardation at a complementary point elsewhere in the domain. To first order, there is no net effect.

Only a small subset of flows exhibit the symmetry necessary for equation (4.9) to be true. However, equation (4.7) allows us to make a much more general statement about the effects of flows on eigenfrequencies. The shift produced by the vertical component of a flow is

$$\frac{\Delta\omega}{\omega_0} = \left[\int dx \oint \frac{v_z}{\omega_0} \frac{1}{c_0^2} dz \right] \left[\int dx \oint \frac{dz}{k_{z,0} c_0^2} \right]^{-1}, \quad (4.10)$$

where the dependence on $k_{z,0}$ has been cancelled in the first term. This cancellation is vital as the path integral in the numerator is now

$$\oint \frac{v_z}{\omega_0} \frac{1}{c_0^2} dz = \int_{z_1}^{z_2} \frac{v_z}{\omega_0} \frac{1}{c_0^2} dz + \int_{z_2}^{z_1} \frac{v_z}{\omega_0} \frac{1}{c_0^2} dz = 0, \quad (4.11)$$

where z_1 and z_2 are the vertical boundaries of the acoustic cavity. Thus, the vertical component of any advective flow produces no net first-order effect. This is not the case for horizontal flows which, as we saw in §3.4, can produce first-order shifts.

The asymmetry arises from the observation that rays are trapped in the vertical direction but not in the horizontal.¹ Since a ray never reverses its horizontal motion, the horizontal wavenumber k_x of any ray maintains the same sign along its trajectory. Conversely, the vertical wavenumber k_z changes sign at each caustic. Because of this asymmetry, the expressions $\oint dx$ and $\oint dz$ have very different mathematical meanings:

$$\oint dx = \int_0^L dx = L \quad \text{while} \quad \oint dz = 0. \quad (4.12)$$

For a more physical explanation, consider that during an ideal switching (of infinite extent in time) a ray comes arbitrarily close to any point in the cavity. The horizontal velocity field at a given point interacts with rays with only one sign of k_x and imparts a net frequency shift. At the same point the vertical flow will encounter two manifestations of every ray, differing only in the sign, but not the magnitude, of k_z . To first order the effect of the vertical flow on these two

¹ It is possible to construct flows where a ray is trapped in the horizontal direction as well, however they do not correspond with reasonable solar flows and we do not consider them here.

rays will be equal and opposite, leaving no net frequency shift.²

For the flow under consideration, the horizontal contribution to the frequency shift is zero, to first order, from the argument summarized by equation (4.9). The effects of vertical flows are negated, to first-order, by either equation (4.9) or (4.11). Regardless of the causal agent, we expect a non-zero second-order frequency shift, as can be shown by the following argument, originally due to Brown (1984).

A region containing anti-symmetric flows produces no first-order frequency shift. However, a ray will take more time to traverse a region when traveling against the flow ($\mathbf{k} \cdot \mathbf{v} < 0$) than to cross a region where the ray and the flow are co-directional ($\mathbf{k} \cdot \mathbf{v} > 0$). The difference in crossing times between the two regions is of order $\mathbf{k} \cdot \mathbf{v}/\omega$, while the frequency shift in the counter-propagating region is $-\mathbf{k} \cdot \mathbf{v}/\omega$. The result is a fractional frequency shift

$$\frac{\Delta\omega}{\omega} \propto -\left(\frac{\mathbf{k}_0 \cdot \mathbf{v}}{\omega}\right)^2. \quad (4.13)$$

With this result we can anticipate the frequency shifts from a domain including the flow of equation (4.2). First, we expect to observe a fractional frequency shift proportional to ϵ^2 . From equations (3.24) and (3.11) we note that k is proportional to ℓ while ω^2 is proportional to ℓ and to $(n + \mu/2)$. Hence, we also expect a fractional frequency shift which is proportional to ℓ , and inversely dependent on n . As we see in Table 4.1, adiabatic switching confirms these expectations.

Although we have worked solely with advective flows in this section, our results can be extended to sound speed perturbations. The shift from a perturbation with both horizontal and vertical dependencies can be written as

$$\frac{\Delta\omega}{\omega_0} = \left[\int dx \oint \frac{\Delta c}{c_0} \frac{dz}{k_{z,0} c_0^2} \right] \left[\int dx \oint \frac{dz}{k_{z,0} c_0^2} \right]^{-1}, \quad (4.14)$$

which reduces to equation (3.37) in the appropriate limit. Thus, any antisymmetric perturbation

² In earlier calculations involving integrals over z , such as equation (3.6), the positive and negative branches of k_z prevent the cancellation of the integral.

to the sound speed satisfying

$$\int \Delta c dx = 0 \tag{4.15}$$

at every depth produces no first-order frequency shift. We saw in §3.3 that first-order shifts from sound speed perturbations are not impossible. However, if symmetry dictates that the frequency shift vanishes to first order, a second-order downward shift will arise for a reason analogous to that described above: rays propagate faster in, and hence spend less time traversing, regions with higher sound speeds.

In the top panel of Figure 4.2 we show a sample raypath after the system has undergone adiabatic switching. The large perturbation to the acoustic cavity occurs despite the small change in the eigenfrequency (compare this to the behavior in Figure 3.2 where the opposite is true). Our EBK analysis of the frequency shifts does assume that perturbations to the acoustic cavity have negligible effects. In this case, the horizontal average of the perturbation to the cavity is zero and we ignore it in the calculations leading to equation (4.7). Presumably there are higher-order effects which we do not consider.

The bottom panel of Figure 4.2 shows the evolution of the ray frequency as a function of switching time. The large oscillations are a characteristic of adiabatic switching in non-integrable systems.

4.2 Rayleigh-Bénard Boussinesq Convection

While the cell studied in the previous section was helpful in shaping our intuition, it was unrealistic in that it did not include perturbations to the sound speed. In this section we explore a model which includes horizontal and vertical variations in both the sound speed and the velocities. Our reference state remains the adiabatically stratified, plane-parallel polytrope described above. We take our parameterization for the convective state from Shirer (1987). It is a two-dimensional, nonlinear model of steady Rayleigh-Bénard convection derived from the Boussinesq fluid equations. We consider the solution with the lowest mode numbers, two cells

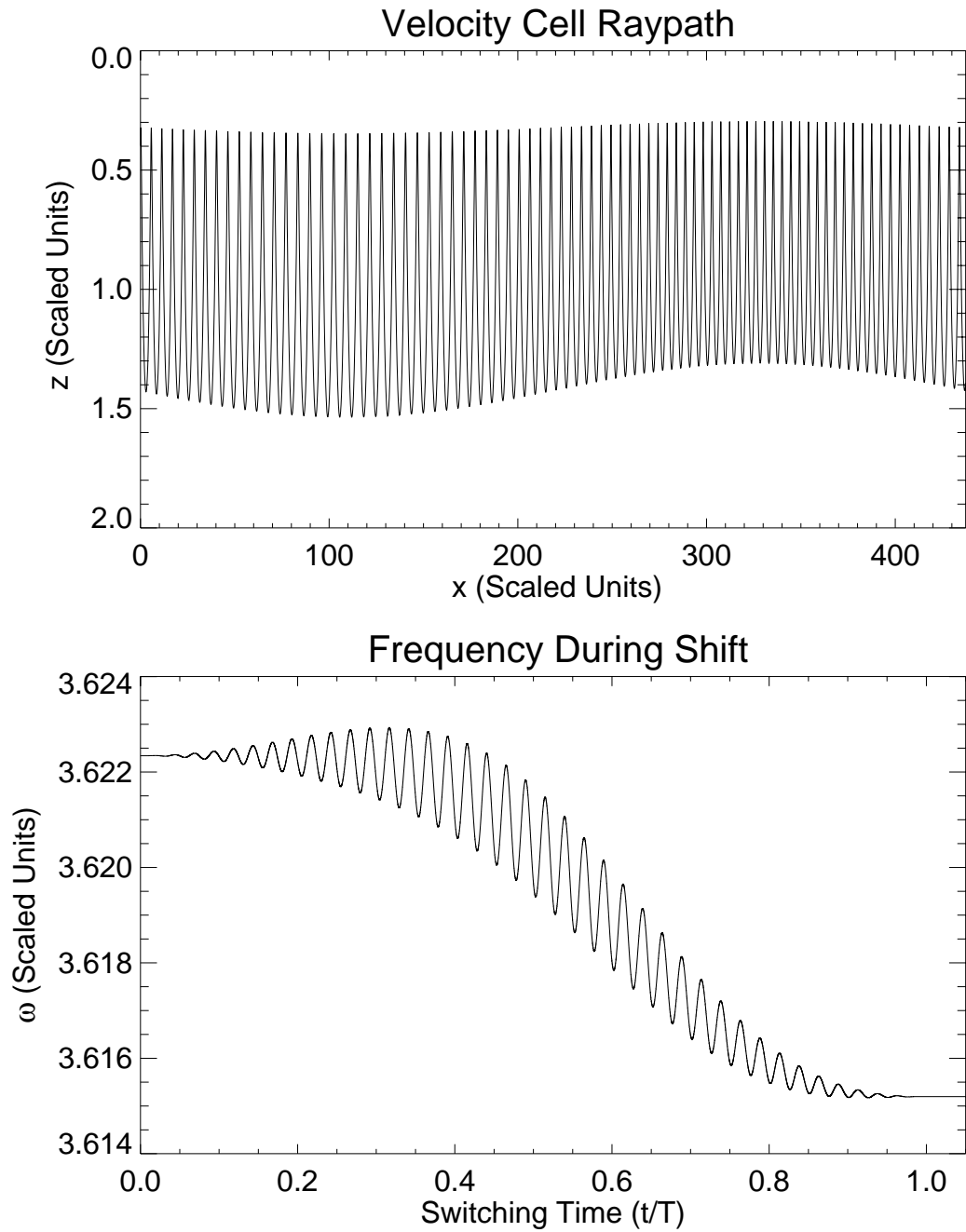


Figure 4.2: A raypath and the evolution of the eigenfrequency for the perturbation of §4.1. Results for a $n = 1$, $\ell = 200$ mode and the velocity perturbation of equation (4.2) with $\epsilon = 0.05$. See the text for further discussion.

in the horizontal direction and one in the vertical.

After converting Shirer's parameterization to our notation, the sound speed is

$$c^2 = \frac{gz}{\mu} + \alpha_1 \cos\left(\frac{2\pi x}{L}\right) \sin\left[\pi\left(1 - \frac{z}{z_T}\right)\right] - \alpha_2 \sin\left[2\pi\left(1 - \frac{z}{z_T}\right)\right], \quad (4.16)$$

where $L = 2\pi R_\odot$ is the length of the domain, z_T is the vertical extent of the cell, and α_1 and α_2 are functions of the product of the thermal diffusivity and the kinematic viscosity, $\kappa\nu$. The velocity perturbations are given by

$$v_x = \gamma_1 \sin\left(\frac{2\pi x}{L}\right) \cos\left[\pi\left(1 - \frac{z}{z_T}\right)\right] \quad \text{and} \quad v_z = \gamma_2 \cos\left(\frac{2\pi x}{L}\right) \sin\left[\pi\left(1 - \frac{z}{z_T}\right)\right], \quad (4.17)$$

where γ_1 and γ_2 are functions of κ and the product $\kappa\nu$. The nonlinear nature of the convection arises from the final term in equation (4.16) which is independent of x . For a linear cell, the perturbation would oscillate in x . Figure 4.3 shows streamlines for the velocity profile given by equation (4.17) as well as the isotherms for the temperature perturbation given by the final two terms of equation (4.16). The standard picture of rising warmer fluid and sinking cooler fluid is seen to hold.

The coefficients of equations (4.16) and (4.17) are

$$\alpha_1 = \frac{gz_T}{\mu} \frac{\sqrt{8}}{\pi \text{Ra}} \frac{a^2 + 1}{a} (\text{Ra} - \text{Ra}_c)^{\frac{1}{2}} \quad (4.18)$$

where

$$a = \frac{2z_T}{L}, \quad \text{Ra} = \frac{gz_T^3}{\kappa\nu\pi^4}, \quad \text{and} \quad \text{Ra}_c = \frac{(a^2 + 1)^3}{a^2} \quad (4.19)$$

are twice the aspect ratio of the convective domain, the Rayleigh number, and the critical Rayleigh number for the onset of convection, respectively. The parameter α_2 is defined as

$$\alpha_2 = \frac{gz_T}{\mu} \frac{1}{\pi \text{Ra}} (\text{Ra} - \text{Ra}_c) \quad (4.20)$$

We also have

$$\gamma_1 = \frac{\pi\sqrt{8}}{z_T(a^2 + 1)} \kappa (\text{Ra} - \text{Ra}_c)^{\frac{1}{2}} \quad (4.21)$$

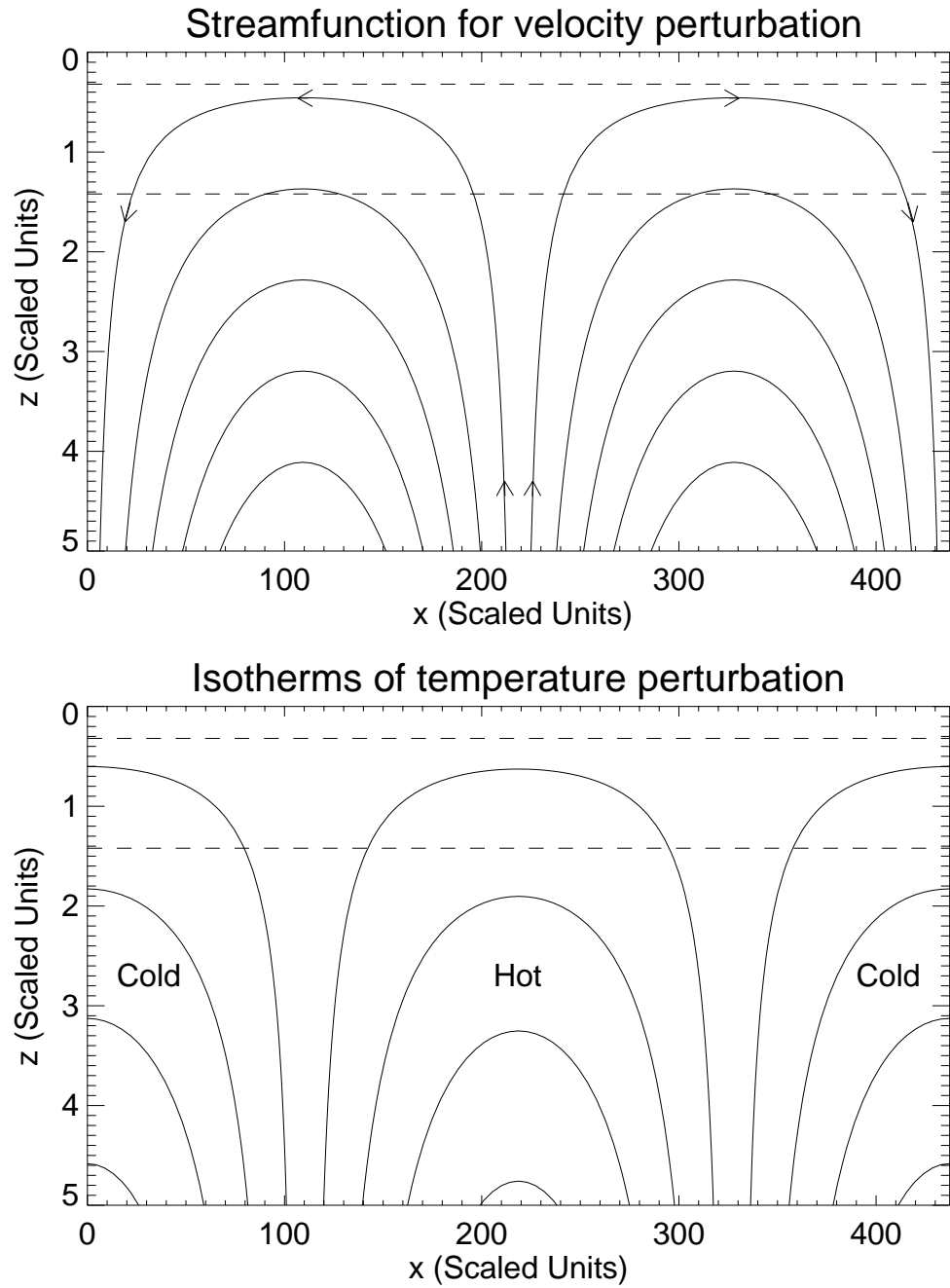


Figure 4.3: Streamlines and isotherms for the convective perturbation of §4.2. The top panel shows streamlines and the bottom panel displays isotherms. Both connect at lower depths. The boundaries of the polytropic cavity of Figure 3.1 are shown as dashed lines.

and

$$\gamma_2 = \frac{a\pi\sqrt{8}}{z_T(a^2+1)}\kappa(\text{Ra} - \text{Ra}_c)^{\frac{1}{2}}. \quad (4.22)$$

From equations (4.18)–(4.22) we can see that a critical parameter governing the size of the perturbations is

$$(\text{Ra} - \text{Ra}_c) = \left[\frac{gz_T^3}{\pi^4} \frac{1}{\kappa\nu} - \frac{(a^2+1)^3}{a^2} \right]. \quad (4.23)$$

To continue, we must specify three free parameters which we take to be z_T , κ , and $(\text{Ra} - \text{Ra}_c)$. Mindful of the constraint that the lengthscales of the fluid motions should be much larger than the lengthscales of the oscillation, we work with the largest possible convective cells, ones the approximate depth of the solar convection zone, and take $z_T = 0.3R_\odot$. These convective motions, then, have similar dimensions to solar giant cells.

Estimates of κ and $(\text{Ra} - \text{Ra}_c)$ in the solar convection zone vary widely over many orders of magnitude. Noting this uncertainty, we choose these parameters so that the size of the perturbations when compared to the ambient sound speed is small. In justification, we note that the velocities of giant cells in the solar convection zone are, if they exist at all, much smaller than even those of supergranules and hence significantly subsonic. Since we are exploring the parameter regime near the boundary of convective instability, small changes in the parameters will have large effects on the size of the perturbations.

From the discussions in §3.3 and §4.1 we can draw some general conclusions about the dependency of the frequency shifts on the parameters. We first consider the velocity perturbations. The sinusoidal structure exhibited in equation (4.17) leads us to expect that the advective perturbations will generate a second-order frequency shift. Since equations (4.21) and (4.22) demonstrate that the magnitude of the vertical velocity is $a \approx 0.1$ times the horizontal velocity, we may safely neglect any shift arising from the vertical component. From the arguments of §4.1, the fractional frequency shift must be of the form

$$\frac{\Delta\omega}{\omega} \sim - \left(\frac{k_x v_x}{\omega} \right)^2. \quad (4.24)$$

Equation (3.11) allows us to write the dependency in terms of the mode parameters, yielding

$$\frac{\Delta\omega}{\omega} \sim -\frac{k_x^2}{\omega^2} \kappa^2 (\text{Ra} - \text{Ra}_c) \sim -\frac{\ell}{n + \mu/2} \kappa^2 (\text{Ra} - \text{Ra}_c). \quad (4.25)$$

Again, as in §4.1, the fractional frequency shift depends quadratically on the strength of the perturbation ($\kappa (\text{Ra} - \text{Ra}_c)^{\frac{1}{2}}$), linearly on ℓ , and inversely on n .

The frequency shift arising from the sound speed perturbation is somewhat more complicated as it combines a strong perturbation whose periodic horizontal structure ensures its effects vanish to first order — the second term of equation (4.16) — and a weak perturbation which will enter at first order — the third term of that equation. After expanding equation (4.16) we find that the shifts produced by the two terms are of equal magnitude and produce a net downshift of

$$\frac{\Delta\omega}{\omega} \sim -\frac{\text{Ra} - \text{Ra}_c}{\text{Ra}}, \quad (4.26)$$

independent of ℓ and n . A further expansion shows that there is an additional downshift of lesser magnitude given by

$$\frac{\Delta\omega}{\omega} \sim -z^2 \frac{\text{Ra} - \text{Ra}_c}{\text{Ra}} \sim -\frac{(n + \mu/2)^2}{\ell^2} \frac{\text{Ra} - \text{Ra}_c}{\text{Ra}}, \quad (4.27)$$

where we have used equation (3.13) to write the dependence of the depth of the acoustic cavity on the mode parameters. Equations (4.25) and (4.26) exhibit different dependencies on the strength of the convective perturbation. Hence, by varying κ and keeping $\text{Ra} - \text{Ra}_c$ constant, we can choose whether the sound speed or the velocity perturbations make the predominant contribution to the frequency shift.

We first choose parameters which make the horizontal velocity perturbation the dominant term and use adiabatic switching to find the eigenfrequencies. The results are shown in Table 4.2. As expected, we see a linear dependence on ℓ and an inverse dependence on n . Also, as expected from equation (4.25), there is a linear dependence on $(\text{Ra} - \text{Ra}_c)$ and a quadratic dependence on κ .

Table 4.2: Frequency shifts for convection cells with dominant horizontal velocity perturbations. Some entries have been repeated in order to display trends.

n^a	ℓ^b	κ^c	$(\text{Ra} - \text{Ra}_c)^d$	$[\Delta\omega/\omega]^e$
1	200	1	0.1	-1.5×10^{-2}
2	200	1	0.1	-1.1×10^{-2}
3	200	1	0.1	-8.7×10^{-3}
4	200	1	0.1	-7.3×10^{-3}
5	200	1	0.1	-6.2×10^{-3}
1	100	1	0.1	-7.9×10^{-3}
1	200	1	0.1	-1.5×10^{-2}
1	300	1	0.1	-2.2×10^{-2}
1	400	1	0.1	-3.1×10^{-2}
1	500	1	0.1	-3.8×10^{-2}
1	200	1	0.03	-4.9×10^{-3}
1	200	1	0.1	-1.5×10^{-2}
1	200	1	0.3	-4.7×10^{-2}
1	200	0.5	0.1	-4.4×10^{-3}
1	200	1	0.1	-1.5×10^{-2}
1	200	2	0.1	-6.2×10^{-2}

^a Vertical mode number.

^b Horizontal mode number.

^c Thermal diffusivity. Scales strength of convective perturbation.

^d See equation (4.23). Scales strength of convective perturbation.

^e Relative frequency shifts from adiabatic switching.

As a second example we consider parameters such that the sound speed and velocity perturbations impart approximately equal frequency shifts. The results are shown in Table 4.3. From our analysis above, we expect the fractional frequency shifts to behave as a combination of the dependencies in equations (4.25), (4.26), and (4.27). This is the case, as is most strikingly seen in the dependence on ℓ in which the fractional frequency shift reaches a minimum value. Two effects contribute to this behavior. The velocity perturbation, from equation (4.25), produces shifts proportional to ℓ and the sound speed perturbation, see equation (4.27), generates shifts proportional to ℓ^{-2} . The location of the minimum, at $\ell \approx 250$, arises from our particular choices for κ and $(\text{Ra} - \text{Ra}_c)$ and can be roughly predicted when more careful track is kept of the constants in equations (4.25) and (4.27). A similar dependence occurs for n , although in this case the minimum occurs at $n \approx 1.5$ and is hence not apparent in Table 4.3.

Finally, in the top panel of Figure 4.4 we show a sample raypath after the system has undergone adiabatic switching. The acoustic cavity has again undergone a significant perturbation which we have ignored in our analysis. The bottom panel shows the evolution of the ray frequency as a function of switching time.

4.3 Compressible Plume

Solar convection only superficially resembles the Rayleigh-Bénard model of the previous section. Rather than symmetric velocity structures, rapid changes in the pressure and density scale heights near the solar photosphere produce convective structures with broad, gentle upflows and narrow, fast downflows. To gain some insight into the effects of such structures, we consider the interactions of p modes with a model of a cool plume descending into an adiabatically stratified compressible envelope (Rast 1998). In the Sun such plumes are believed to be generic features found at the edges of convective cells of all scales.

Pictured in Figure 4.5 are the sound-speed perturbations for the simulation we choose as our convective model. The vertical velocities have nearly an identical structure and the horizontal velocities are significant only at the bottom of the plume. Although we work with

Table 4.3: Frequency shifts for convection cells with equal strength horizontal velocity and sound speed perturbations. Some entries have been repeated in order to display trends.

n^a	ℓ^b	κ^c	$(\text{Ra} - \text{Ra}_c)^d$	$[\Delta\omega/\omega]^e$
1	200	0.03	0.1	-8.94×10^{-4}
2	200	0.03	0.1	-9.06×10^{-4}
3	200	0.03	0.1	-9.25×10^{-4}
4	200	0.03	0.1	-9.48×10^{-4}
5	200	0.03	0.1	-9.74×10^{-3}
1	100	0.03	0.1	-9.24×10^{-4}
1	200	0.03	0.1	-8.94×10^{-4}
1	300	0.03	0.1	-8.94×10^{-4}
1	400	0.03	0.1	-9.00×10^{-4}
1	500	0.03	0.1	-9.06×10^{-4}
1	600	0.03	0.1	-9.10×10^{-4}
1	700	0.03	0.1	-9.15×10^{-4}
1	800	0.03	0.1	-9.21×10^{-4}
1	900	0.03	0.1	-9.26×10^{-4}
1	1000	0.03	0.1	-9.30×10^{-4}

^a Vertical mode number.

^b Horizontal mode number.

^c Thermal diffusivity. Scales strength of convective perturbation.

^d See equation (4.23). Scales strength of convective perturbation.

^e Relative frequency shifts from adiabatic switching.

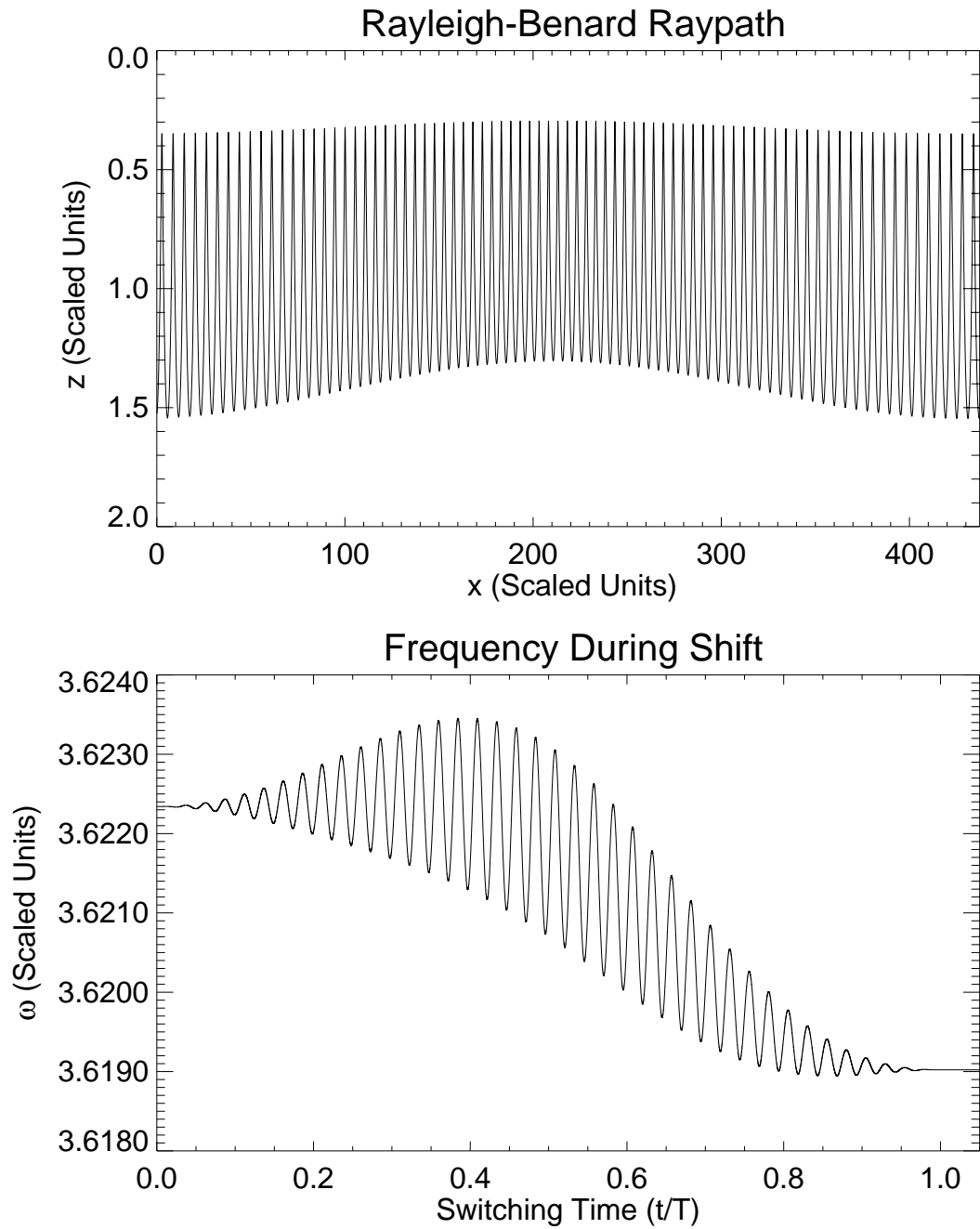


Figure 4.4: A raypath and the evolution of the eigenfrequency for the perturbation of §4.2. Results for a $n = 1$, $\ell = 200$ mode with $\kappa = 0.05$, $(Ra - Ra_c) = 0.1$. See the text for further discussion.

a snapshot of a time-dependent structure, by the time this configuration has been reached the neck of the plume has nearly reached a steady-state. The majority of the interaction between the ray and the plume is with this feature rather than the head which is still rapidly evolving on oscillatory timescales.

Our model is one realization of Rast’s Case B1 at a time, in the non-dimensional units of his paper, of 112.4. Rast’s Table 1 fully documents the model parameters, but we note that for this simulation the Reynolds number is 100 and the Prandtl number is 0.1. The calculation was performed on a stretched grid of 1024×1024 data points covering a 60×60 domain where the units of length are measured in terms of the full width at half maximum of the applied Gaussian temperature perturbation at the top of the atmosphere. We interpolate onto a evenly spaced grid for our use. The polytropic index is $\mu = 3/2$ and the acceleration of gravity is $g = 5/8$, to be compared to the values of 3 and 2.7397, respectively, which were used in earlier sections.

The top boundary of Rast’s model occurs at a temperature of $T = 1$ where a cold Gaussian temperature perturbation with a 30% amplitude is maintained. This level corresponds to $z = 4$ for a polytrope with the above stratification and zero boundary conditions. To complete the atmosphere, we attach to the top of the simulation a $\mu = 3/2$ polytrope extending from $z = 0$ to $z = 4$. This addition generates discontinuities in the sound speed and horizontal velocity perturbations at $z = 4$, but they are primarily confined to a small region near the plume center. In order to investigate the effects of the plume strength on the eigenfrequencies, we isolate the perturbations (both velocity and sound speed) by subtracting off the ambient polytropic stratification. After scaling all of the perturbations by a constant factor we then add them back to the ambient stratification.

Our choice of mode parameters is somewhat limited by the characteristics of the model. The plume extends vertically from $z = 4$ to $z \approx 30$ and we must choose n and ℓ so that the acoustic cavity encompasses these depths. Within this constraint we must also choose an ℓ large enough to satisfy the WKB approximation. The combination of these constraints is restrictive and dictates our choice of $n = 10$ and $\ell = 10$.

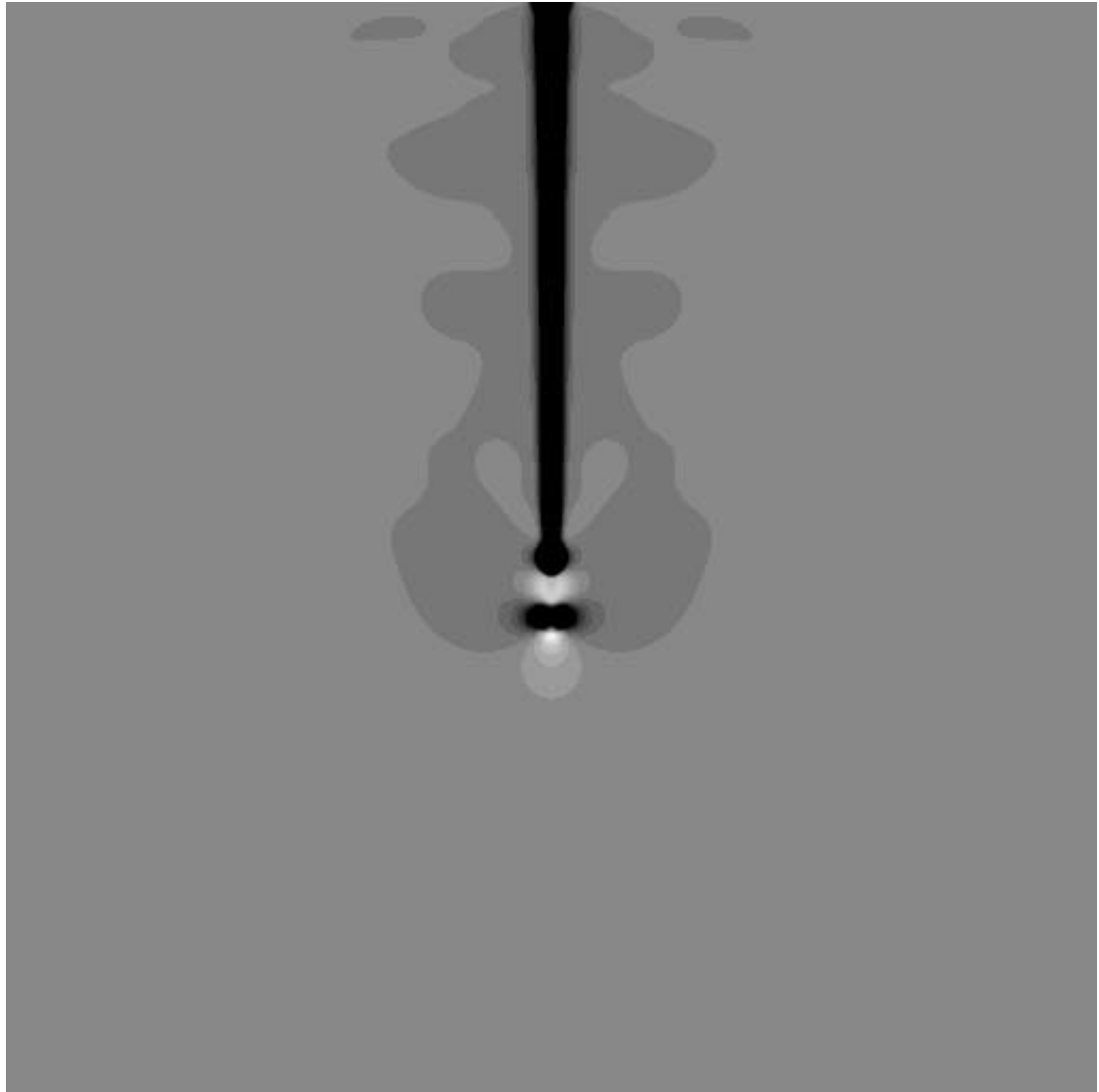


Figure 4.5: Sound speed perturbations for the plume of §4.3. Cooler regions have slower sound speeds and are darker in color. The background stratification has been subtracted and the entire 60×60 computational domain is shown.

Unfortunately the narrow width of the plume implies that $\ell = 10$ only marginally satisfies the WKB requirement. Although we are strictly violating one of the approximations we made in changing to a ray description, we suggest that employing the method of adiabatic switching allows us, in a loose sense, to do so. Recall that we made the WKB approximation in order to pass from a modal to a ray description of the eigenmodes. Since a mode is a three-dimensional object while a ray is merely one-dimensional, the WKB approximation is necessary to ensure that a given ray fully samples the background state. If the background varies on lengthscales which are small compared to the wavelength of the ray, those features which are not directly in the path of the ray will not be included in the determination of the mode eigenfrequency. However, when we employ adiabatic switching a single ray passes through a cavity multiple times. With an infinite switching time a ray will sample every point in the cavity; for the finite switching times we consider the ray will still explore structures on much smaller wavelengths than is possible in any one traversal of the cavity. In essence, adiabatic switching allows the ray to construct a detailed picture of the entire cavity and adjust its eigenfrequency accordingly. Armed with this heuristic argument, we apply adiabatic switching despite the formally invalid nature of the WKB approximation.

Before turning to the eigenfrequency shifts, in the top panel of Figure 4.6 we show a sample raypath in the atmosphere including the plume. The plume itself is not shown, but is centered at $x = 30$ and extends from $z = 4$ through the bottom of the displayed region. As we can see, the raypaths are quite different than in previous examples. Unlike Figures 4.2 and 4.4, the raypaths do not possess well defined caustics. Moreover, in several locations there appear to be more than two rays passing through a single point.

What causes this behavior? Recall the KAM theorem, which states that for sufficiently large perturbations a non-integrable system will contain no invariant tori. When a trajectory passes through a destroyed torus, it is left free to wander in phase space. We believe that the perturbation of the plume is strong enough for that to be the case here. Since the ray is no longer confined to an acoustic cavity, given enough time it will eventually diffuse onto a path which

departs the computational domain. In the bottom panel of Figure 4.6 we show the evolution of the frequency during the switching process. The jagged transition is also much different than we have seen for earlier examples and is also a consequence of the large perturbation provided by the plume.

In Figure 4.7 we plot the dependence of the fractional frequency shift on the plume strength which was adjusted by the scaling process discussed above. The error bars are a direct result of the diffusion of the ray in phase space. Since the final state does not reside on an invariant torus, the ray undergoes Arnold diffusion during the switching process. When not being switched, the eigenfrequency is a constant of the motion, however during adiabatic switching the ray frequency is not constant, and can also drift in phase space. As we discussed in §3.2, we deal with this possibility in our computer code by beginning with several randomly chosen initial conditions and averaging the final eigenfrequencies. The error bars are merely the standard deviations of the mean. Increasing the strength of the plume increases the rate of diffusion, thus explaining the trend in the size of the error bars. Presumably such errors also occur for the non-integrable systems of §4.1 and §4.2, however, we neglected them in those cases because they are much smaller than our quoted results. We also note that the probability that a ray will diffuse out of the computational domain during the switching process increases as the perturbation strength increases. If this occurs, we ignore that ray and proceed to the next initial condition. Hence for stronger plumes we must sample more initial conditions to achieve the same number of completed switchings.

In Figure 4.8 we plot the perturbed quantities from a horizontal slice of the plume. This cut is taken within the acoustic cavity of the unperturbed ray and slices at other depths within the cavity are similar, differing primarily in amplitude. As can be seen, the horizontal velocity profile possesses the symmetry necessary to make the associated frequency shifts cancel to first order. From our earlier arguments, we expect the vertical velocity, despite its significant horizontal integral, to also produce no first-order shift. Both velocity perturbations will produce second-order downshifts. Since the horizontal integral of the sound-speed perturbation is non-

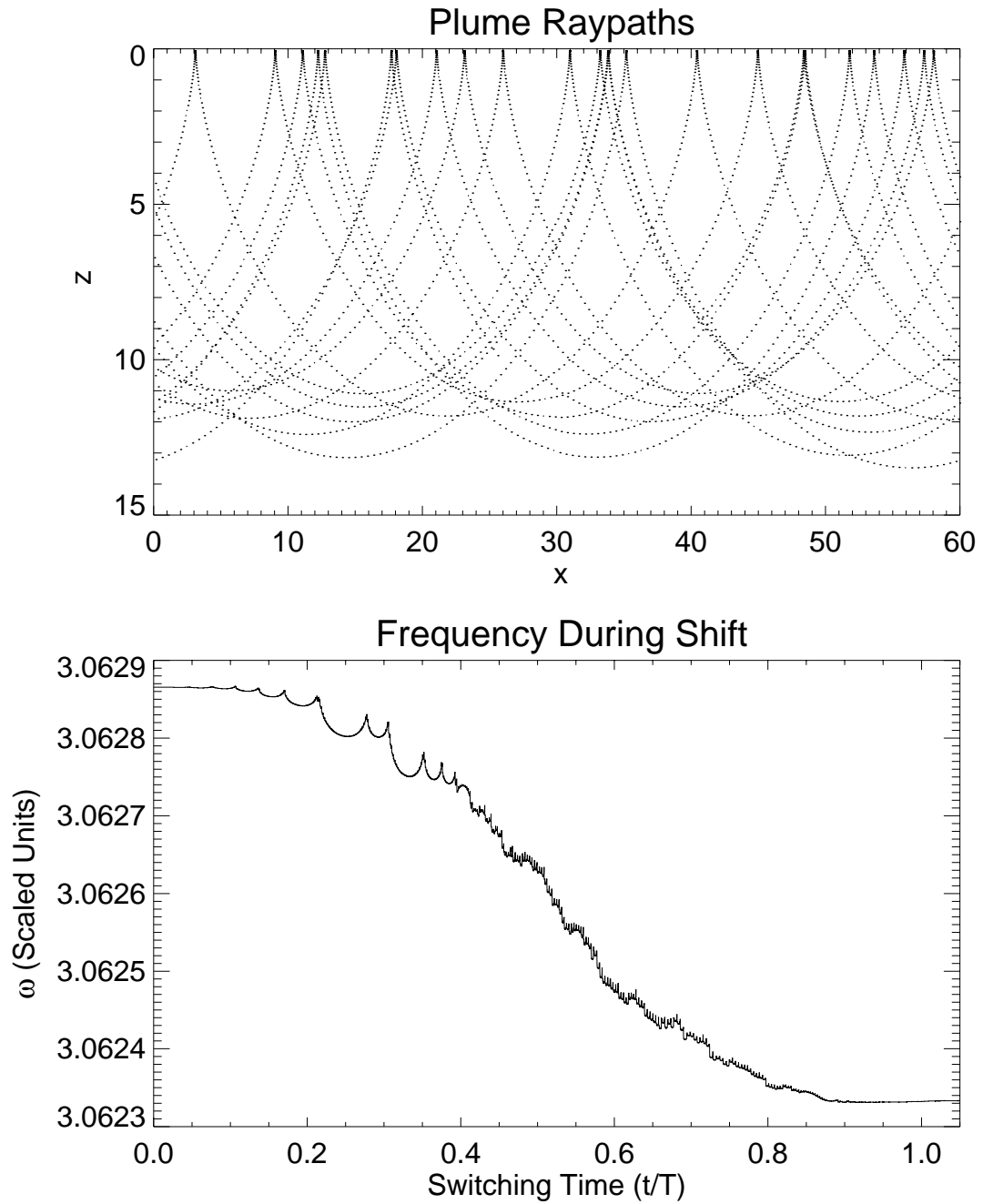


Figure 4.6: A raypath and the evolution of the eigenfrequency for the perturbation of §4.3. Results are for a $n = 10$, $\ell = 10$ mode. The plume is 0.3 times its original strength and is centered on $x = 30$ in the top panel. See the text for further discussion.

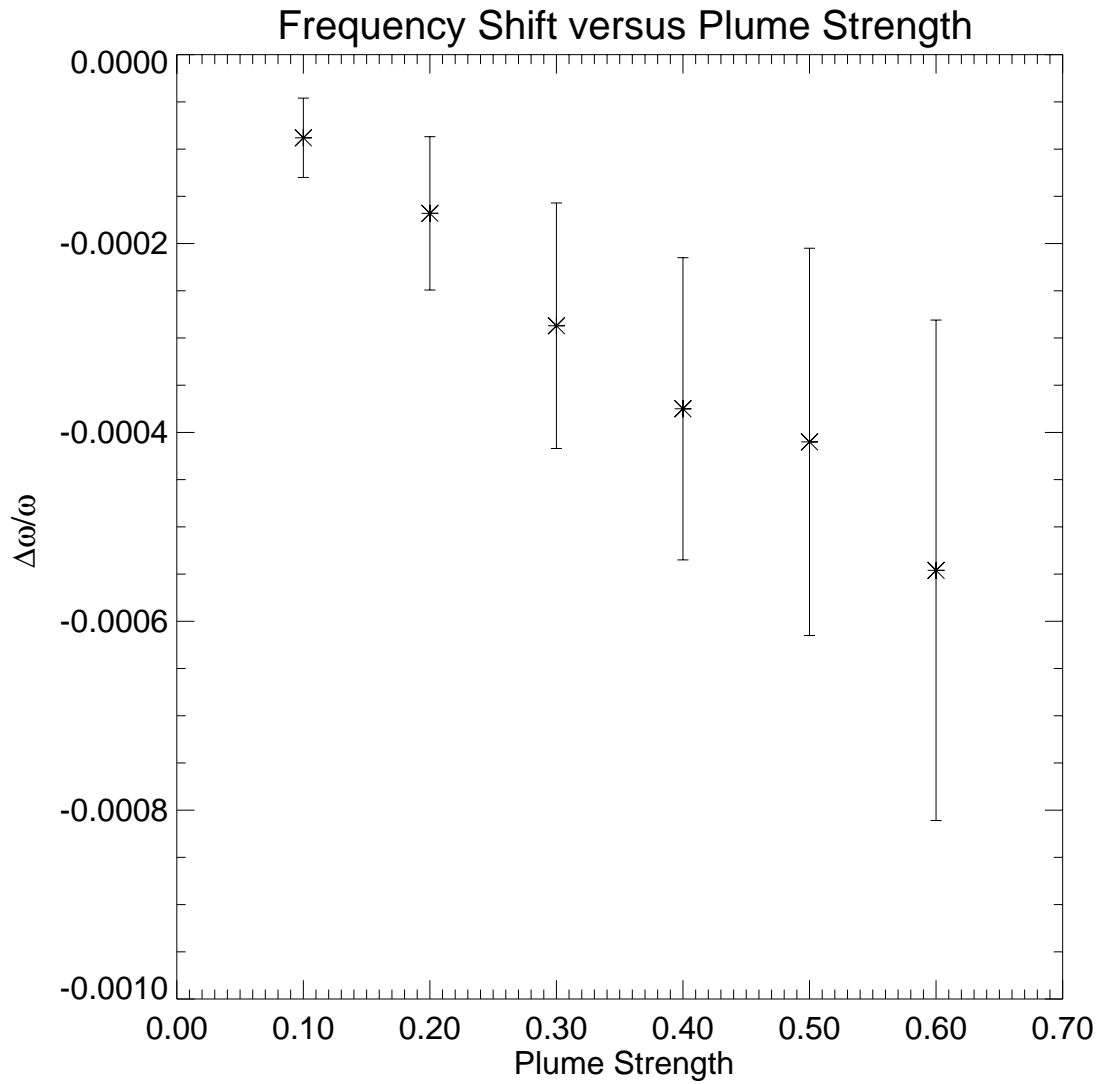


Figure 4.7: Fractional frequency shift versus strength of the plume of §4.3. Results are for an $n = 10$, $\ell = 10$ mode. The source and significance of the error bars is discussed in the text.

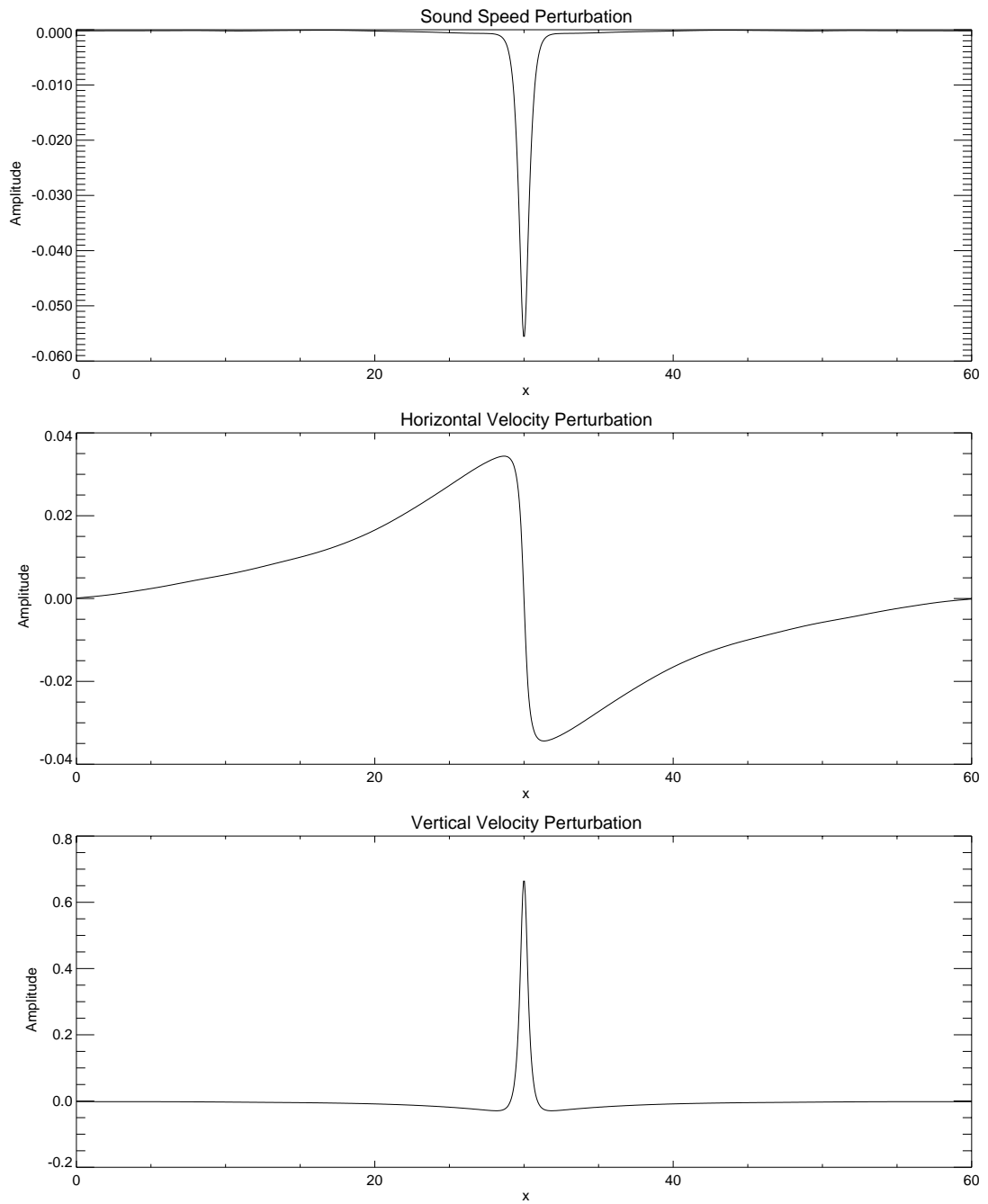


Figure 4.8: Horizontal slices of the plume of §4.3. The slice is at $z = 10$ and the three plots show the sound speed, horizontal velocity and vertical velocity perturbations, respectively.

zero, we expect it to contribute a first-order frequency downshift. For the parameters we are considering, the first-order fractional sound-speed perturbation is larger than the second-order vertical velocity perturbation and so we expect the former to be the dominant term. Since the perturbation is negative, we expect any ray interacting with this plume to undergo a first-order shift which scales with the strength of the plume and is always downward. This expectation is mirrored in Figure 4.7.

4.4 Turbulent Compressible Convection

For our final example, we consider a two-dimensional slice of a snapshot of a time-dependent, three-dimensional model of turbulent compressible convection due to Brummell et al. (1996). It incorporates all of the features we have explored in earlier sections and is the closest approximation to solar convection that we consider. The perturbations for this slice are shown in Figure 4.9. Plumes are seen at either end of the horizontally periodic domain while the center contains a gentler region of upflow.

The complete parameters for this model are listed in Table 1 of Brummell et al. (1996) as case R0,³ although we note that the Prandtl number is 0.1 and the root-mean-square Reynolds number is 932. The computational domain is a plane-parallel box of $192 \times 192 \times 130$ equally spaced grid points covering an aspect ratio of 4:4:1 in the horizontal and vertical coordinates, respectively. To set the length scale, the depth of the box is taken to be unity. The initial stratification corresponds to a polytropic index of $\mu = 1$ and an adiabatic exponent of $\Gamma_1 = 5/3$, which here is not equal to $1 + 1/\mu$. The acceleration of gravity is $g = 20$. As was the case for the plume, the top boundary of the model lies at a fixed temperature of $T = 1$ and supports no vertical velocity perturbations.

Although the initial stratification of the simulation corresponds to a $\mu = 1$ polytrope, convective motions alter the temperature structure so that in this realization it is better characterized by $\mu = 1.42$. We use the latter value for the polytrope we attach to the top of the domain

³ A lower resolution version of the same simulation appears as Case 3 in Cattaneo et al. (1991).

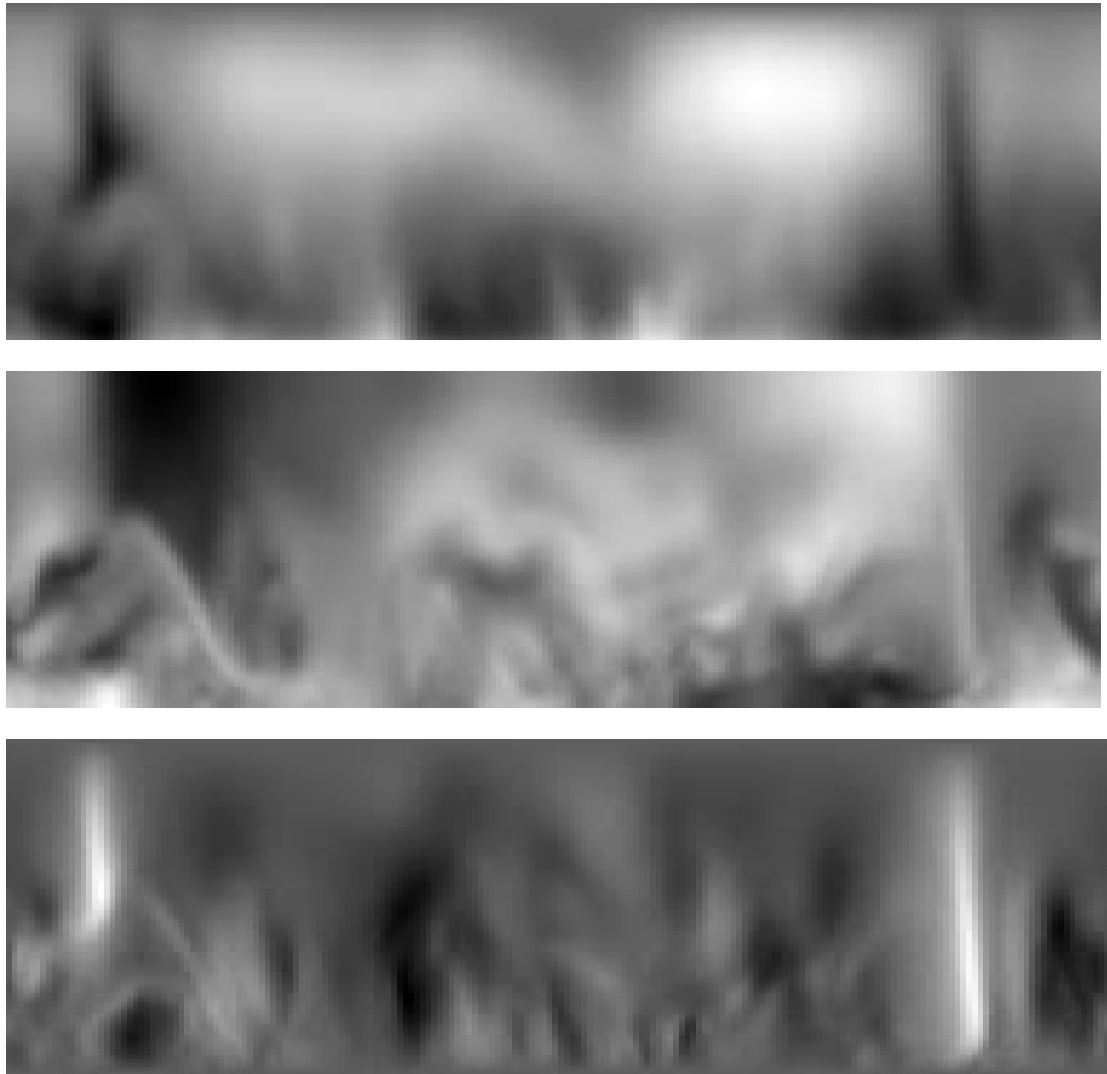


Figure 4.9: Sound speed and velocity perturbations of the convective model of §4.4. From top to bottom, the sound speed, horizontal, and vertical velocity perturbations in a slice at $y = 0.26$ in the dimensions of the model. Light colors represent hotter material and stronger flows. The true aspect ratio is 4:1.

in order to extend it to $z = 0$. Since the temperature stratification is much larger in this model than for the plume of §4.3, the addition is much smaller in extent, covering $0 < z < 0.12$. Unlike the plume, the top boundary for this model has a constant temperature and hence there are no discontinuities in the sound speed or vertical velocity perturbations. The horizontal velocity is discontinuous at $z = 0.12$, but the effects are small. Finally, just as for the plume, we isolate, scale, and return the perturbations to the background stratification to test the dependence of the frequency shift on the amplitude of the motions.

The strong temperature stratification allows us to be somewhat more lenient in choosing the mode parameters than we were in §4.3. Due to the highly turbulent nature of the convection we have almost no hope of strictly satisfying the WKB approximation for all scales of the convective structures. However, the argument made in §4.3 suggests that adiabatic switching will allow us to sample smaller structures than might be expected. As a compromise between sampling a significant portion of the cavity and satisfying the WKB condition, we work with an $n = 1$, $\ell = 10$ mode. A sample raypath and the evolution of the switched frequency are shown in Figure 4.10. Qualitatively, the results are similar to those presented in §4.3 leading us to conclude that the perturbation is strong enough to destroy all of the invariant tori.

We plot horizontal slices of the plume showing the perturbed quantities at a depth of $z = 0.3$ in Figure 4.11. Unlike the plume of §4.3, slices at other depths differ both in amplitude and in structure from those shown. However, we can still make some general statements about the expected frequency shifts. The horizontal velocity perturbation always has a nearly zero horizontal integral implying that it contributes a second-order downshift. For reasons we have previously discussed (see §4.1), the vertical velocity perturbation, regardless of form, will also contribute a second-order downshift. The form of the sound speed perturbation varies from depth to depth and we expect that over the entire convective domain it will average to zero. However, for the particular acoustic cavity we consider, the integral of the perturbation is positive. Hence, it will produce a first-order frequency upshift, although other modes occupying other acoustic cavities will undergo frequency downshifts.

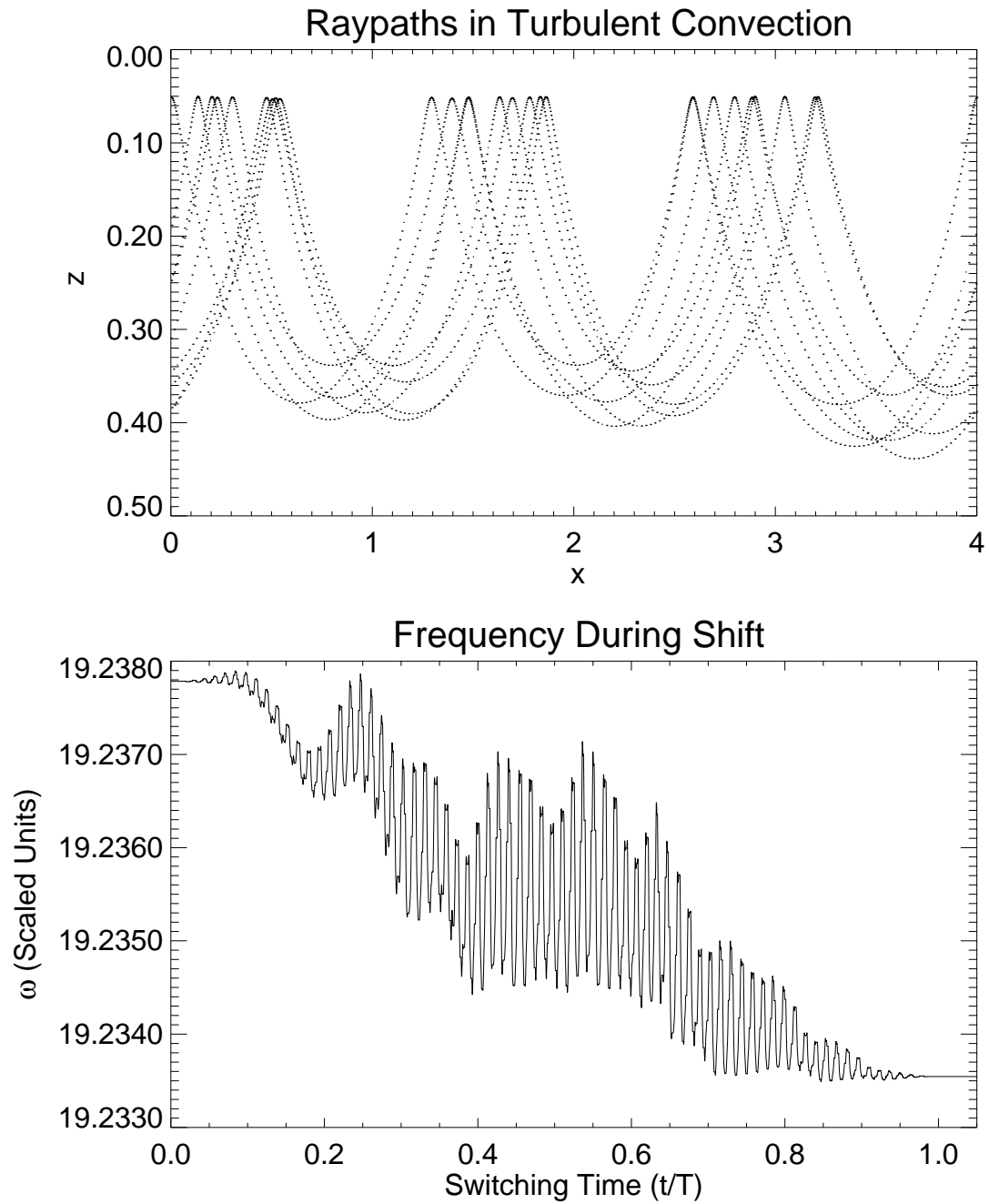


Figure 4.10: A raypath and the evolution of the eigenfrequency for the perturbation of §4.4. Results are for an $n = 1$, $\ell = 10$ mode with the convection at 0.1 times its original strength. See the text for further discussion.

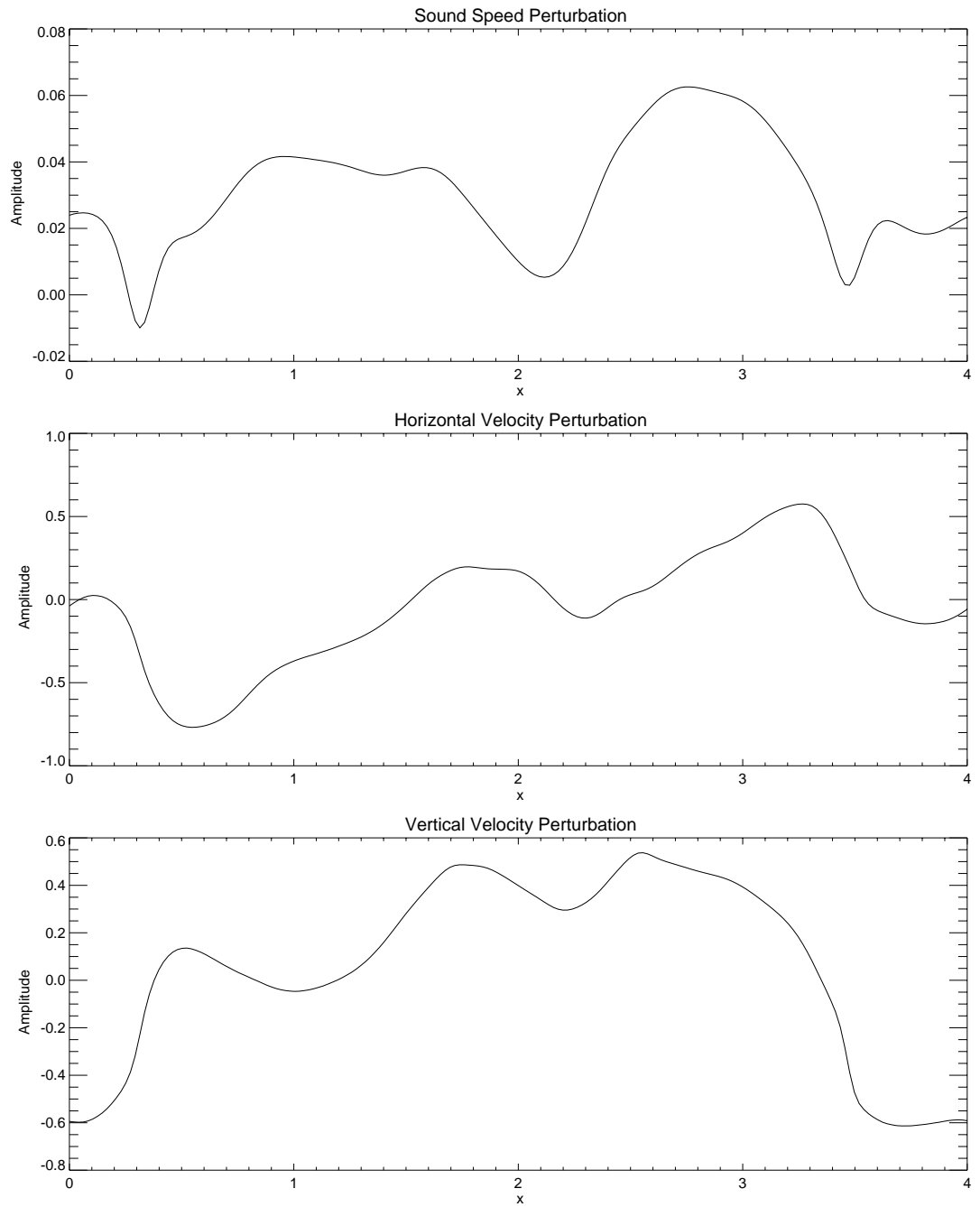


Figure 4.11: Horizontal slices of the plume of §4.4. The slice is at $z = 0.3$ in the units of the model and the three plots show the sound speed, horizontal velocity, and vertical velocity perturbations, respectively.

The net frequency shift is a combination of these different shifts. A rough order-of-magnitude estimate suggests that the velocity perturbations contribute the dominant terms. This is not surprising since the Prandtl number (the ratio of the viscosity to the thermal diffusivity) of this simulation is less than unity — in this case, 0.1. Low Prandtl numbers imply that temperature perturbations (and hence sound speed perturbations) are smoother and weaker than velocity perturbations. Since the velocity perturbations contribute the dominant terms, we expect the fractional frequency shift to be downward and quadratic in the strength of the perturbation.

In Figure 4.12 we plot the dependence of the fractional frequency shift on the strength of the convection for an $n = 1$, $\ell = 10$ mode. The error bars again arise from averaging the results from different initial conditions and signal the presence of destroyed phase-space tori. The frequency shift, while always negative, scales approximately as $\epsilon^{1.5}$, where ϵ is the strength of the perturbation. This dependency is likely a combination of the linear frequency shift arising from the sound speed perturbation and the quadratic perturbation arising from the advective motions.

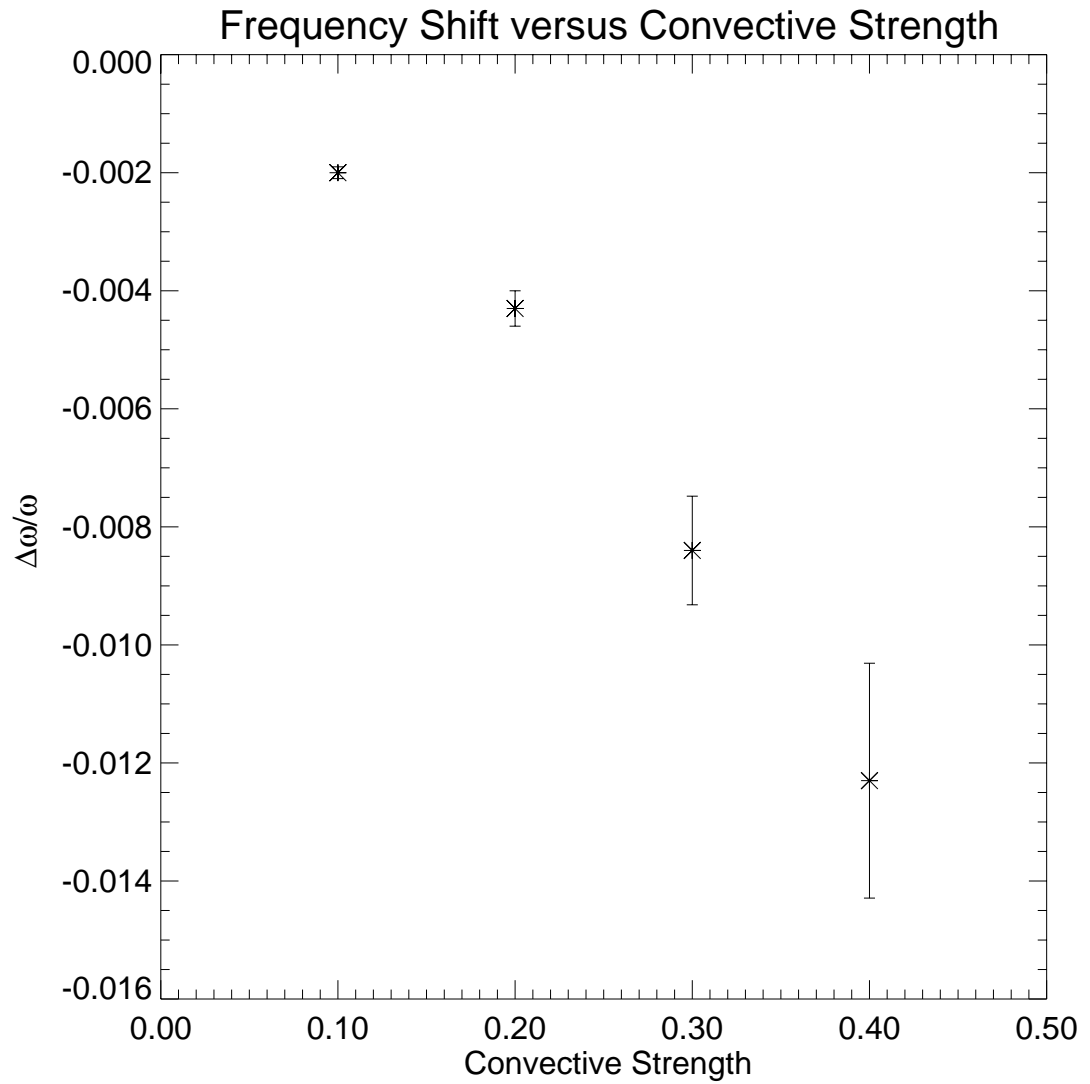


Figure 4.12: Fractional frequency shift versus strength of the convective model of §4.4. The results are for a mode with $n = 1$, $\ell = 10$.

Chapter 5

Conclusions

Adiabatic switching provides a powerful tool for predicting the effects of convective structures on p -mode eigenfrequencies. In §5.1 we summarize a few of our key results and in §5.2 we outline several possibilities for future applications and extensions.

5.1 Results

In the ray approximation, p modes are Hamiltonian systems. The canonical positions and momenta are the position and wavenumber, respectively, while the dispersion relation is the functional form of the Hamiltonian. We have shown that time-independent, horizontally invariant convective models form integrable systems. Their eigenfrequencies can be predicted with adiabatic switching as well as an independent method, semi-classical EBK quantization. The results from the two methods agree. However, we have also shown that adiabatic switching is a viable method of finding the eigenfrequencies of non-integrable systems (in this context, those with horizontal variations), a domain in which EBK quantization can only offer guidance and not precise results.

From our investigations we draw some general conclusions concerning the effects of convection on p -mode eigenfrequencies. Foremost, the fractional frequency shift is the weighted integral of the perturbation over the resonant cavity of the eigenmode. For cases such as the sound-speed perturbation of §3.3 and the Doppler shift of §3.4 where the perturbation is monotonic over the acoustic cavity, the shift is linear in the perturbation strength.

Of more physical interest are examples where the perturbations oscillate in sign. For horizontally antisymmetric perturbations, such as those of §4.1 and §4.2, we have argued on both physical and mathematical grounds that the frequency shift vanishes to first order. Adiabatic switching confirms this result. Furthermore, it demonstrates that a second-order perturbation does exist, resulting from the ray spending extra time in regions of retarding material. We have also shown that vertical velocity perturbations always produce second-order fractional frequency shifts, independent of the perturbation structure.

We also treated even more complex perturbations such as a plume in §4.3 and a two-dimensional slice of a convective model in §4.4. In these complex models, over large enough scales, we expect every perturbation to average to zero — cold, narrow plumes are balanced by broad, warm upflows. If p -mode cavities extended over large scales we would always expect second-order downshifts as any first-order shifts will cancel. However, acoustic cavities have a limited vertical extent and hence may sample a region in which the perturbations do not fully cancel. In that case, the dominant perturbation cannot necessarily be predicted. But, it is known that solar convection is characterized by low Prandtl numbers, implying that velocity perturbations are generally larger in amplitude than sound speed perturbations. Within a typical acoustic cavity, velocity perturbations will be the dominant effect. In the majority of cases, then, we expect second-order frequency downshifts arising from velocity perturbations.

For the simpler perturbations of §4.1 and §4.2 we investigated the dependence on radial mode number n and angular degree ℓ . First-order velocity perturbations vary roughly as $\sqrt{\ell}$ and $1/\sqrt{n}$ and second-order perturbations as the square of these quantities. For sound speed perturbations whose amplitude increases with depth, the fractional frequency shifts generally increase with n and decrease with ℓ . The exact dependency of the shift, however, depends on the functional form of the perturbation.

In addition, we have demonstrated that even mild perturbations can significantly change the structure of the resonant cavity of an eigenmode despite producing only small frequency shifts. As the perturbation strength increases for realistic convective models, the ray trajectories

diffuse and are no longer confined within an obvious cavity. It is an open question as to what extent this occurs in the Sun, particularly as results from time-distance helioseismology imply that ray-like entities which follow predictable trajectories do exist.

It is intriguing to note, as discussed in Gough et al. (1996) and seen in Figure 1.1, that current solar models predict larger sound speeds in the outer portion of the convection zone than are suggested by p -mode observations. Since p -mode eigenfrequencies are proportional to the sound speed, the implication is that theory predicts higher eigenfrequencies than are actually produced by the Sun. We have shown in this work, however, that one effect of convective structures is to lower p -mode eigenfrequencies. This effect is not accounted for in current theoretical solar models and is a potential source of the discrepancy.

Not only is the effect of the proper sign, it has the proper magnitude to explain the difference. As we saw in Chapter 4 the scaling of the frequency shift from convection depends on the integral of the perturbation over the cavity. To make a conservative estimate, we assume that any frequency shift is second-order in the velocity:

$$-\frac{\Delta\omega}{\omega} \sim \frac{v^2}{c^2}. \quad (5.1)$$

Evaluating c at the midpoint of an acoustic cavity gives

$$-\frac{\Delta\omega}{\omega} \sim \frac{v^2}{gR_\odot} \ell \sim \left(\frac{v}{400}\right)^2 \ell, \quad (5.2)$$

where v is the convective velocity in km/s, ℓ is the mode degree, and we have suppressed terms of order 1. For typical supergranular photospheric outflow velocities of 0.5 km/s, the fractional frequency shift is $\approx 3 \times 10^{-4}$. This result is a conservative lower limit: higher ℓ values, higher velocities, and lower-order frequency shifts will all produce larger shifts. Observational determinations of p -mode eigenfrequencies quote error bars of $\Delta\omega/\omega \approx 3 \times 10^{-4}$. Hence we conclude that convective structures will, at the minimum, produce detectable shifts.

5.2 Future Work

Although adiabatic switching is an attractive method for finding p -mode eigenfrequencies, care must be taken to apply it to problems for which it is valid. In the Sun, the true excited objects are global modes. But, inherent in our methodology is the assumption that in the small-wavelength limit these modes may be approximated as one-dimensional rays. We did not discuss the transition between mode and ray. However, one may form a ray by superposing eigenmodes into a wavepacket whose dynamics are then governed by the ray equations (2.38). Bogdan (1997) has shown that, due to the finite number of excited solar p modes, a truly one-dimensional ray cannot be formed. Instead, the smallest wavepacket which can be constructed is ≈ 30 Mm in size. This dimension, characteristic of supergranules, suggests a lower size limit to the structures which can be explored using adiabatic switching. Unfortunately this limit is somewhat more stringent than the WKB criteria, which sets the lower size limit at $\approx 400/\ell$ Mm. It may be possible, as was discussed in §4.3, to show that the method of adiabatic switching loosens these constraints. Although it is not clear how to frame this argument in a rigorous manner, further investigation into the limitations of the WKB approximation is certainly warranted. In any case, the smallest convective structures cannot strictly be treated within our present formulation of adiabatic switching. As discussed in §1.3, other methods, such as the inclusion of a turbulent pressure in the governing equations, must be employed.

A conceptually simple, although perhaps computationally expensive, extension to our work would be the incorporation of a third dimension into the plane-parallel geometry. The system would gain another degree of freedom, however the reference state would remain integrable since another constant of the motion (k_y) would also be added. The transition from two to three dimensions is accompanied by two important geometric effects. As an example of the first, consider the plume of §4.3. In two dimensions it is impossible for rays to avoid the plume; with every traversal of the cavity they pass through the heart of the disturbance. In three dimensions a one-dimensional ray can easily bypass a plume-like structure. Second,

convection in three dimensions is vastly different than in two dimensions. Even highly turbulent two-dimensional convection is organized in cell-like structures such as those of §4.2. Addition of a third dimension results in a much more complicated system. In §4.4 we attempted to account for the second of these differences by taking two-dimensional slices of a three-dimensional model, but a full treatment involves extending our method to include the propagation of rays in three dimensions.

Working in a spherical, rather than plane-parallel, geometry would complement the addition of a third dimension. The solar convection zone extends to a depth of $\approx 0.7R_{\odot}$ and so we expect the effects of curvature to be small. However, we would be able to explore recent spherical shell simulations of the convection zone (Elliott et al. 1998, for example).

Both rotation and magnetic fields can be expressed as additional terms in the governing dispersion relation (Gough 1993). The primary effect of rotation is known: it breaks the spherical symmetry and introduces a dependence of the frequency on m , the azimuthal order in the spherical harmonic decomposition. Magnetic effects are not as well understood. One of the most intriguing, as well as most difficult, questions is the effect of active regions on the eigenfrequency spectrum. Magnetic field strengths reach equipartition in sunspots, becoming strong enough to suppress convective motions as well as have significant impacts on ray propagation. We can also investigate the signatures of a buried magnetic field on the p -mode eigenfrequencies. Detections of such signals would permit predictions of the appearance of magnetic flux at the solar surface.

Finally, power spectra of the solar oscillations show that p modes possess intrinsic line profiles, the source and shape of which is not completely understood. Previous works (Kumar et al. 1994; Roxburgh & Vorontsov 1995; Rast & Bogdan 1998) have treated the effects of intrinsic damping, noise, and source structure on the line profiles. Intriguingly, the error bars of Figures 4.7 and 4.12 can also be interpreted as linewidths. They arise from the drift of the eigenfrequency in phase space as the ray passes through time-dependent convective structures (in this case, during the switching process). In the Sun, time-dependent convective motions, even those lasting for timescales which are long compared to a p -mode period, will broaden the

mode eigenfrequencies via the process of Arnold diffusion discussed in §2.5. A closer exploration of the error bars we discuss in §4.3 and §4.4 will likely yield insight into the nature of p -mode linewidths.

Bibliography

- Arnold, V. I. 1978, *Mathematical Methods of Classical Mechanics* (New York: Springer-Verlag)
- Baker, N. H. & Gough, D. O. 1979, *ApJ*, 234, 232
- Balmforth, N. J. 1992, *MNRAS*, 255, 632
- Beck, J. G., Duvall Jr, T. L., & Scherrer, P. H. 1998, *Nature*, 394, 653
- Bogdan, T. J. 1997, *ApJ*, 477, 475
- Brillouin, L. 1926, *J. Phys. Radium*, 7, 353
- Brown, T. M. 1984, *Science*, 226, 687
- Brummell, N., Cattaneo, F., & Toomre, J. 1995, *Science*, 269, 1370
- Brummell, N. H., Hurlburt, N. E., & Toomre, J. 1996, *ApJ*, 473, 494
- Brut, F. & Arvieu, A. 1993, *J. Phys. A*, 4749
- Cattaneo, F., Brummell, N. H., Toomre, J., Malagoli, A., & Hurlburt, N. H. 1991, *ApJ*, 370, 282
- Chandrasekhar, S. 1987, *Ellipsoidal Figures of Equilibrium* (New York: Dover Publications, Inc.), 28–30
- Christensen-Dalsgaard, J. 1980, *MNRAS*, 190, 765
- Christensen-Dalsgaard, J. 1997, *Lecture Notes on Stellar Oscillations*, 4th edn., available at <http://www.obs.aau.dk/~jcd/oscilnotes/>
- Cowling, T. G. 1941, *MNRAS*, 101, 367
- Cox, J. P. 1980, *Theory of Stellar Pulsation* (Princeton: Princeton University Press)
- Duvall, Jr., T. L., Kosovichev, A. G., & Murawski, K. 1998, *ApJ*, 505, L55
- Ehrenfest, P. 1917, *Philos. Mag.*, 33, 500
- Einstein, A. 1917, *Verhandl. Deut. Physik. Ges.*, 19, 82, as translated in Engel (1997)
- Elliott, J. R., Miesch, M. S., Toomre, J., Clune, T., & Glatzmaier, G. A. 1998, in *Structure and Dynamics of the Interior of the Sun and Sun-like Stars*, ed. S. Korzennik & A. Wilson (Noordwijk: ESA), 765–770
- Engel, A. 1997, *The Collected Papers of Albert Einstein, Vol. 6, The Berlin Years: Writings, 1914–1917* (Princeton: Princeton University Press), 434–443

- Fetter, A. F. & Walecka, J. D. 1980, *Theoretical Mechanics of Particles and Continua* (New York: McGraw-Hill), 434–458
- Ghosh, P., Antia, H. M., & Chitre, S. M. 1995, *ApJ*, 451, 851
- Goldstein, H. 1965, *Classical Mechanics* (Reading: Addison-Wesley)
- Gough, D. O. 1993, in *Dynamique des Fluides Astrophysiques: Astrophysical Fluid Dynamics*, Les Houches No. XLVII (New York: North-Holland), 399–560
- Gough, D. O., Kosovichev, A. G., Toomre, J., et al. 1996, *Science*, 272, 1296
- Gruzinov, A. V. 1998, *ApJ*, 498, 458
- Hénon, M. & Heiles, C. 1964, *AJ*, 69, 73
- Johnson, B. R. 1985, *J. Chem. Phys.*, 83, 1204
- Keller, J. B. 1958, *Ann. Phys. (N.Y.)*, 4, 180
- Keller, J. B. & Rubinow, S. I. 1960, *Ann. Phys. (N.Y.)*, 9, 24
- Kumar, P., Goldreich, P., & Kerswell, R. 1994, *ApJ*, 427, 483
- Lamb, H. 1932, *Hydrodynamics*, 6th edn. (Cambridge University Press)
- Lavelly, E. M. & Ritzwoller, M. H. 1992, *Phil. Trans. R. Soc. Lond. A*, 339, 431
- . 1993, *ApJ*, 403, 810
- Leibacher, J. & Stein, R. F. 1971, *Astrophys. Lett.*, 7, 191
- Leighton, R. B., Noyes, R. W., & Simon, G. W. 1962, *ApJ*, 135, 474
- Lichtenberg, A. J. & Lieberman, M. A. 1983, *Regular and Stochastic Motion* (New York: Springer-Verlag)
- Murawski, K. & Goossens, M. 1993, *A&A*, 279, 225
- Murawski, K. & Roberts, B. 1993a, *A&A*, 272, 595
- . 1993b, *A&A*, 272, 601
- Nöckel, J. U. & Stone, A. D. 1997, *Nature*, 385, 45
- Noid, D. W. & Marcus, R. A. 1975, *J. Chem. Phys.*, 62, 2119
- Patterson, C. W. 1985, *J. Chem. Phys.*, 83, 4618
- Rast, M. P. 1998, *J. Fluid Mech.*, 369, 125
- Rast, M. P. & Bogdan, T. J. 1998, *ApJ*, 496, 527
- Rosenthal, C. S. 1997, in *SCORE'96 : Solar Convection and Oscillations and their Relationship*, 145–160
- Rosenthal, C. S., Christensen-Dalsgaard, J., Kosovichev, A. G., Nordlund, Å., Reiter, J., Rhodes Jr, E. J., Schou, J., Stein, R. F., & Trampedach, R. 1998, in *Structure and Dynamics of the Interior of the Sun and Sun-like Stars*, 521–525
- Roxburgh, I. W. & Vorontsov, S. V. 1995, *MNRAS*, 272, 850

- Shampine, L. F. & Gordon, M. K. 1975, *Computer Solution of Ordinary Differential Equations: The Initial Value Problem* (San Francisco: W. H. Freeman)
- Shirer, H. N. 1987, in *Lecture Notes in Physics*, Vol. 271, *Nonlinear Hydrodynamic Modeling: A Mathematical Introduction*, ed. H. N. Shirer (New York: Springer-Verlag), 22–46
- Skodje, R. T. & Cary, J. R. 1988, *Comput. Phys. Rep.*, 8, 221
- Smith, R. S., Shirts, R. B., & Patterson, C. W. 1987, *J. Chem. Phys.*, 86, 4452
- Spiegel, E. 1971, *ARA&A*, 9, 323
- Stix, M. & Zhugzhda, Y. D. 1998, *A&A*, 335, 685
- Swisdak, M. & Zweibel, E. 1999, *ApJ*, 512, 442
- Tabor, M. 1989, *Chaos and Integrability in Nonlinear Dynamics: An Introduction* (New York: Wiley and Sons)
- Ulrich, R. K. 1970, *ApJ*, 162, 993
- Zhugzhda, Y. D. 1998, *A&A*, 332, 314
- Zhugzhda, Y. D. & Stix, M. 1994, *A&A*, 291, 310

Appendix A

Table of Important Symbols

Table A.1: Important symbols. Referenced pages give the location of either the first appearance or a definition.

Symbol	Page	Description
∇_h^2	15	Horizontal Laplacian
$\hat{\cdot}$	17	Unit vector
$'$	102	Eulerian perturbation
a	66	Aspect ratio
\mathbf{a}	101	Marker identifying a fluid element
A	21	Varying plane-wave amplitude
B_1, B_2, B_3, B_4	110,110,110,111	Functions of χ
c	13	Adiabatic sound speed
c_0	45	Polytropic adiabatic sound speed
C	25	Integration curve
\mathbf{f}	13	Force per unit mass
g, \mathbf{g}	17,13	Scalar and vector gravitational acceleration
G	13	Newtonian gravitational constant
h	23	Planck's constant
H, H_0, H_1	24, 35, 35	General, integrable, and non-integrable Hamiltonian
H_ρ	19	Density scale height
I, I_x, I_z	25, 42, 40	General, horizontal, and vertical action variable of action-angle coordinates
k_r, k_ϕ, k_x, k_z	28, 28, 40, 40	Radial, azimuthal, horizontal, and vertical wavenumbers
\mathbf{k}	21	Wavevector

continued on next page

Table A.1 continued

Symbol	Page	Description
K	48	Perturbation wavenumber
ℓ	16	Spherical harmonic degree
L	57	Horizontal dimension of computational domain
L_1, L_2, L_3	112	Differential operators
m	16	Azimuthal order of spherical harmonic
n	16	Radial mode number
N	18	Brunt-Väisälä frequency
p	13	Pressure
\mathbf{p}	23	Canonical momentum
\mathbf{q}	23	Canonical position
Q	101	Generic variable
r	4	Radius
R_\odot	3	Solar radius
Ra, Ra_c	66	Rayleigh number, critical Rayleigh number
s	28	Number of encountered caustics
S	31	Action
t	12	Time
T	35	Switching time
T_x, T_z	43, 43	Periods of horizontal and vertical motion
v_x, v_z	46, 46	Horizontal and vertical velocity
\mathbf{v}	12	Velocity
x	39	Horizontal coordinate
\mathbf{x}	21	Position vector
Y_ℓ^m	16	Spherical harmonic
z	39	Vertical coordinate
z_1, z_2	43	Minimum and maximum depths of acoustic cavity
z_{mid}	43	Average depth of acoustic cavity
z_T	66	Depth of convective cell
α_1, α_2	66, 66	Sound speed perturbation amplitudes
β	18	Adiabatic stratification parameter
γ_1, γ_2	66, 68	Horizontal and vertical velocity perturbation amplitudes
Γ_1	13	Adiabatic exponent

continued on next page

Table A.1 continued

Symbol	Page	Description
δ	102	Lagrangian perturbation
Δ	31	Generic difference
ϵ	26	Small parameter
θ	15	Polar angle
Θ	25	Angle variable of action-angle coordinates
κ	66	Thermal diffusivity
λ	35	Switching function
Λ	21	Ratio of lengthscales
μ	39	Polytropic index
ν	66	Kinematic viscosity
ν_k, ν_x, ν_z	25, 42, 42	Generic, horizontal, and vertical characteristic frequencies of motion
ξ	17	Radial component of the Lagrangian displacement
ρ	12	Density
ϕ	15	Azimuthal angle
φ	21	Varying plane-wave phase
Φ	13	Gravitational potential
χ	16	Divergence of the Lagrangian displacement
ψ	57	Streamfunction
Ψ	19	Scalar variable in wave equation
Ψ_0	21	Constant plane-wave amplitude
ω	21	Frequency
$\tilde{\omega}$	22	Local frequency
ω_c	19	Acoustic cutoff frequency
Ω	46	Polytropic frequency

Appendix B

Fluid Descriptions and Perturbations

At sufficiently small scales all matter is discrete, separated into atoms and molecules. However, for a large class of substances, termed fluids, this discretization is not apparent. Instead, the mean free path of atomic and molecular motion is much smaller than any other relevant lengthscale (for example, the density scale height or the diffusion length). This separation of lengthscales allows one to average over many particles and thus approximate a fundamentally discrete object as a continuous medium. In this appendix, we outline the Eulerian and Lagrangian descriptions of a fluid. While both are valid representations, most of fluid dynamics, including the standard forms of the fluid equations, is conceived and written using the Eulerian description. However, as is seen below, the Lagrangian description occasionally provides simplifications. We also describe the Eulerian and Lagrangian perturbations (which are closely related to their respective fluid descriptions) and demonstrate their commutation properties with respect to three mathematical operators.

As their names suggest, these descriptions are not new. Instead of breaking new ground, this appendix is merely our own organization of the material. Other treatments may be found in Chandrasekhar (1987) and in Chapter 5 of Cox (1980).

B.1 Descriptions

The choice of independent variables differentiates the Eulerian and Lagrangian fluid descriptions. The position vector \mathbf{x} and time t are the independent variables in an Eulerian fluid

and any quantity Q is written as $Q(\mathbf{x}, t)$. This representation is completely general since, in principle, the value of a variable at any point is uncorrelated with the value at a neighboring point (ignoring, for the moment, constraints imposed by the fluid equations).

In contrast, the Lagrangian description divides a fluid into tiny parcels. The independent variables are the time t and a quantity which uniquely identifies a particular fluid element. Often this quantity is taken to be the position of the fluid element at some reference time, but other choices are possible. To acknowledge this ambiguity, I follow the notation of Cox (1980) and denote the identifying marker as \mathbf{a} . Variables are associated with parcels of fluid, not points in space, and are denoted by $Q(\mathbf{a}, t)$.

By supposing the existence of fluid parcels, the Lagrangian description appears, by the application of Ockham's razor, to be inferior to the Eulerian. The need for fluid parcels requires, at some level, that the fluid be smooth enough for neighboring points to share the same physical description; the Eulerian picture does not require this precondition. To resolve this apparent difficulty, recall that, by definition, every fluid possesses a lengthscale where averaging over many particles is permissible. The Lagrangian description is valid when this lengthscale is larger than the size of a fluid parcel. As both descriptions are equally valid, other considerations will dictate which to use for a given problem.

B.2 Mathematical Operations

Due to the choice of independent variables, the usual gradient operator $\nabla = \frac{\partial}{\partial \mathbf{x}}$ is a useful operation in the Eulerian picture. This is not the case in the Lagrangian description where position is not an independent variable; instead $\mathbf{x} = \mathbf{x}(\mathbf{a}, t)$. The appropriate spatial derivative is then $\nabla_{\mathbf{a}} = \frac{\partial}{\partial \mathbf{a}}$.

As time is exclusively an independent variable, $\frac{\partial}{\partial t}$ is useful in both the Lagrangian and Eulerian pictures. However, it is not the same useful operator in both descriptions. In the

Eulerian frame,

$$\frac{\partial}{\partial t} = \frac{\partial}{\partial t} \Big|_{\mathbf{x}}, \quad (\text{B.1})$$

while in the Lagrangian frame,

$$\frac{\partial}{\partial t} = \frac{\partial}{\partial t} \Big|_{\mathbf{a}}, \quad (\text{B.2})$$

with the notation $|_j$ indicating that j is to be held constant during differentiation. For the Eulerian description the time derivative is taken at a point while in the Lagrangian description it is taken with respect to a particular fluid parcel.

The derivative of equation (B.2) is given a special name: the advective, or Stokes, derivative. In the Eulerian description it is often denoted $\frac{D}{Dt}$.¹ Since the derivative is taken with respect to a fluid parcel, the position varies with time. Thus for any Eulerian variable Q associated with the element:

$$\frac{D}{Dt}Q(\mathbf{x}, t) \equiv \frac{\partial}{\partial t} \Big|_{\mathbf{a}} Q(\mathbf{x}(\mathbf{a}, t), t) = \frac{\partial Q}{\partial t} \Big|_{\mathbf{x}} + \frac{\partial \mathbf{x}}{\partial t} \cdot \nabla Q = \frac{\partial Q}{\partial t} + \mathbf{v} \cdot \nabla Q \quad (\text{B.3})$$

where \mathbf{v} is the fluid velocity. In short, for derivatives taken along the motion of a fluid parcel

$$\frac{D}{Dt} = \frac{\partial}{\partial t} \Big|_{\mathbf{a}} = \frac{\partial}{\partial t} \Big|_{\mathbf{x}} + \mathbf{v} \cdot \nabla. \quad (\text{B.4})$$

B.3 Perturbations

Of course, fluids do not always occupy equilibrium configurations. Here we discuss the application of the Eulerian and Lagrangian descriptions to fluid states which are slightly perturbed away from an reference state. Linear perturbation theory postulates that a variable Q in the perturbed state may be expressed as

$$Q = Q_0 + \Delta Q \quad (\text{B.5})$$

where Q_0 is the variable in the reference state and ΔQ is a generic perturbation which is small compared to Q_0 .

¹ Occasionally the more confusing $\frac{d}{dt}$ is used.

Just as both the Eulerian and Lagrangian descriptions can be used to represent fluids, the perturbation of equation (B.5) can be written in different ways. We will discuss two forms, the Eulerian and Lagrangian perturbations, which are closely related to their respective fluid descriptions. As we will see, both perturbations can be considered in either the Eulerian or Lagrangian description. Unfortunately, the literature has not settled on standard symbols for the perturbations. We follow the notation of Cox (1980) and signify the Eulerian and Lagrangian perturbations to a quantity Q by Q' and δQ , respectively.

Figure B.1 illustrates both the Eulerian and Lagrangian perturbations. Position, normally a three-dimensional vector, has been collapsed to one dimension and plotted on the vertical axis; time is shown on the horizontal axis. The slanted lines are streamlines for three parcels of fluid. The dotted lines are streamlines in the reference state (denoted by y_0) while the solid line is a streamline in the perturbed state (denoted by y). Each streamline is further delineated by the position at time t_1 of a fluid parcel (serving as the \mathbf{a} in the Lagrangian description). Thus, in the reference state, a fluid parcel which occupied position x_2 at time t_1 follows the streamline labeled $y_0(x_2)$. Finally, representative parcels of fluid are shown on the streamlines. So, $y_0(x_2)$ and $y(x_2)$ are streamlines for the same fluid parcel, the first tracing the path of the parcel in the reference state, and the second in the perturbed fluid. Although the reference and perturbed states are shown occupying the same positions at time t_1 , in general this need not be the case. Note that the streamlines, although linear in this sketch, are, in general, curved.

An Eulerian perturbation to a variable Q is the difference at the same point and time between the perturbed and reference fluid states. We first treat this perturbation in the Eulerian description. Suppose the two fluid parcels following the streamlines $y_0(x_4)$ and $y(x_2)$ are described by the variable Q . They are different fluid parcels, as indicated by their different positions at time t_1 , yet at time t_2 , they occupy the same position, the latter in the perturbed and the former in the reference model. At this location and moment, the Eulerian variation is

$$Q'(\mathbf{x} = x_3, t = t_2) = Q(\mathbf{x} = x_3, t = t_2) - Q_0(\mathbf{x} = x_3, t = t_2), \quad (\text{B.6})$$

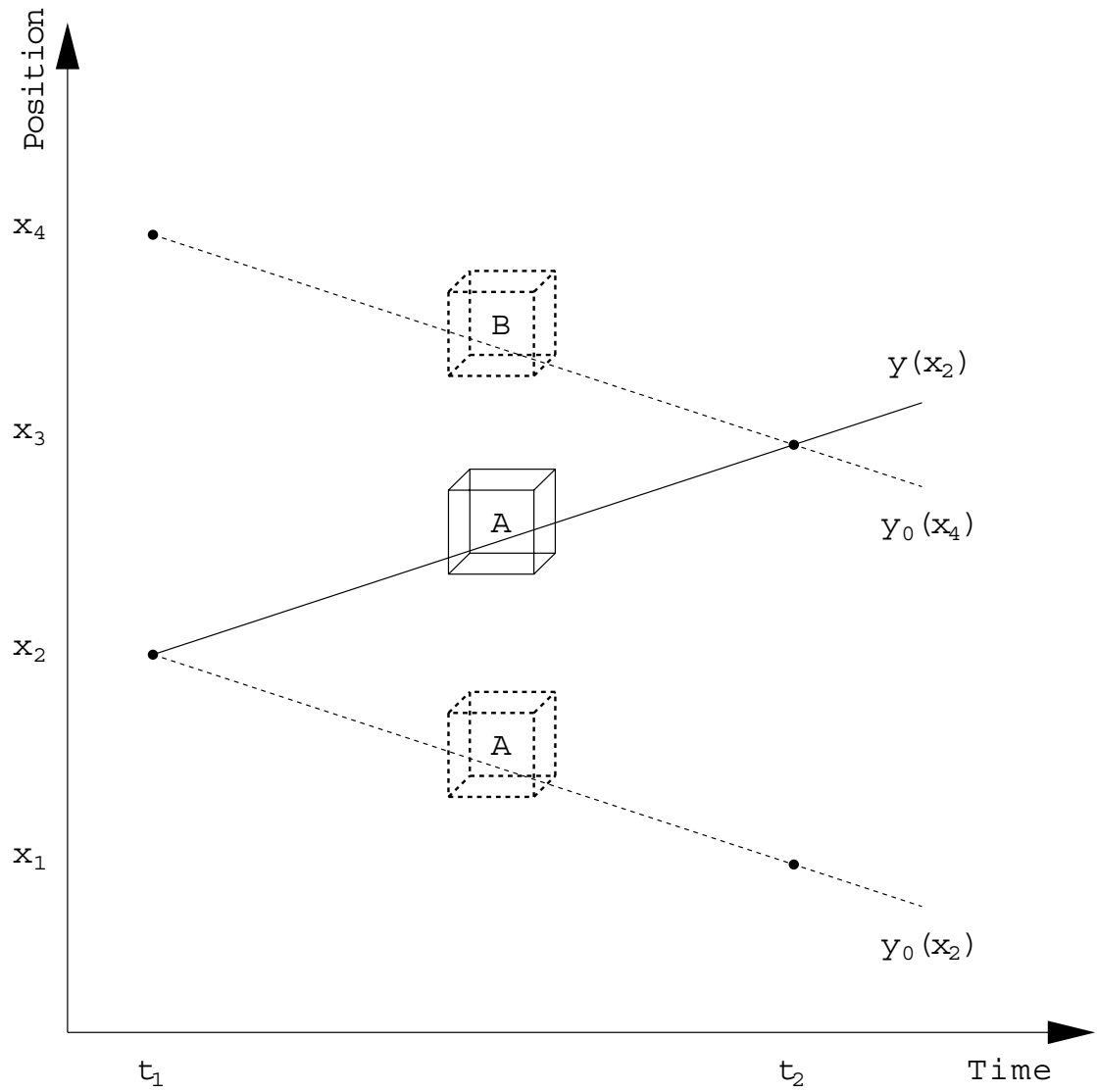


Figure B.1: A pictorial demonstration of the Eulerian and Lagrangian perturbations. See the text for details.

where we have included the independent variables to make it clear we are in the Eulerian description. In general form:

$$Q'(\mathbf{x}, t) = Q(\mathbf{x}, t) - Q_0(\mathbf{x}, t). \quad (\text{B.7})$$

From equation B.7, we see that $\mathbf{x}' = 0$.

A Lagrangian perturbation is the difference between identical fluid parcels, one in the reference state and one in the perturbed system. This perturbation is most naturally described in the Lagrangian description (see below), but it proves useful to examine it in the Eulerian description as well. In the specific case of Figure B.1, we have:

$$\delta Q(\mathbf{x} = x_3, t = t_2) = Q(\mathbf{x} = x_3, t = t_2) - Q_0(\mathbf{x} = x_1, t = t_2). \quad (\text{B.8})$$

Note the distinction between x_3 and x_1 in the final two terms; it forms the crucial difference between the Eulerian and Lagrangian perturbation. In the reference state the variable is evaluated at $\mathbf{x} = x_1$ because this is the location at $t = t_2$ of the reference state parcel which, at $t = t_1$, coincided with the parcel in the perturbed state.

Equation (B.8) gives $\delta \mathbf{x} = x_3 - x_1$. In general $\delta \mathbf{x}$ depends on both the time and position of the observation, so extension to the general case yields

$$\delta Q(\mathbf{x}, t) = Q(\mathbf{x}, t) - Q_0(\mathbf{x} - \delta \mathbf{x}(\mathbf{x}, t), t), \quad (\text{B.9})$$

where we again include the independent variables to make it clear these results apply in the Eulerian description.

As both equations (B.7) and (B.9) are written in the Eulerian description, we may subtract to find

$$\delta Q - Q' = Q_0(\mathbf{x}, t) - Q_0(\mathbf{x} - \delta \mathbf{x}(\mathbf{x}, t), t) \approx \delta \mathbf{x} \cdot \frac{\partial}{\partial \mathbf{x}} Q_0 = \delta \mathbf{x} \cdot \nabla Q_0, \quad (\text{B.10})$$

where the approximation is made to first-order in smallness. At this level of accuracy, Q_0 may be replaced by Q .

Although the Lagrangian description is not as intuitive, it is possible to express both perturbations in its formalism. Recall that the independent variables are no longer time and

position, but time and a marker identifying the fluid parcels (in the case of Figure B.1, initial position). The Lagrangian perturbation in the Lagrangian description is, from Figure B.1,

$$\delta Q(\mathbf{a} = x_2, t = t_2) = Q(\mathbf{a} = x_2, t = t_2) - Q_0(\mathbf{a} = x_2, t = t_2). \quad (\text{B.11})$$

Or, in general form

$$\delta Q(\mathbf{a}, t) = Q(\mathbf{a}, t) - Q_0(\mathbf{a}, t). \quad (\text{B.12})$$

Note the symmetry between this expression and the Eulerian perturbation in the Eulerian description of equation B.7. A simple application of equation (B.12) demonstrates $\delta \mathbf{a} = 0$.

Finally, consider an Eulerian perturbation in the Lagrangian description. From Figure B.1

$$Q'(\mathbf{a} = x_2, t = t_2) = Q(\mathbf{a} = x_2, t = t_2) - Q_0(\mathbf{a} = x_4, t = t_2). \quad (\text{B.13})$$

Since the Eulerian perturbation (usually) compares different fluid parcels, the two terms on the right-hand side of equation (B.13) are evaluated at different \mathbf{a} . In order to generalize this result, notice that $\mathbf{a}' = x_2 - x_4$ in this example. In general, \mathbf{a}' is a function of both time and the initial position of the fluid parcel. So,

$$Q'(\mathbf{a}, t) = Q(\mathbf{a}, t) - Q_0(\mathbf{a} - \mathbf{a}'(\mathbf{a}, t), t). \quad (\text{B.14})$$

As might be expected, this result is quite similar to equation (B.9). Evaluating the difference between equations (B.12) and (B.14) shows that

$$\delta Q - Q' = Q_0(\mathbf{a} - \mathbf{a}'(\mathbf{a}, t), t) - Q_0(\mathbf{a}, t) \approx -\mathbf{a}' \cdot \frac{\partial}{\partial \mathbf{a}} Q_0 = -\mathbf{a}' \cdot \nabla_{\mathbf{a}} Q_0 \quad (\text{B.15})$$

Again, Q may be substituted for Q_0 in the last term without affecting the result.

B.4 Commutation Relations

Using the formalism of the preceding sections, we examine the commutation properties of the perturbations with three mathematical operators. In particular, we demonstrate that

$$[\nabla, \prime] = \left[\frac{\partial}{\partial t} \Big|_{\mathbf{x}}, \prime \right] = \left[\frac{D}{Dt}, \delta \right] = 0 \quad (\text{B.16})$$

and

$$[\nabla, \delta] \neq 0, \left[\frac{\partial}{\partial t} \Big|_{\mathbf{x}}, \delta \right] \neq 0, \left[\frac{D}{Dt}, ' \right] \neq 0, \quad (\text{B.17})$$

where the commutation symbol $[\cdot, \cdot]$ is defined for two operators F and G as $[F, G] \equiv FG - GF$.

Although we can easily extend the results to treat the operator $\nabla_{\mathbf{a}}$, it is rarely used in the literature and so we neglect it here.

B.4.1 Eulerian Perturbation, Commuting Operators

First, consider the Eulerian perturbation. It is simple to prove the two equalities of equation (B.16) using the Eulerian description of equation (B.7). Applying the two operators to the perturbation yields

$$\nabla(Q') = \nabla Q - \nabla Q_0 \quad \text{and} \quad \frac{\partial}{\partial t} \Big|_{\mathbf{x}} (Q') = \frac{\partial}{\partial t} \Big|_{\mathbf{x}} Q - \frac{\partial}{\partial t} \Big|_{\mathbf{x}} Q_0, \quad (\text{B.18})$$

while applying the perturbation to the operators gives

$$(\nabla Q)' = \nabla Q - \nabla Q_0 \quad \text{and} \quad \left(\frac{\partial Q}{\partial t} \Big|_{\mathbf{x}} \right)' = \frac{\partial Q}{\partial t} \Big|_{\mathbf{x}} - \frac{\partial Q_0}{\partial t} \Big|_{\mathbf{x}}. \quad (\text{B.19})$$

The right-hand sides of equations (B.18) and (B.19) are clearly identical, thus proving the first two commutation relations.

B.4.2 Eulerian Perturbation, Non-Commuting Operators

To prove the inequality of equation (B.17), recall from equation (B.4) that the advective derivative is the same as a derivative at constant \mathbf{a} . In light of this fact, it is easiest to consider the Eulerian perturbation in the Lagrangian description. Expanding equation (B.14) to first-order, the Eulerian perturbation becomes

$$Q'(\mathbf{a}, t) = Q - Q_0 + \mathbf{a}' \cdot \nabla_{\mathbf{a}} Q_0. \quad (\text{B.20})$$

So, remembering that $\mathbf{a}' = \mathbf{a}'(\mathbf{a}, t)$

$$\frac{\partial}{\partial t} \Big|_{\mathbf{a}} (Q') = \frac{\partial}{\partial t} \Big|_{\mathbf{a}} Q - \frac{\partial}{\partial t} \Big|_{\mathbf{a}} Q_0 + \left(\frac{\partial}{\partial t} \Big|_{\mathbf{a}} \mathbf{a}' \right) \cdot \nabla_{\mathbf{a}} Q_0 + \mathbf{a}' \cdot \frac{\partial}{\partial t} \Big|_{\mathbf{a}} (\nabla_{\mathbf{a}} Q_0). \quad (\text{B.21})$$

Applying the operations in the opposite order gives

$$\left[\frac{\partial Q}{\partial t} \Big|_{\mathbf{a}} \right]' = \frac{\partial Q}{\partial t} \Big|_{\mathbf{a}} - \frac{\partial Q_0}{\partial t} \Big|_{\mathbf{a}} + \mathbf{a}' \cdot \nabla_{\mathbf{a}} \frac{\partial Q_0}{\partial t} \Big|_{\mathbf{a}}. \quad (\text{B.22})$$

Switching the order of differentiation in the last term of either equation (B.21) or (B.22), subtracting, and changing to the notation of equation (B.4)

$$\left[\frac{D}{Dt}, ' \right] = \frac{D}{Dt}(Q') - \left[\frac{DQ}{Dt} \right]' = \frac{\partial \mathbf{a}'}{\partial t} \Big|_{\mathbf{a}} \cdot \nabla_{\mathbf{a}} Q_0. \quad (\text{B.23})$$

In general, the Eulerian perturbation and the advective derivative do not commute.

B.4.3 Lagrangian Perturbation, Commuting Operators

Next, consider the Lagrangian perturbation δ . To prove the equality of equation (B.16), use equation (B.4) and the form of the perturbation given in equation (B.12).

$$\frac{\partial}{\partial t} \Big|_{\mathbf{a}} (\delta Q) = \frac{\partial}{\partial t} \Big|_{\mathbf{a}} (Q) - \frac{\partial}{\partial t} \Big|_{\mathbf{a}} (Q_0) \quad (\text{B.24})$$

and

$$\delta \left(\frac{\partial Q}{\partial t} \Big|_{\mathbf{a}} \right) = \frac{\partial Q}{\partial t} \Big|_{\mathbf{a}} - \frac{\partial Q_0}{\partial t} \Big|_{\mathbf{a}}. \quad (\text{B.25})$$

The right-hand sides of equations (B.24) and (B.25) are equal, proving that the Lagrangian perturbation commutes with the advective derivative.

B.4.4 Lagrangian Perturbation, Non-Commuting Operators

The inequalities of equation (B.17) are best treated in the Eulerian description. Expanding equation (B.9) to first-order,

$$\delta Q(\mathbf{x}, t) = Q - Q_0 + \delta \mathbf{x} \cdot \nabla Q_0. \quad (\text{B.26})$$

Working first with the ∇ operator and recalling that $\delta \mathbf{x} = \delta \mathbf{x}(\mathbf{x}, t)$,

$$\nabla(\delta Q) = \nabla Q - \nabla Q_0 + (\delta \mathbf{x} \cdot \nabla) \nabla Q_0 + (\nabla Q_0 \cdot \nabla) \delta \mathbf{x} + \nabla Q_0 \times (\nabla \times \delta \mathbf{x}). \quad (\text{B.27})$$

The final three terms result from applying a vector identity to $\nabla(\delta\mathbf{x} \cdot \nabla Q_0)$. Applied in the reverse order, the operations produce

$$\delta(\nabla Q) = \nabla Q - \nabla Q_0 + (\delta\mathbf{x} \cdot \nabla)\nabla Q_0. \quad (\text{B.28})$$

Hence,

$$[\nabla, \delta] = \nabla(\delta Q) - \delta(\nabla Q) = (\nabla Q_0 \cdot \nabla)\delta\mathbf{x} + \nabla Q_0 \times (\nabla \times \delta\mathbf{x}). \quad (\text{B.29})$$

Finally, consider the commutation properties of the Lagrangian perturbation and the partial with respect to time at constant \mathbf{x} .

$$\left. \frac{\partial}{\partial t} \right|_{\mathbf{x}} (\delta Q) = \left. \frac{\partial}{\partial t} \right|_{\mathbf{x}} Q - \left. \frac{\partial}{\partial t} \right|_{\mathbf{x}} Q_0 + \left(\left. \frac{\partial}{\partial t} \right|_{\mathbf{x}} \delta\mathbf{x} \right) \cdot \nabla Q_0 + \delta\mathbf{x} \cdot \left. \frac{\partial}{\partial t} \right|_{\mathbf{x}} \nabla Q_0, \quad (\text{B.30})$$

but

$$\delta \left(\left. \frac{\partial Q}{\partial t} \right|_{\mathbf{x}} \right) = \left. \frac{\partial Q}{\partial t} \right|_{\mathbf{x}} - \left. \frac{\partial Q_0}{\partial t} \right|_{\mathbf{x}} + \delta\mathbf{x} \cdot \nabla \left. \frac{\partial Q_0}{\partial t} \right|_{\mathbf{x}} \quad (\text{B.31})$$

Again, by switching the order of differentiation in the last term of two preceding equation and subtracting,

$$\left[\left. \frac{\partial}{\partial t} \right|_{\mathbf{x}}, \delta \right] = \left. \frac{\partial}{\partial t} \right|_{\mathbf{x}} (\delta Q) - \delta \left(\left. \frac{\partial Q}{\partial t} \right|_{\mathbf{x}} \right) = \left. \frac{\partial \delta\mathbf{x}}{\partial t} \right|_{\mathbf{x}} \cdot \nabla Q_0. \quad (\text{B.32})$$

Equations (B.29) and (B.32) show that the Lagrangian perturbation commutes with neither the gradient operator nor the partial derivative with respect to time at constant position.

Appendix C

Alternate Forms of the Wave Equation

In §2.1.4, several approximations were made to arrive at the final form of the wave equation (2.30). For this appendix, we relax two of these assumptions, constant gravity and adiabatic stratification, and derive the resulting wave equations.

The starting point is equation (2.22), the perturbed momentum equation under Cowling's approximation:

$$\frac{\partial^2 \delta \mathbf{x}}{\partial t^2} = \nabla(c^2 \chi - g\xi) + (c^2 \frac{\nabla \rho}{\rho} + g\hat{\mathbf{r}})\chi. \quad (\text{C.1})$$

Our previous assumptions of constant gravity allowed us to write expressions such as $\nabla^2(g\xi) = g\nabla^2\xi$. In the general case, we cannot make such a statement. Instead we have four parameters (the three components of $\delta \mathbf{x}$ and χ) and thus need four separate equations to reduce the equation to one in terms of χ only. Of course, since $\chi = \nabla \cdot \delta \mathbf{x}$ the four variables are interrelated. We proceed by applying four operators to (C.1), yielding the following equations:

(a) $\nabla \cdot$

$$\nabla^2(g\xi) = \nabla^2(c^2 \chi) - \frac{\partial^2 \chi}{\partial t^2} + \hat{\mathbf{r}} \cdot \nabla(\beta \chi) + \frac{2\beta \chi}{r}, \quad (\text{C.2})$$

(b) $\hat{\mathbf{r}} \cdot \nabla \times \nabla \times$

$$\frac{\partial^2}{\partial t^2} \nabla^2 \xi = \nabla_h^2(\beta \chi) + \frac{2\beta \chi}{r^2} + \frac{\partial^2}{\partial t^2} (\hat{\mathbf{r}} \cdot \nabla \chi), \quad (\text{C.3})$$

(c) $\nabla_h \cdot$ (horizontal component)

$$\frac{\partial^2}{\partial t^2} \left(\frac{\partial \xi}{\partial r} + \frac{2\xi}{r} \right) - \nabla_h^2(g\xi) = \frac{\partial^2 \chi}{\partial t^2} - \nabla_h^2(c^2 \chi), \quad (\text{C.4})$$

(d) $\hat{\mathbf{r}} \cdot$

$$\frac{\partial^2 \xi}{\partial t^2} + \hat{\mathbf{r}} \cdot \nabla(g\xi) = \hat{\mathbf{r}} \cdot \nabla(c^2 \chi) + \beta \chi. \quad (\text{C.5})$$

Equations (C.2) and (C.3) are the same as equations (2.24) and (2.25), respectively.

From our work in §2.1.3, we know that the angular parts of the perturbation variables are given by spherical harmonics. Hence, we are free to make the substitution

$$\nabla_h^2 = -\frac{\ell(\ell+1)}{r^2}. \quad (\text{C.6})$$

With this simplification, equations (C.2)–(C.5) are four linear equations for the four unknowns ξ , $\dot{\xi}$, $\ddot{\xi}$, and χ where a dot represents a derivative with respect to the radial coordinate r . Simple substitution quickly reduces the equations to the form

$$\left[\left(\ddot{\xi} - \frac{2\dot{g}}{r} \right) \frac{\partial^2}{\partial t^2} - \frac{2\ell(\ell+1)}{r^2} g \dot{g} \right] \xi = \frac{\partial^2}{\partial t^2} B_1(\chi) - g B_2(\chi) - 2\dot{g} B_3(\chi) \quad (\text{C.7})$$

and

$$\left[\frac{\partial^4}{\partial t^4} + \left(\dot{g} - \frac{2g}{r} \right) \frac{\partial^2}{\partial t^2} - \frac{\ell(\ell+1)}{r^2} g^2 \right] \xi = -g B_3(\chi) + \frac{\partial^2}{\partial t^2} B_4(\chi), \quad (\text{C.8})$$

where $B_1(\chi)$, $B_2(\chi)$, $B_3(\chi)$, and $B_4(\chi)$ are the right-hand sides of equations (C.2)–(C.5), respectively.

In order to eliminate the partial derivatives with respect to time, we work with only one Fourier component of the solution and hence make the substitution $\frac{\partial}{\partial t} \rightarrow -i\omega$. Although it is possible to produce a final partial differential equation without any further restrictions, the algebra is quite involved. This is why the simplifying assumptions of §2.1.4 were made: they illuminated the underlying physics without clouding the result with mathematical complications. In that spirit we consider a looser set of assumptions, with a better physical rationale, than those considered in the main text. From the spherical symmetry of the reference state, we already know that $g = g(r)$. However, the solar mass distribution is centrally condensed — the convection zone accounts for only 2% of the total mass despite occupying the outer 30% by radius. Furthermore, p modes of large spherical degree traverse only the outermost regions of the

convection zone. Thus, gravity for the p modes under consideration is well approximated by a free-space potential. Under this assumption, there is a simple relation between the gravitational acceleration and its radial derivatives,

$$\dot{g} = \frac{-2g}{r} \quad \text{and} \quad \ddot{g} = \frac{6g}{r^2}. \quad (\text{C.9})$$

We first consider a system with an adiabatic stratification (in other words, $\beta = 0$), but gravity as specified in (C.9). Equations (C.7) and (C.8) can be reduced to the following form:

$$\begin{aligned} & \left(\frac{\partial^4}{\partial t^4} - \frac{4g}{r} \frac{\partial^2}{\partial t^2} + g^2 \nabla_h^2 \right) \left[\frac{\partial^2 \chi}{\partial t^2} - \nabla^2 (c^2 \chi) + g \hat{\mathbf{r}} \cdot \nabla \chi \right] - \\ & \left(\frac{4g}{r} \frac{\partial^2}{\partial t^2} - \frac{6g^2}{r^2} \right) \left[\frac{\partial^2 \chi}{\partial t^2} - \nabla_h^2 (c^2 \chi) \right] + \left(\frac{10g}{r^2} \frac{\partial^2}{\partial t^2} - \frac{4g^2}{r} \nabla_h^2 \right) \hat{\mathbf{r}} \cdot \nabla (c^2 \chi) = 0, \end{aligned} \quad (\text{C.10})$$

where equation (C.6) and the correspondence between $\frac{\partial}{\partial t}$ and $-i\omega$ have been used to put the result in a form similar to (2.26). To compare to our previous results, we take the plane-parallel limit ($r \rightarrow \infty$). Doing so yields

$$\left[\frac{\partial^2 \chi}{\partial t^2} - \nabla^2 (c^2 \chi) + g \hat{\mathbf{r}} \cdot \nabla \chi \right] = 0, \quad (\text{C.11})$$

which is equivalent to equation (2.26) in the limit of adiabatic stratification.

Although equation (C.10) contains odd derivatives of χ , we cannot transform it into a Helmholtz-like form, as we did with equation (2.27), due to the final terms on the left-hand side.

Defining the differential operators

$$L_1 = \frac{\partial^4}{\partial t^4} - \frac{4g}{r} \frac{\partial^2}{\partial t^2} + g^2 \nabla_h^2, \quad L_2 = \frac{4g}{r} \frac{\partial^2}{\partial t^2} - \frac{6g^2}{r^2}, \quad \text{and} \quad L_3 = \frac{10g}{r^2} \frac{\partial^2}{\partial t^2} - \frac{4g^2}{r} \nabla_h^2, \quad (\text{C.12})$$

and making the same substitution as before, $\Psi = c^2 \rho^{1/2} \chi$, we find that

$$L_1 \left[\frac{\partial^2 \Psi}{\partial t^2} - c^2 \nabla^2 \Psi + \omega_c^2 \Psi \right] - L_2 \left[\frac{\partial^2 \Psi}{\partial t^2} - c^2 \nabla_h^2 \Psi \right] + L_3 \left[c^2 \hat{\mathbf{r}} \cdot \nabla \Psi + \frac{g \Psi}{2} \right] = 0, \quad (\text{C.13})$$

where the acoustic cutoff frequency ω_c is the same as defined in equation (2.28). Again this form is equivalent to equation (2.30) in the plane-parallel limit. If desired this equation can be placed in the form of a dispersion relation analogous to equation (2.35), although the expression is somewhat complicated.

Finally, for completeness, we present the governing equation for the more general case where $\beta \neq 0$ and where derivatives of the gravitational acceleration are of the form given in equation (C.9). After some algebra, and in terms of Ψ , the result is

$$L_1 \left[\frac{\partial^4 \Psi}{\partial t^4} - \left(c^2 \nabla^2 - \omega_c^2 - \frac{2\beta\chi}{r} \right) \frac{\partial^2 \Psi}{\partial t^2} - \left(c^2 N^2 \nabla_h^2 - \frac{2\beta g c^2}{r^2} \right) \Psi \right] - \\ L_2 \left[\frac{\partial^4 \Psi}{\partial t^4} - c^2 \frac{\partial^2}{\partial t^2} \nabla_h^2 \Psi \right] + L_3 \left[\frac{\partial^2}{\partial t^2} \left(c^2 \hat{\mathbf{r}} \cdot \nabla \Psi + \frac{g\Psi}{2} \right) + \beta \frac{\partial^2 \Psi}{\partial t^2} \right] = 0. \quad (\text{C.14})$$

The first term in square brackets is identical with equation (2.27) and in the appropriate limits this form reduces to our previous results.

Appendix D

The Computer Code

Originally written in IDL during 1995 to implement the method described in §2.4.4, the code has undergone several revisions since then. In 1997 it was translated into FORTRAN90 when it was realized that the benefits of IDL's graphical capabilities did not outweigh FORTRAN's greater speed and numerical precision. We first used adiabatic switching in a fashion similar to the current version in 1998. For structural reasons, the code has been broken into modules, each of which is described in the table below.

Table D.1: Modules used in our adiabatic switching code. Files above the line are necessary while those below the line generate test data, but are not required for use.

File (*.f90)	Function
<code>constants</code>	Defines useful constants such as the polytropic index, gravitational acceleration, domain size, and the switching period.
<code>eureka</code>	The top level of the integration routines from Shampine & Gordon (1975). This routine allocates storage for variables and calls subsequent programs.
<code>func</code>	Defines and evaluates the differential equations used by the ray-tracing routine — in other words, the right-hand-side of Hamilton’s equations.
<code>main</code>	The top-level program. It sets the initial conditions, writes useful data to a file for later reference, and calls the integration routines.
<code>mod1</code>	Part of the integration routine. It supervises the integration and evaluates its success or failure.
<code>mod2</code>	The heart of the integration routine, it uses the Adams PECE formulas to solve Hamilton’s equations. The code adjusts its order and step size to control the error.
<code>mod3</code>	The final part of the integration routine. After previous parts of the code approximate the solution with a polynomial, this subroutine finds the solution at the desired point.
<code>sound</code>	On the first call it loads the mesh of sound speeds into memory for quicker access. On all subsequent calls it calculates the sound speed and directional derivatives at a point in the domain.
<code>switching</code>	Defines and evaluates the form of the switching function.
<code>velocity</code>	On the first call it loads the mesh of advective velocities into memory for quicker access. On all subsequent calls it calculates the velocity and directional derivatives at a point in the domain.
<code>c_func</code>	Defines and evaluates the functional form of the sound speed when creating a grid of values.
<code>make_c</code>	Creates a grid with a given spacing (set in <code>constants.f90</code>) of sound speeds.
<code>make_v</code>	Creates a grid with a given spacing (set in <code>constants.f90</code>) of advective velocities.
<code>v_func</code>	Defines and evaluates the functional form of the advective velocity when creating a grid of values.